**Democratic and Popular Republic of Algeria**

**Ministry of Higher Education and Scientific Research**

**University Abou Bekr Belkaid, Tlemcen**

**Faculty of technology, Chetouane**
**Department of Electrical Engineering and Electronics**

# D O C T O R A T
# T H E S I S

**Mention: Electronics**

# Synthesis of time–frequency analysis methods applied to Phonocardiogram signal

by

Abdelghani Djebbari

2013

**Jury :**

| | | | |
|---|---|---|---|
| *Advisor :* | Prof. Fethi Bereksi–Reguig | – | University of Tlemcen |
| *President :* | Prof. Mohammed El Amine Debbal | – | University of Tlemcen |
| *Examiners :* | Prof. Ali Djebbari | – | University Djilali Liabès, Sidi Bel Abbès |
| | Dr. Said Assous | - | University of Leicester, UK |

# Dedication

To my parents,

my brothers and sisters,

my wife,

my sons,

and all my family.

# Acknowledgements

I would like to thank Prof. Fethi Bereksi–Reguig to accept to be the advisor of this thesis. His advices were of great interest to me to manage all steps of this work.

All my gratitude to Prof. Louis–Gilles Durand, "Officier de l'ordre national du Québec", for receiving me in his laboratory in the "Institut de recherches cliniques de Montreal (Quebec, Canada)", for putting at my disposal all required material to accomplish this work. My stay in Montreal working with Louis–Gilles Durand was so vital to me to learn about the beauty of biomedical engineering.

I also got the opportunity to meet Prof. Yves Meyer, whom received me in the "École normal supérieure (ENS) de Cachan" during a training period. His help was invaluable to refresh gazing out wavelets. Many thanks to Prof. Yves Meyer to allow me to meet Prof. Stéphane Mallat, whom revolutionised the wavelet world by developing the Quadrature mirrors filters. Momentous discussions with Stéphane Mallat and Yves Meyer about some signal processing issues was so beneficial to me.

I would like also to thank Prof. Abderrahim Meziane–Tani, head of the Cardiology department of the Teaching hospital of Tlemcen, for receiving me to record data despite his great and various charges.

Many thanks to Prof. Sidi Mohammed Debbal, Prof. Ali Djebbari, and Prof. Said Assous for accepting to join the jury to examine this work. Special admiration to Said Assous, so thank you for being a great spring of inspiration and hope.

Last but not least, I would like to thank my dear parents to support every single step in all my studies.

**Abstract**

Digital phonocardiography is the acoustic recording of the intracardiac hemodynamic activity. Heart sounds and murmurs recorded as phonocardiographic signals include reliable information in investigating the valvular functioning.

This thesis investigates the time–frequency content of phonocardiographic signals through advanced digital signal processing methods. As a first part, heart sounds and murmurs are studied to understand their nature and genesis. The multidegree of freedom theory concludes several theories behind genesis of heart sounds and murmurs. Understanding the genesis theory allow to select the appropriate tool for analysis.

In the second part, time–frequency methods are studied through their theoretical background. Practical applications complement the study to select the adequate time–frequency methods to be used during analysis. The Reassigned smoothed pseudo Wigner–Ville distribution among several time–frequency methods brings to light the required digital signal processing elements to appropriately process information within phonocardiographic data.

Finally, several techniques were developed to support the selected time–frequency methods as adaptive algorithms towards extracting information from heart sounds and murmurs.

An adjustment algorithm was developed to resolve the amplitude attenuation issue within heart sounds. Additionally, a dechirping algorithm was developed to resolve the phase cancellation issue that cancel valuable valvular sounds during their transmission from the heart to the chest. A detection algorithm of the valvular split within heart sounds based on the Reassigned smoothed pseudo Wigner–Ville distribution was developed. These algorithms were validated on simulated and real heart sounds. Phonocardiographic signals were recorded within the CHUT (Centre hospitalier universitaire de Tlemcen), and from the LGB–IRCM (Laboratoire de Génie biomédical – Institut de recherches cliniques de Montreal) cardiac valve database. A mother wavelet was developed from the Valvular chirplet model valvular heart sounds. This mother wavelet allowed better scalograms in comparison to usual Morlet and discrete Meyer wavelets. A global analysis of abnormal phonocardiographic signals was performed by wavelet packets to localise energy within the forming frequency subbands of the analysed signal.

**Keywords:** Digital phonocardiography, heart sounds, heart murmurs, time–frequency analysis, valvular chirplet model, reassigned smoothed pseudo Wigner–Ville distribution, wavelet analysis, discrete wavelet transform, wavelet packets.

# Contents

# List of Figures

# List of Tables

# Innovative digital signal processing algorithms

1. **Amplitude recovery algorithm** of heart sounds to resolve the **amplitude attenuation** issue of heart sounds within thoracic phonocardiograms.
2. **Dechirping algorithm** developed to resolve the **phase cancellation** issue between intracardiac valvular sounds within phonocardiographic signals.
3. **Time–frequency detection algorithm of heart murmurs**.
4. **Adapted mother wavelet** developed from the **Valvular chirplet model (VCM)** of valvular heart sound to be applied on phonocardiographic signals through Continuous wavelet transform (CWT).

# Introduction

A normal phonocardiographic (PCG) signal is mainly formed by two major acoustic vibrations groups which appears during one cardiac cycle, namely the first (S1) and the second (S2) heart sounds. These two sounds delimits the onset of systole and diastole phases respectively. The systole corresponds to blood ejection from the heart to the entire body. The diastole, which lasts more than the systole phase, is the relaxation period of the heart during a cardiac cycle. There are two other heart sounds known as the third (S3) and the fourth (S4) heart sounds, which are not usually recorded unless under specific physiological conditions or within a well known cardiovascular pathologies.

The heart is formed by two major parts known as the right and the left hearts. Each part is constituted by an atrium and a ventricle communicating between them by means of an atrioventricular valve, mitral and tricuspid valves for the right and left sides of the heart respectively. Aortic and pulmonary valves, also known as semilunar valves, ensures blood flow circulation from and towards the heart. During the cardiac cycle which lasts approximately about 0.7 $s$ in normal subjects, blood circulates within heart cavities and vessels according to opening and closure of the four cardiac valves which generates S1, S2, S3, and S4 heart sounds during the cardiac cycle. The main heart sounds, namely S1 and S2, are generated by alternative opening and closure of atrioventricular and semilunar valves. The S1 and S2 heart sounds are mainly formed by closure of atrioventricular and semilunar valves, respectively. These slightly simultaneous events generate acoustic components denoted M1 and T1, as mitral and tricuspid valvular closures forming the S1 heart sound, as well as A2 and P2 components, corresponding to aortic and pulmonary valvular closures forming the S2 heart sound, respectively. The atrioventricular and semilunar valves open and close alternatively during the cardiac cycle. However, cardiovascular pathologies alter this synchronised functioning and yield murmurs within phonocardiographic recordings.

The human heart activity is basically articulated around its two functioning modes; namely contraction (systole) and relaxation (diastole) cardiac periods. Thus, the boundaries of each cardiac period are marked by alternative functioning of heart valves. Therefore, blood flow circulation in addition to heart valves closures and openings generate heart sounds. Any deterioration of the cardiac valves should affect the nature of the generated sounds by adding stenotic, regurgitant and musical murmurs. Hence, heart sounds and murmurs constituting the Phonocardiogram

(PCG) signal are in correlation with intracardiac hemodynamics. However, these sonic vibrations are also affected by the heart–thorax system[4]. Moreover, the human ear cannot accurately perceive the temporal and spectral characteristics of the heart sounds and murmurs, because of their very short durations and their low frequency activity aspect. Additionally, the PCG signal should restrain both modulation laws caused by blood turbulences into the myocardium and also split sounds components.

Heart sounds are of great clinical importance, but remain confusing physicians about their origins. Certainly, the more persuading theory is that proposed by Durand et al.[5], which gathered both the valvular and the cardiohemic theories. This theory consists of linking heart sounds with vibrations due to cardiac valvular activity as well as blood circulation within heart vessels and cavities. This new theory stipulates that before arriving to the thorax, heart sounds had crossed different tissues; therefore, they should be affected by the contribution of the overall heart–thorax system. This concept highlights the relationship between cardiac structures and their vibrations modes to the resulting thoracic Phonocardiogram (PCG). As concluded by Durand et al. [6], the heart–thorax system affects intracardiac heart sounds to be attenuated within the thoracic PCG. Transmitted through thoracic tissues, the rising frequency component of the S1 heart sound should be affected by *magnitude attenuation* or *phase cancellation*. All these debating results are complementary rather than contradictory, since the recorded PCG changes according to the auscultation area which favours valvular or non–valvular intracardiac activity.

Fourier theory provides a frequency overview of a signal through power spectral density (PSD) which can be estimated as a periodogram or even more as an averaged periodogram known as Welch's estimator [7, 8]. Only a frequency dependent energy representation can be provided through Fourier–based PSD estimation methods. However, Gabor transform and its obvious extension which is the short–time Fourier transform (STFT) enables a time–related frequency analysis. This can be achieved by segmenting a given signal into elementary portions to be analysed by the discrete Fourier transform (DFT). Each spectrum is assigned to the middle instant of the weighting window to create a time dimension within the STFT representation. The main restraint facing the STFT to represent signals is its poor joint time–frequency localisation within the time–frequency plane. Time–frequency analysis methods are then the bright solution to this well known digital signal processing issue towards representing transients within biomedical signals. Moreover, wavelet transform, which is based on a scale parameter rather than frequency, can prominently outstand in appropriatly representing the complex content of phonocardiographic signals and outperform spectral methods.

The first heart sound (S1) contains both valvular halting snaps of the mitral and tricuspid heart valves and also blood flow circulation within cavities of the myocardium. This sound which indicates the beginning of the ventricular systole phase is mainly due to the closure of atrioventricular valves. It was shown by Wood et al. [9] that the S1 heart sound when recorded from the epicardium contains a rapidly rising frequency component during early systole, which was correlated with

the rising left ventricle pressure. Moreover, the first heart sound S1 could favour impulse–like components. The second heart sound (S2) appears at the beginning of the ventricular diastole, and can reach 200 Hz for normal subjects. For a normal subject, the third (S3) and the fourth (S4) heart sounds cannot be recorded because of their low intensity[5]. These heart sounds are of great clinical importance, for instance, the S3 heart sound can be an indicator of heart failure in patients with asymptomatic left ventricular dysfunction.

In a previous work, a temporal analysis of heart sounds and murmurs allows us to separate systole and diastole phases within a cardiac cycle [10]. Liang *et al.* [11] proposed an algorithm based on the normalised average Shannon energy of the PCG signal to detect systolic and diastolic heart sounds and murmurs. Spectral analysis methods can be combined with such time domain analysis to assess the valvular pathology severity. Clarke *et al.* [12] studied the spectral content of the first heart sound and concluded that its spectral energy can be used to detect myocardial ischemia. Stein *et al.* [13] found that the aortic component of the second heart sound can be investigated as a characterisation parameter of the aortic valve status. They reported that a stiffened valve generates a higher than normal frequency of the A2 component. Therefore, both temporal and spectral approaches should be combined to study the physiological information within heart sounds and murmurs. Thus, these short–duration acoustic waveforms which occur within different frequency subbands inside the PCG power spectrum can be adequately analysed by means of time–frequency analysis as well as time–scale analysis methods.

Several works studied successfully abnormal valves activity by localising and analysing murmurs they generate. Choi *et al.* [14] used the wavelet packets decomposition to study the aortic and mitral insufficiency murmurs. They concluded that S1 and S2 heart sounds lies up to 200 Hz and that frequencies between 300 and 500 Hz can be used as a discriminating bandwidth between the cardiac pathological PCG signals. Al–Naami *et al.* [15] used the norm entropy–based criterion within wavelet packets applied to PCG signals to early detect aortic stenosis (AS). Liang *et al.* [16] used wavelet packets to define feature vectors which served as input of a neural network to detect pathological murmurs at 85% as accuracy ratio.

The objective of the work presented within this thesis is to develop appropriate analysis tools that properly retrieve intracardiac functioning information from phonocardiographic signals within the time–frequency plane. The theoretical background of time–frequency analysis methods is to be studied to properly select a method that matches the content of heart sounds and murmurs. The main issues to overcome during analysis of phonocardiographic signals are amplitude attenuation and phase cancellation when recorded from the chest of the patient. Therefore, phonocardiographic dedicated processing algorithms are to be developed to overcome amplitude attenuation and phase cancellation.

This thesis is partitioned into three chapter. The first one, entitled “Heart sounds and murmurs”, presents the various behaviours of phonocardiographic signals by linking their content with the corresponding hemodynamics behind their genesis. The second chapter, entitled “Time–frequency analysis methods”, gathers the re-

quired theory of time–frequency analysis methods and presents their ability to represent particular waveforms to highlight their benefits and drawbacks. The third chapter, entitled “Time–frequency analysis of phonocardiograms”, adapts the studied time–frequency methods to heart sounds and murmurs to explore their hemodynamic content. An appendix presents the graphical user interfaces of some developed software, and clinical information of some pathological cases studied in ChapterIII.

# Chapter I

# Heart sounds and murmurs

The heart beats continuously during the entire human life to ensure blood circulation through the whole body of a human being. This vital organ, which is the blood pump within the cardiovascular system, is the acoustic source of heart sounds and murmurs. The auscultation of the cardiac activity remains a basic examination of the heart and can be performed by means of a stethoscope[1] usually used by physicians to assess the cardiac condition of a patient. Digital stethoscopes had been introduced as improved heart auscultation devices allowing a better exploration of the cardiac activity.

Sounds perceived during auscultation can be represented as a graph which is known as Phonocardiogram (PCG). Phonocardiography is suitable for detecting valve disease, pulmonary hypertension, ventricular dysfunction, coronary artery disease, and cardiomyopathies [5]. However, at the beginning of the 1970's, phonocardiography known toughness to evolve among medical diagnosis techniques and therefore undergone slower development for several reasons. The PCG signal, which is the acoustic recording of heart sounds and murmurs, is not easily readable by medical staff than other physiological signals are, as for instance the Electrocardiogram (ECG). The transient nature of the PCG signal deprived it from pioneering medical signals aimed for cardiac exploration. Moreover, controversy stills blurring the origin of heart sounds and murmurs. The thorax is contributing in bringing up more ambiguity around the genesis of heart sounds and murmurs. Indeed, heart sounds and murmurs, going across the tissues between the heart and the thorax, are transmuted by the filtering effect of the heart–thorax system [18, 5]. Furthermore, recording heart sounds and murmurs from various thoracic sites complicates the analysis and comparison of the acquired PCG signals. In addition, furtherance of ultrasound imaging extinguished heart auscultation and phonocardiography as emerging medical technique.

When computers's dawn broke, a new era loomed up yielding digital phonocardiography. Indeed, data acquisition gave a new perception of heart sounds and murmurs

[1] Acoustic medical device allowing to listen to the sounds of the heart, blood vessels, and lungs [17]. It can also be used with a sphygmomanometer to measure blood pressure.

as digital phonocardiogram signal which can be stored within a computer. Moreover, the advent of digital signal processing techniques enable digital phonocardiography to benefit from new processing methods. Resonant features of heart valves as well as blood flow turbulence within heart cavities can be digitally quantified. Therefore, digital phonocardiography became a reliable tool for detecting valvular pathologies as well as preventing valvular prosthesis dysfunction. Thus, several researchers watched over analysis of heart sounds and murmurs by advanced digital signal processing methods. Hence, the PCG signal can provide a valuable medical diagnosis towards exploration of the cardiac activity. Myriad scientific research papers were published around the genesis of heart sounds and murmurs. Consequently, several theories occurred explaining the origin of each vibration recorded within the PCG signal for both normal and abnormal subjects.

The present chapter introduces heart sounds and murmurs with a detailed study about their genesis and nature and is organised as follows. Section I.1 entitled "Anatomy of the heart" presents the Internal anatomy of the human heart. In section I.2 entitled "Intracardiac hemodynamics", the intracardiac hemodynamics are studied. Section I.3 entitled "Heart auscultation" deals with auscultation of the intracardiac activity. In section I.4 entitled "Genesis theories of heart sounds", basic theories of heart sounds and murmurs generation are presented. Finally, section I.5 entitled "Sounds of intracardiac vibrations", presents phonocardiogram signals of normal and abnormal heart sounds.

## I.1 Anatomy of the heart

The heart is located at the superior surface of the diaphragm. It is formed by four chambers as an atrium–ventricle pair which are arranged side by side to form the right and left hearts. The atria allow collecting blood and the ventricles allow ejecting this blood away from the heart. The heart is a muscular pump which ensures two main functions. The first one, which is accomplished by the right heart, is to pump deoxygenated blood coming from the body tissues toward the lungs to evacuate carbon dioxide and to be reloaded by oxygen. The second function, which is ensured by the left heart, is to be filled up by oxygenated blood coming from the lungs and to pump it to the overall body tissues to provide oxygen, the blood is then reloaded by carbon dioxide.

During the cardiac cycle, these cavities communicate between them through atrioventricular valves; mitral and tricuspid valves. These valves allow blood flow circulation between the atrium and ventricle of the left and right hearts, respectively.

The superior and inferior venae cavae gather deoxygenated blood from the upper and lower parts of the body, respectively. Thus, the whole deoxygenated blood is collected within the right ventricle which pump it out from the heart through the pulmonary trunk[2]. The blood is then oxygenated and returns from the right and left

[2]Trunk when referring to a vessel is an artery that bifurcates. The pulmonary trunk bifurcates into the right and left pulmonary arteries that enter the lungs [19].

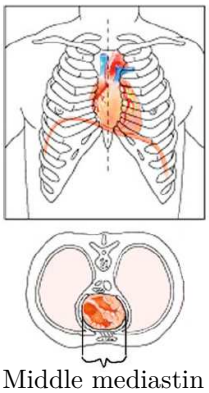


Figure I.1: The heart within the thorax [19]

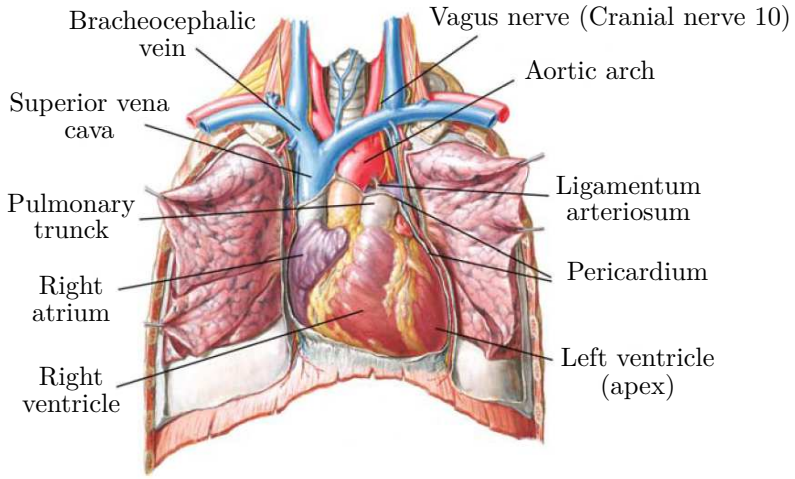


Figure I.2: Anterior view of the heart [19]

lungs through the right and left pulmonary veins[3], respectively. Assembled within the left atrium, the oxygenated blood is carried to the left ventricle to be pumped to body tissues through the aortic artery.

There are two distinct circuits allowing blood circulation through the entire body, namely the pulmonary and systemic circuits, as illustrated in Figure I.4. The pul-

[3] A vein is vessel carrying blood toward the heart. The right and left pulmonary veins bifurcates to form four veins entering the heart through the left atrium [19].

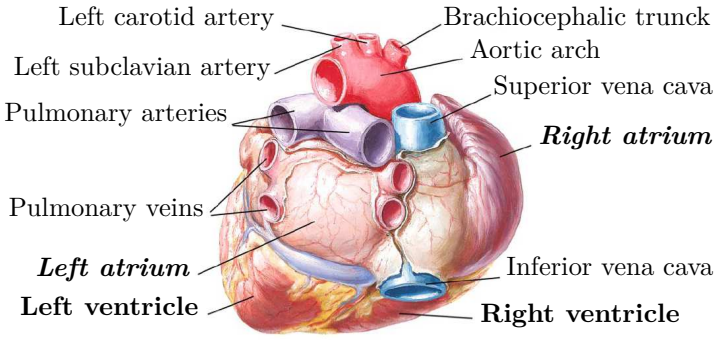


Figure I.3: Exterior view of the heart. Source: [19]

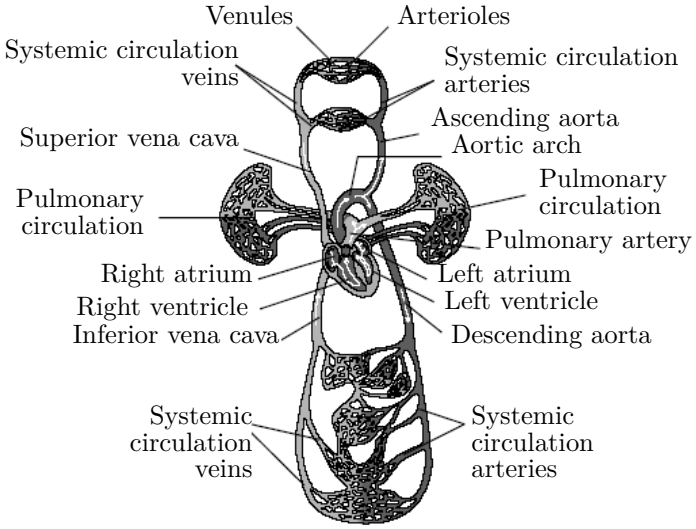


Figure I.4: Circulation. Source: [20]

monary circuit relies on the right heart, pulmonary artery, and veins to allow blood circulation from and toward the lungs. The systemic circuit is centred around circulatory functions of the aortic artery, venae cavae, and left heart which allows blood to be pumped to and from the entire body tissues. Blood flows unidirectionally

within the heart by means of intracardiac valves. Thus, atria are filled up by the incoming blood and eject it through atrioventricular[4] (AV) valves to ventricles which pump it away from the heart [19].

### I.1.1 Right atrium

As illustrated in Figure I.5, the right atrium is connected to the superior and inferior venae cavae as well as the coronary sinus. The right atrium contains the fossa ovalis, sinoatrial node, and atrioventricular (AV) node. The inferior part of the right atrium contains the opening or ostinum of the Inferior vena cava, and the os or ostinum of the coronary sinus. The coronary sinus which receives the deoxygenated blood is at the inferior part of the heart. The Eustachian[5] and Thebesian[6] valves are venous valves and are located on the inferior border ridge of the atrium separating the os of the coronary sinus and inferior vena cava. The fossa ovalis is located on the interatrial part of the atrial septum. The tendon of Torado ensure connection between the valve of the inferior vena cava and the interventricular septum. The sinoatrial node is the electric impulse contraction generator of atria. This electric excitation node, which provides regular impulses allowing contraction of atria, is located between the myocardium and epicardium in the superior part of the right atrium.

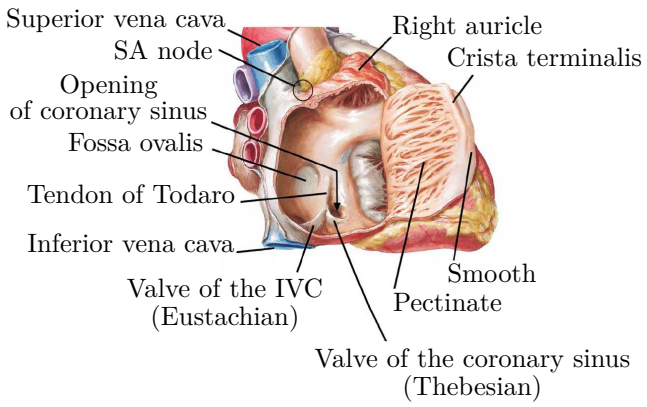


Figure I.5: Right atrium [19]

[4]Valves separating atria from ventricles within the left and right heart, namely the tricuspid and bicuspid (mitral) valves.

[5]A fetal remnant located at the orifice of the inferior vena cava, Bartolommeo E. Eustachio, Italian anatomist, 1520–1574 [19].

[6]Valve of the coronary sinus, serves to obviate blood backflow, Adam C. Thebesius, German physician, 1686–1732 [19].

### I.1.2 Right ventricle

The right ventricle (Figure I.6) is located at the anterior surface of the heart. The role of the right ventricle is to collect blood from the right atrium then to pump it to lungs through the pulmonary trunk and arteries. The wall of the right ventricle is formed by coarse trabeculae carnae[7]. The conus arteriosus[8] is a part of the infundibular septum[9] which separates the right and left ventricles and is located inferior to the semilunar valves. The semicircular arch[10] separates the blood ejection tract from the right atrium [19].

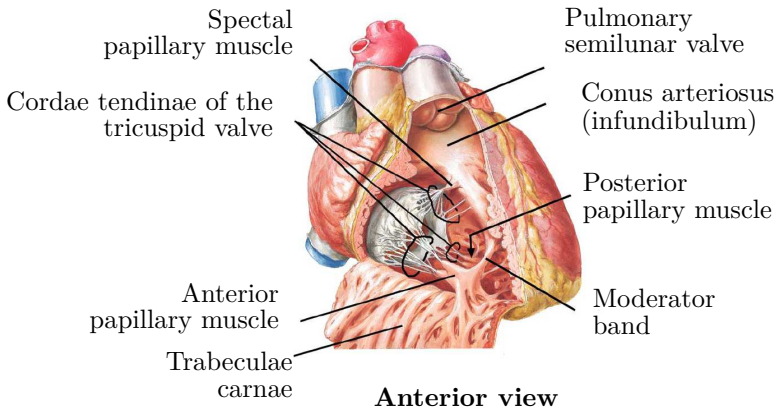


Figure I.6: Right ventricle [19]

#### Tricuspid valve

The tricuspid[11] valve (Figure I.7) is the gate separating the right atrium from the right ventricle. This atrioventricular valve is strengthened by the annulus fibrosus of the cardiac skeleton to avoid blood regurgitation. This valve is formed by the annulus, three valvular leaflets, three papillary muscles, and three bundles of chordae tendinae. The tricuspid valve have three leaflets: anterior(superior), posterior (inferior), and septal. The anterior leaflet, which is the largest one, is delimited between the medial border of the ventricular septum and the anterior wall of the myocardium. The posterior leaflet is located between the lateral free wall of the myocardium and the posterior part of the ventricular septum. The septal leaflet

[7] muscular columns or fleshy beams at the inner surface of the right and left ventricles, analogous to pectinate muscle of the right atrium.

[8] or infundibulum (arterial cone): a funnel–shaped tract responsible of blood ejection within the right ventricle.

[9] interventricular conal septum

[10] muscle bundles known as supraventricular crest and septomarginal trabeculae.

[11] named tricuspid for its three cusps.

is oval–shaped and is delimited by the annulus of the orifice and the medial side of the interventricular septum. Papillary muscles pull chordae tendinae which are fixed to leaflets to get securely ready to the huge ventricular contraction. Indeed, this configuration avoids prolapse[12] of the leaflets within the atrium [19].

The total area of the tricuspid valve leaflets is approximately twice that of the tricuspid orifice to provide adequate closure preventing blood backflow to the right atrium during ventricular systole. The junction between two adjacent leaflets is called a commissure which is named by its respective leaflets (anteroseptal, anteroposterior, and posteroseptal). Chordae tendinae are present upon each commissure as a smooth arc to ensures a firm valvular closure [19].

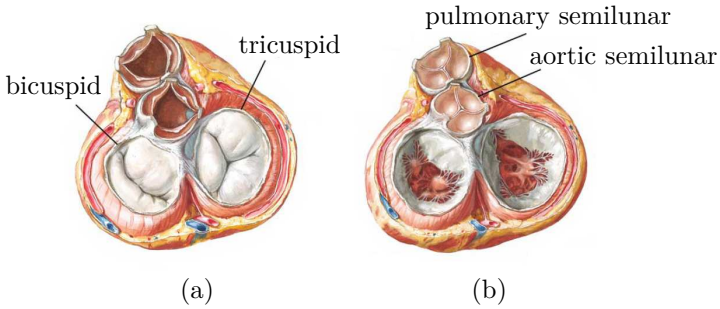


Figure I.7: Intracardiac valves: (a) systole and (b) diastole [19]

### Pulmonary valve

After ventricular systole, the pulmonary semilunar valve (Figure I.7) closes to avoid blood backflow from the pulmonary trunk and arteries to the right ventricle. This valve is formed by three symmetric, semilunar–shaped cusps attached to an annulus which is fixed to both the right ventricular infundibulum and the pulmonary trunk. Cusps of the pulmonary semilunar valve are named according to their position: anterior, left (septal), and right.

## I.1.3 Left atrium

The oxygenated blood coming from the lungs is collected within the left atrium through the left and right pulmonary veins. The left atrium is located between the right atrium and left ventricle in a midline position. The walls of the left atrium

[12] displacement of an organ from its normal position.

are smooth due to their embryological origin whereas the walls of atrial appendage are pectinate. The left atrium go back to the fetal pulmonary vein as a link to the embryonic pulmonary venous plexus. The atrial septum of the left atrium go back to the embryonic septum primum. The valve of the foramen ovale is a sealed valve flap as an embryonic remnant structure [19].

### I.1.4 Left ventricle

The left ventricle (Figure I.8), is responsible for collecting the oxygenated blood from the left atrium and pumping it toward tissues of the body. The left ventricle is at the left lateral surface of the heart, and its walls are formed by abundant trabeculae carnae which their muscular ridges are thinner beside those of the right ventricle. However, the myocardium of the left ventricle is thicker in comparison to that of the right ventricle. The interventricular septum is curved toward the right ventricle so that the left ventricle is barrel–shaped.

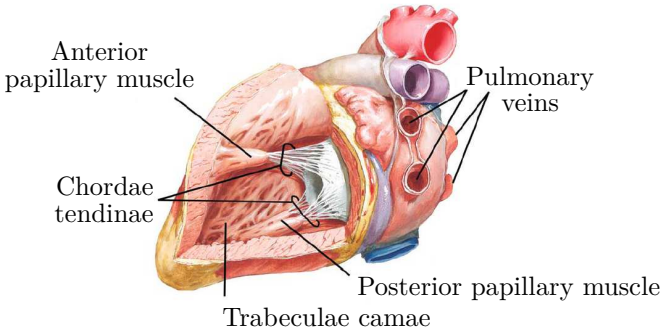


Figure I.8: Left ventricle [19]

#### Mitral valve

The oxygenated blood is pumped from the left atrium to the left ventricle through the left atrioventricular orifice. During ventricular systole, blood is prevented to flow back to the left atrium thanks to closure of the mitral[13] valve (Figure I.7 & Figure I.9) also known as mitral[14] valve. This atrioventricular valve is formed by an annulus, two leaflets, two papillary muscles and two sets of chordae tendinae. The posterior leaflet is narrow than the anterior which is trapezoidal–shaped. Papillary muscles with chordae tendinae ensure fixing the leaflets to prevent them prolapsing within the left atrium. Similarly to the right atrioventricular valve, the leaflets of the bicuspid valve are of a surface greater than that of the left atrioventricular orifice.

[13] also known as bicuspid valve, formed by two cusps.
[14] also named mitral valve for its resemblance to a miter which is a tall pointed hat (Figure I.9).

Mitral cusps are of abundant surface area which ensure firm closure during ventricle systole without any prolapsing. The two cusps of the mitral valve are joined at the anterolateral and the posteromedial commissures as a fibrous ridge.

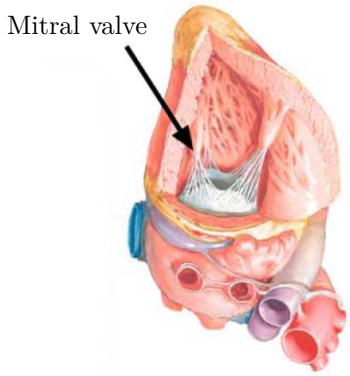


Figure I.9: Bicuspid valve [19]

#### Aortic valve

During ventricular systole, the oxygenated blood is pumped from the left ventricle to the tissues of the body through the aortic artery. During diastole, the aortic semilunar valve (Figure I.7) prevents blood to flow back to the left ventricle. Similarly to the pulmonary semilunar valve, the aortic valve is formed by three symmetric semilunar–shaped cusps which are attached to the fibrous skeleton at the root of the aorta. These cusps are named with respect to their spatial position to the body: left and right both in front of the pulmonary valve, and posterior [19].

## I.2 Intracardiac hemodynamics

Intracardiac hemodynamics allows the study of the cardiac activity according to variations in intracardiac pressures and blood flow through the valves. It thus allows to understand the timing and genesis of normal and abnormal heart sounds during contraction and relaxation phases of the cardiac cycle also known as systole and diastole phases respectively. Systole and diastole are ejection and relaxation phenomena occurring within heart cavities during the cardiac cycle. During the systolic phase, the heart ejects blood from the ventricles into the pulmonary artery and the aorta. The diastole is a relaxation phase allowing ventricles to fill up from the venous return in the atria. The basic description of the mechanical events given below about the left heart dynamics can also be applied to the right heart, taking

into consideration the lower pressures of the the right ventricle and the pulmonary artery.

In the following, the cardiac cycle is defined between two successive P waves of the electrocardiogram (ECG). The cardiac cycle can be subdivided into two main phases, namely systole and diastole phases. The systole consists of ventricular contraction and ejection, and the diastole of ventricular relaxation and filling. The cardiac cycle can also be divided into seven elementary phases: atrial systole, isovolumetric contraction, rapid ejection, reduced ejection, isovolumetric relaxation, rapid filling, and reduced filling, as depicted in Figure I.10. This partition is achieved according to the evolution of intracardiac chambers pressure as functions of time. Events in the right heart (right atrium and ventricle and pulmonary artery) are qualitatively similar to those of the left heart. The timing is similar but the pressures within the chambers of the right side of the heart are lower than those of the left side [21].

### I.2.1 Atrial systole

*AV valves open, aortic and pulmonic valves closed*

The atrium contraction corresponds to the P wave of the ECG which represents electrical depolarization of atria. This contraction increases the pressure and consequently ejects the blood from atria to ventricles passing through the open AV valves. The atrial contraction allows up to 10% of the left ventricular filling at rest, and up to 40% at high heart rates. After atrial contraction, the pressure within atria decreases to effect a gradient reversal through the AV valves. Ventricular volumes reaches their maximum values (end–diastole volume, EDV). The left ventricular end–diastolic volume (typically about 120 mL) is associated with end–diastolic pressures of 8 to 12 mmHg. The right ventricular end–diastolic pressure typically ranges from 3 to 6 mmHg. A fourth heart sound (S4) is sometimes audible owing to vibration of the ventricular wall during atrial contraction. This sound is normal in older individuals.

### I.2.2 Isovolumetric contraction

*Early systole: All valves closed*

This phase is the onset of the ventricular systole and coincides with the QRS complex of the ECG at ventricular depolarization. Consequently, the intraventricular pressure increases above atrial pressure allowing AV valves closure. These valvular events combined with blood flow within intracardiac chambers contribute in generating the first heart sound (S1), which is ordinarily split of 40 $ms$ and is formed by the mitral and the tricuspid valves closures. The intraventricular pressure rises rapidly without any ejection of blood into the aorta or pulmonary artery. The intraventricular volume remains constant during this phase which is consequently named isovolumetric contraction.

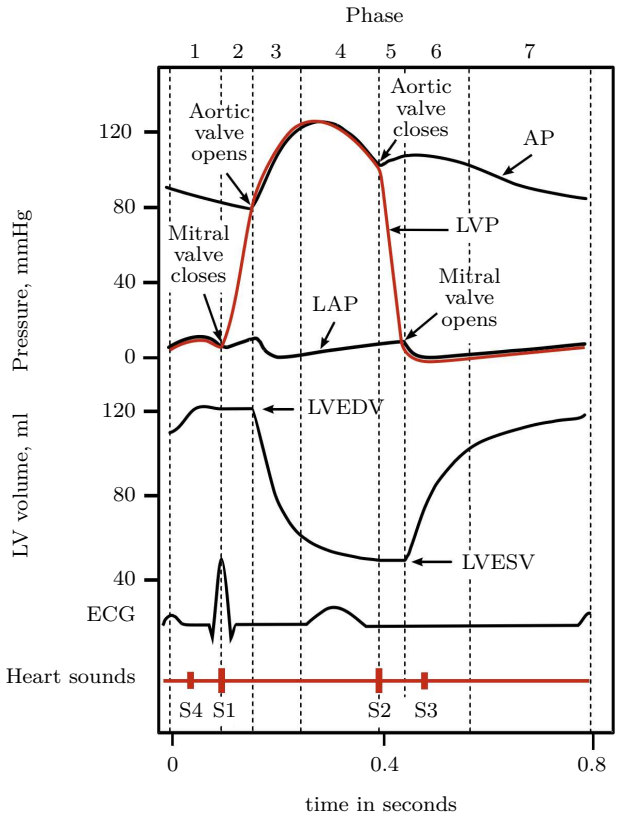


Figure I.10: Cardiac cycle phases: (1) atrial systole, (2) isovolumetric contraction, (3) rapid ejection, (4) reduced ejection, (5) isovolumetric relaxation, (6) rapid filling, and (7) reduced filling, LV: left ventricle, AP: aortic pressure, LVP: left ventricular pressure, LAP: left atrial pressure, LVEDV: left ventricular end–diastolic volume, LVESV: left ventricular end–systolic volume.

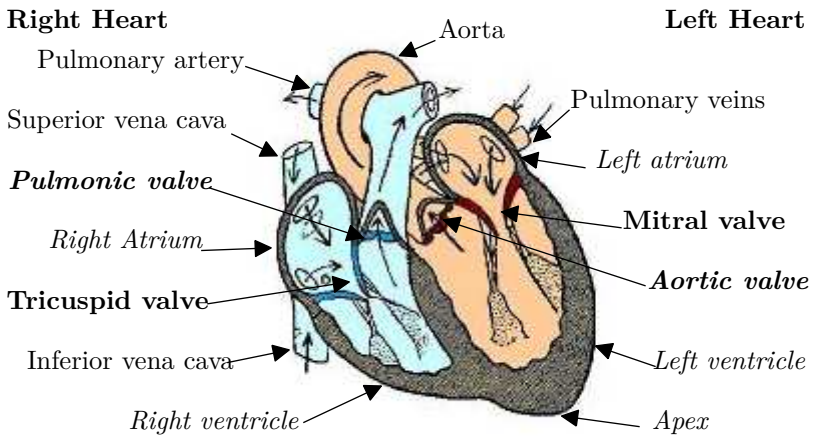


Figure I.11: Diagram of the heart

### I.2.3 Rapid ejection

*First phase of the mid systole: A and P valves open, AV valves remain closed*

As the intraventricular pressure exceeds the aorta and pulmonary artery, semilunar valves open and consequently the blood is ejected out of ventricles. After ventricular contraction and ejection of blood, the intraventricular pressure decreases. No sounds are generated during this ejection through a healthy valve which is silent during its opening. Therefore, a sound recorded during blood ejection is an indicator of a valvular pathology and is known as a murmur.

### I.2.4 Reduced ejection

*Second phase of the mid systole: A and P valves open, AV valves remain closed*

The ventricular repolarisation, corresponding to the T wave in the ECG and which occurs approximately 150 to 200 $ms$ after the QRS complex, provides a muscular relaxation which causes a slower ejection. The ventricular pressure decreases slightly below the outflow tract pressure. The outward flow persists owing to the inertial blood energy which continue pitching blood into the aorta and pulmonary artery. The atrial pressure rises again owing to the continuing venous blood inflow.

### I.2.5 Isovolumetric relaxation

*Early diastole: All valves closed*

The intraventricular pressure decreases allowing ventricles to relax. A pressure reversal occurs when this pressure is less than the outflow tracts pressure and causes closure of the aortic and the pulmonary valves (aortic before pulmonary). A second heart sound (S2) is generated and is ordinarily split.

### I.2.6 Rapid filling

*Mid diastole: AV valves open, A and P valves closed*

Ventricular pressure decreases below the atrial pressure. Therefore, atrioventricular (AV) valves open allowing ventricles to be filled up. This opening combined with the rising atrial pressure provide a passive and rapid filling of ventricles. The active relaxation of ventricles during isovolumetric relaxation provide a rapid pressure ventricular fall in comparison to the atrial pressure, which causes diastolic suction initiating the ventricular filling. Healthy AV valves are silent during the filling phase. However, the presence of a third heart sound (S3) is normal in children but is usually considered as a pathological indicator of ventricular dilation. This sound represents tensing of the supporting tissue of valve leaflets formed by the chordae tendineae and the AV ring.

### I.2.7 Reduced filling

*Diastatis: AV valves open, A and P valves closed*

The reduced filling phase corresponds to the end of the ventricular filling which makes ventricles stiffer as they continue to be filled up. The pressure gradient[15] through the AV valves fall owing to the rising of intraventricular pressure. Therefore, the ventricular filling is reduced despite the slight increase of atrial pressure owing to the venous blood flow.

## I.3 Heart auscultation

Perception of heart sounds is influenced by their production and transmission as well as the capability of the human auditive sensory system in recognising correct amplitude and frequency of each sound. The human ear is not equally responsive to sound in all frequency ranges, and has relative perception about loudness and softness of a sound. Two sounds with the same intensity at different frequencies are perceived differently. The human ear has an optimal sensitivity range between 1 and 5 kHz. This frequency range is perceived louder than an equally intense but lower frequency sound (e.g., 200 Hz) because of the ear's poor sensitivity in the lower frequency range [22].

Auditory performance of a human being is limited and requires adapted devices to achieve better cardiac auscultation. Subsection I.3.2 present the stethoscope as

[15]The pressure gradient refers to the difference between the atrial and ventricular pressures

a basic exploration device which still been used nowadays as a powerful tool in auscultating the heart. Subsection **??** presents the digital phonocardiography as an emerging technique to explore the heart activity.

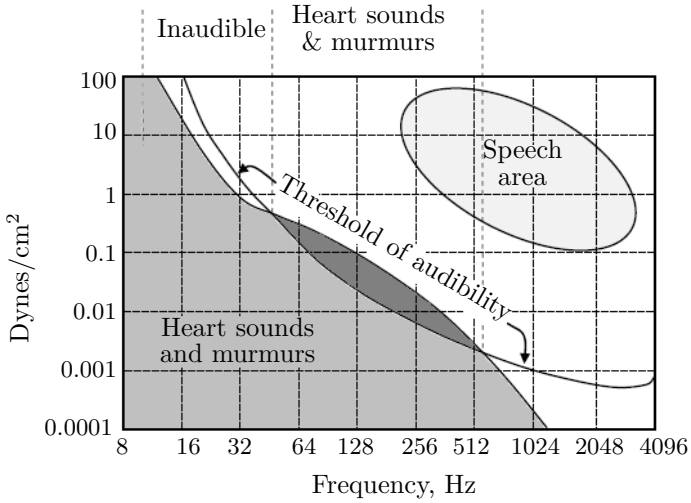


Figure I.12: Audibility of heart sounds and murmurs [23].

### I.3.1 Auscultation areas

### I.3.2 Stethoscope

In 1816, at the Necker–Enfants Malades Hospital in Paris, heart auscultation has made great strides thanks to works of Laënnec[16] who created the first stethoscope which was a simple monaural wooden tube. Despite this primitive design, René Laënnec brings a revolutionary tool to cardiologists in front of intracardiac exploration through auscultation of heart sounds and murmurs [25].

After several models proposed to explore the cardiac activity, in 1961, David Littmann, noted cardiologist and Harvard medical school professor, designed the contemporary stethoscope model. As depicted in Figure I.14, this acoustic stethoscope is mainly formed by a chestpiece, composed of a bell, a diaphragm, a binaural headpiece which allows distribution of the sound to each ear, the earpieces tips, and tubing which connects all pieces together.

[16]René Théophile Marie Hyacinthe Laënnec (1781–1826)

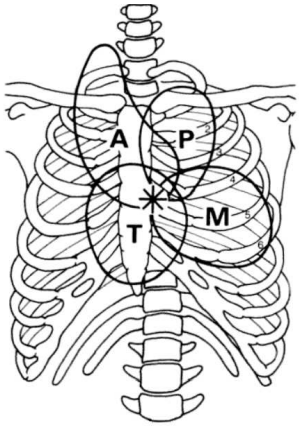


Figure I.13: Auscultation areas (* = Erb's point) [24].

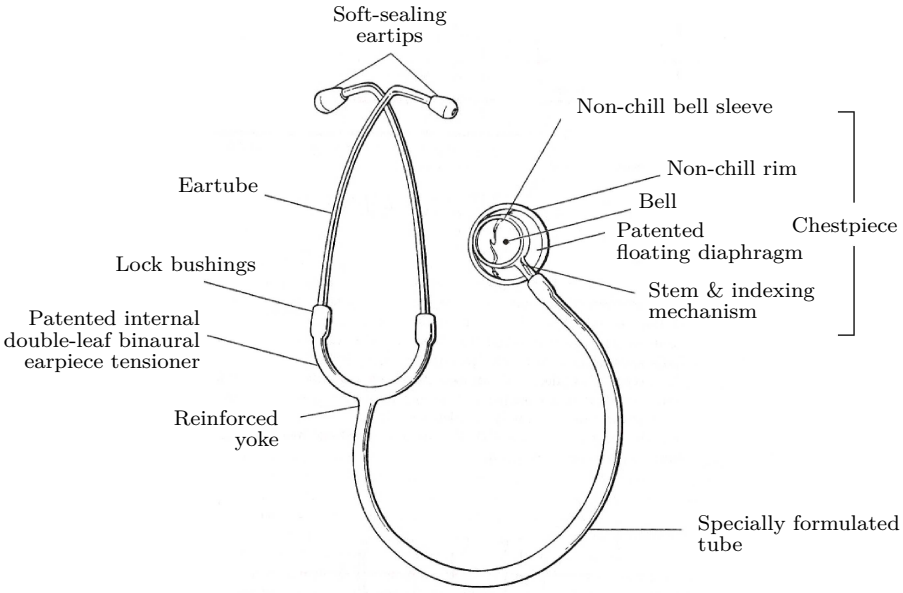


Figure I.14: Acoustic stethoscope according to the Littmann model [22].

The bell attenuates sounds of high frequency content. Indeed, the bell when held against the chestwall, in positions properly located and known as auscultation areas (Figure I.13), transmits sounds within frequency range from 20 up to 100 Hz. Sounds between 100 to 1000 Hz are slightly attenuated. The diaphragm when applied firmly

to the chest attenuates low frequency components from 20 up to 100 Hz and favours high–frequency sounds. Most stethoscopes are equipped with a bell and a diaphragm tools allowing both low and high frequencies to be perceived easily.

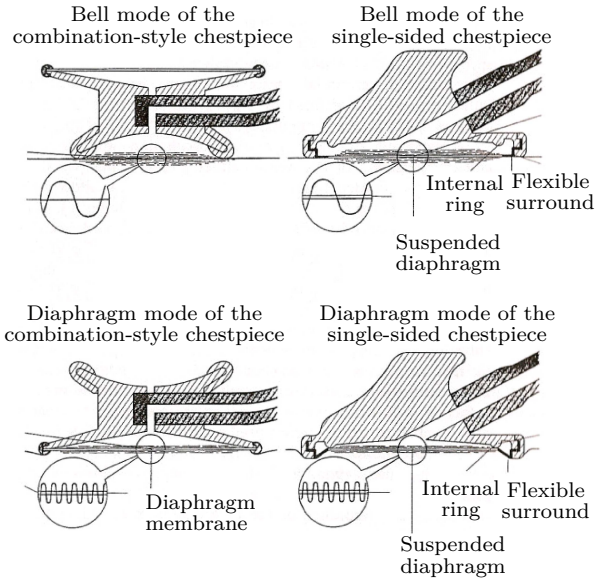


Figure I.15: Traditional and newer design of acoustic stethoscopes. On the left: a traditional design with separate bell and diaphragm (combination–style chestpiece). On the right: the 3M Littmann Master Classic stethoscope [22]

The Littmann stethoscope model has been improved by 3M[17] to combine the bell and the diaphragm tools into one single–sided chestpiece as illustrated in Figure I.15. This universal new generation binaural stethoscope allow an appropriate auscultation of the cardiac activity in both the low and high frequency ranges.

Recording heart sounds in a quiet room can help to get an attenuated effect of the ambient background noise. Another alternative is to ensure coupling by means of an ultrasound gel. A practical tip to get better auscultation experience is to use a light pressure with the bell since firm pressure will produce the effect of diaphragm.

Moreover, electronics brings supplementary improvements towards stethoscopes. Indeed, the electronic stethoscope, also known as stethophone, improves the sound quality by means of specific amplification and filtering. Sound sensing can be achieved by means of a microphone placed into the chestpiece. Recent improvements emerged incorporating wireless technology to ensure ambulatory function of

[17] American company named as *Minnesota Mining and Manufacturing Company* until 2002, now know as 3M

the auscultation device at a higher performance.

## I.4 Genesis theories of heart sounds

The genesis of heart sounds and murmurs is a challenging issue which remains a fertile research area. Indeed, this is due the ambiguous findings of several investigators during decades of scientific research. Two emerging concepts are considered as the main theories able to yield a logical elucidation behind genesis of heart sounds and murmurs. Indeed, the valvular and the cardiohemic theories arose to explain this issue but with two controversy hypotheses. The multidegree of freedom theory propounded by Durand and Guardo [18, 26] unified the two opposing concepts and merged them into a more comprehensive and coherent theory.

### I.4.1 Valvular theory

The transient vibrations produced by the sudden tension on the valve leaflets at the opening and closure of the intracardiac valves has been considered for long time as the main obvious origin of the sounds generated by the heart [27, 28, 29, 30, 31]. This is advanced as the valvular theory which stipulates that heart sounds are the direct result of the valvular cusps impact during the cardiac cycle[32, 33]. In this theory, heart sounds are considered to be formed by high–frequency components, clearly audible, which appears at closure of atrioventricular valves. The S1 and S2 heart sounds are both formed by two high–frequency audible components corresponding to halting at the end of closure of the atrioventricular (M1 then T1) and the semilunar (A2 then P2) valves leaflets, respectively. The M1 and T1 vibrations are considered as the main source of the first heart sound (S1). The third and fourth heart sounds, considered as left ventricular vibrations, are generated by halting of the mitral valve at the end of its opening. The atrioventricular pressure gradient extend the mitral valve during early and late diastole to produce low–frequency vibrations constitung the main energy within the S3 and S4 heart sounds [5].

### I.4.2 Cardiohemic theory

Rushmer [34] introduces a theory about heart sounds genesis stipulating that the blood fits within the overall heart structure to form a dynamically coupled system which vibrates synchronously to generate heart sounds. According to this theory, the blood within heart cavities and vessels is exposed to their vibrations and thereby vibrates accordingly. This theory consider intracardiac structures and blood they contain as an interdependent system which vibrates as one element. This theory assigns heart sounds to blood acceleration and deceleration within cardiac cavities and vessels and rule out any valvular vibration to form heart sounds. Thenceforth, this finding defines the cardiohemic theory, which claims that heart sounds are the contribution of intracardiac blood flow within heart cavities and vessels.

The first heart sound (S1) is considered to begin with a low frequency component appearing at the first myocardial contraction. It was realised that the intensity of the first heart sound (S1) depends significantly on the left ventricle contraction. On the basis of the cardiohemic theory, Luisada developed a research work [35]which confirms the Rushmer's theory.

Luisada studied the relation between the aortic component of the second heart sound, aortic pressure, and flow velocity as well as aortic valve closure and attributed heart sounds to the energy stored in the aortic wall of the myocardium. This energy accelerates blood flow and thereby yield deceleration of the intracardiac structures and blood they contain [36]. Luisada also reported that a change in blood volume as a consequence of dilatation or hypertrophy of the cardiac myocardial wall can induce modification on the first heart sound [37]. Luisada investigated the temporal occurrence of cardiac events through intracardiac pressure tracings in dogs and frequency selective phonocardiograms of normal human subjects [38]. He find out that large vibrations in heart sounds are due to the ejection phase.

However, Luisada recognises the valvular contribution within heart sounds [38]. Both the first and second heart sounds are formed by three vibration phases beginning by a low–frequency phase, then extended by a high–frequency phase and finished with a low–frequency phase. The first phase of the first heart sound is of low frequency content produced by the myocardial tension. Its second phase, of high frequency content, is produced by four valvular events, namely: mitral closure, tricuspid closure, pulmonic opening and aortic opening. The last phase, of low frequency content, is generated by the vascular blood inflow. The first phase of the second heart sound is of a low frequency content and is generated by vortexes appearing before the valvular closure. The second phase is of high frequency content and is due to closure of the semilunar valves. The last phase, of low frequency content, is produced by the opening of the atrioventricular valves. The rapid filling of the right ventricle occurs before that of the left ventricle.

According to this theory, the first heart sound (S1) is formed by four components. The first component begins with a low frequency component in line with the onset of myocardial contraction owing to intracardiac pressure rising. The second component, assumed to be of high frequency, results from the left ventricular structures' vibrations, the contraction of the heart, and the deceleration of blood within these cavities. The third component occurs at the opening of the aortic valve and is due to the abrupt acceleration of blood within the aorta. The fourth component is generated by the aorta inflow turbulence. The right heart is considered to have no effet on producing the first heart sound. The second heart sound is considered to be generated by the deceleration of the aorta inflow and pulmonary artery [39, 40]. The third and fourth heart sound (S3 and S4) are assumed to be formed by abrupt deceleration of intraventricular blood during early and late diastolic ventricular filling phases.

### I.4.3 Heart–thorax system

Durand *et al.* reviewed the advances in instrumentation and digital signal processing techniques applied to phonocardiography [5]. They examined the results obtained by applying spectral analysis [41, 42, 43, 44], time–frequency representations and cardiac acoustic mapping on heart sounds to better understand their genesis and transmission through the heart–thorax system.

Aubert *et al.* explored the transmission of heart sounds from the myocardium to the surface of the thorax by means of the fast Fourier transform [45, 46]. They compared the spectral content of heart sounds for both intracardiac and thoracic recordings in dogs. They found that thoracic heart sounds were a filtered version of intracardiac sounds. Moreover, thoracic heart sounds were affected by the interaction of the heart with its surrounding structures to the chest wall.

Several investigators introduced a sound source near or within heart cavities to study the sound transmission through the heart–thorax system, and confirms the effect of this system on thoracic heart sounds [18, 26, 47, 48]. Durand *et al.* introduced a system as a model of the time–varying transfer function of the heart–thorax system in dogs [18, 26, 41]. They found that the mean acoustic attenuation of the heart–thorax system for A2 is about 50 dB in dogs and humans, and about 60 dB in pigs [49]. The acoustic heart–thorax system has been characterised through spectral analysis of intracardiac and thoracic phonocardiograms. The study of the of the mitral (M1) component of the first heart sound and the aortic (A2) component of the second heart sound in dogs allows to characterise the heart–thorax system as a band–pass filter. On the calculated spectra between 20 and 100 Hz, the M1 and A2 components are attenuated at 30 dB and 46 dB, respectively. Above 100 $Hz$, the attenuation slope for M1 and A2 is at $-12dB$ and $-6dB$ per octave respectively [41].

Durand *et al.* [42] applied several surgical protocols to study the heart–thorax system in dogs and pigs. They studied the neuromuscular blockade, the sternotomy and atrioventricular pacing effects on the heart–thorax system, especially on the mitral (M1) and the aortic (A2) components in dogs. They found that the neuromuscular blockade has no effect on the attenuation effect of the heart–thorax system at the contrary to the sternotomy and the cardiac pacing. They reported attenuations of 20 dB and 11dB for M1 and A2 components, respectively. This attenuation effect disappears after a recovery of 2 weeks.

Durand *et al.* [43] established a surgical protocol to study the effect of changing the heart rate and the P–R interval on the acoustic transmission of M1 and the aortic A2 components through the heart–thorax system. This experiment, applied to seven dogs, consists in implanting a programmable sequential atrioventricular pacemaker, after destructing the bundle of His to create a chronic heart block. Durand *et al.* found that changing the P–R interval effects a considerable alteration in the intensity of the M1 component as well as a change in its transmission through the heart–thorax acoustic system. The intensity and acoustic transmission of the aortic A2 component are not affected. The M1 component is slightly affected by the heart rate variation, whereas no change is noticed on A2. Despite the variation of either

heart rate or P–R interval, the spectral contents of both intracardiac and thoracic M1 and A2 did not indicate any modification.

In a complementary study on myocardial contractility, Durand *et al.* [44] found that varying the cardiac inotropy[18] changes considerably the intensity of M1 and A2 components with no effect on their respective spectral content. It was also noticed that cardiac inotropy slightly affects the heart–thorax acoustic system.

### I.4.4 Controversy and modern concepts

The cardiohemic theory extended the investigator's mind to involve the myocardial reverberations as a significant acoustic source of the heart sounds. The valvular and cardiohemic theories are incompatible in their background hypotheses. The cardiohemic theory excluded any valvular contribution at the time of heart sounds generation. Indeed, the blood mass and the heart cavities are considered as the system which generates heart sounds. The valvular theory reduces the genesis of heart sounds to the coaptation of the four heart valves during the cardiac cycle. Several researchers investigated the origin of heart sounds with controversy finding which result in a necessary unified concept to explain the genesis of heart sounds [50, 51, 52, 53]. One of the modern investigations of heart genesis which takes into account both the cardiohemic and the valvular concepts was proposed by Ronan [54, 55]. Ronan begins his study by considering the M1 and T1 oscillations within the first heart sounds as an obvious result of the closure of mitral and tricuspid valves, respectively. In a cardiohemic viewpoint, he considers the myocardium, the valves and blood mass as an entire system since they are fitting the one to the other during the cardiac cycle. As a combination of the cardiohemic and the valvular theories, he considers the second heart sound to be formed by the closure of aortic and pulmonary valves, however, the resulting A2 and P2 acoustic components are assumed to be produced by rapid vibrations of the valves leaflets rather than their coaptation. The third and fourth heart sounds are considered to be ventricular sounds due to blood mass deceleration which effects myocardial reverberations. The third heart sound is assumed to be generated by the sudden vibration of the ventricular wall at the onset of ventricular diastole. Similarly, the fourth heart sound is due to atrial contraction.

### I.4.5 Multidegree of freedom theory

The previous sections obviously highlights that leaflets of intracardiac valves vibrates at their resonant frequencies within the blood. This is incompatible with cardiohemic theory that stipulates that the incompressibility of the blood is the main reason behind heart sounds genesis with no valvular contribution. Durand *et al.* [49] studied the acoustic transmission system of intracardiac blood, and found that it is negligible below 20Hz and rises above 60Hz up to 20dB. Therefore, the cardiohemic system is valid only for low–frequency components (below 60Hz) of heart sounds. Indeed, a complementary concept should be theorised to explain the

[18] by using injections or infusions of cardiotonic drugs: Dobutamine, Betalol and Quinidine

high–frequency content (above 60Hz) of heart sounds. Durand and Guardo [18, 26] propounded the multidegree of freedon theory which considers the heart as a system which transform the biochemical energy of the blood into mechanical and acoustical energy and heat. This theory merged both valvular and cardiohemic concepts. This theory stipulates that the heart is a multidegree of freedom viscoelastic system assumed to generate heart sounds as a result of vibrations of its internal structures as well as turbulence of the blood mass. Therefore, the produced heart sounds should be multicomponent signal rather than monocomponent as advanced previously by the cardiohemic theory. Indeed, the heart sounds are assumed to be the direct result of pressure fluctuations around the valves leaflets, cordae tendinae, and myocardium as well as turbulences in the intracardiac blood mass. Thus, the phonocardiogram is formed by vibrations of intracardiac structures which are of different resonance modes. Moreover, the intensity and spectral content of the thoracic phonocardiogram depends on the heart–thorax acoustic system. The electrocardiogram (ECG) signal, considered as a triggering signal, modulates vibrations of the heart–thorax acoustic system.

The multidegree of freedom theory can be summarised as follows. Any vibrations below 60Hz is due to the intracardiac structures motions as a whole owing to the incompressibility of blood mass. Above 60Hz, the intracardiac structures (valve leaflets, cordae tendinae, etc.) can vibrate according to their own resonance modes.

The proposed transfer function comprises 3 modules, namely; the myocardial, respiratory, and chest–wall systems organised successively from the myocardium to the chest wall [5].

### Myocardial system

The myocardial system is responsible for producing fluctuations of intracardiac structures tensions and blood turbulences. The myocardium, with its spatially distributed sources, change rapidly and therefore should be represented by a fast time–varying impulse response. Vibrations of intracardiac structures produce heart sounds, which are deterministic signals, as an input of the heart–thorax system. These sounds are transient signals. Valve leaflets and blood masses are considered as inputs which generate transient components M1, T1, A2, P2 and musical murmurs. Stenosis and regurgitant murmurs are random signals produced by blood mass turbulences through abnormal valves. The location of the generated vortexes within the myocardium depends on the cardiac abnormality. Another possible nature of signals is harmonic vibrations known as musical murmurs which are generated under pathological conditions.

### Respiratory system

The second module, the respiratory system, represents the effect of the lungs on heart sounds which affects heart sounds and murmurs timing according the respiration cycle. The respiratory system can also affect the acoustic transmission of heart

sounds and murmurs through the heart–thorax system. The respiratory system is represented by a slow time–varying impulse response owing to its slow effect in comparison to the timing of intracardiac events.

#### Chest–wall system

The last module, the chest–wall system which is formed by thoracic tissues and bones, is the more passive module. This system has an attenuation effect modulated by the respiratory system, but is considered as time–invariant system owing to the short durations of heart sounds and murmurs.

## I.5 Sounds of intracardiac vibrations

In this section, electronic resources [24, 1] of cardiac auscultation tutorials designed of auscultation training purposes are used to study the various cardiac disorders through their phonocardiographic recordings.

### I.5.1 Timing of heart sounds

The heart, during its continuous cyclic beating, generates sounds recorded as phonocardiogram (PCG) signal. The phonocardiogram of a healthy subject can record up to four sounds, which are not all audible (Figure I.12). A normal phonocardiogram is usually formed by S1 and S2 sounds during a cardiac cycle as depicted in Figure I.16. These sounds appears at the onset of the systole and the diastole phases respectively.

The sinusal node is closer to the tricuspid valve in comparison to the mitral valve. Consequently, the right atrial contraction leads up to the left one. Therefore, the left and right hearts are not synchronised, as are their generated sounds.

Interestingly, the contraction of the left ventricle begins and finishes before that of the right ventricle. These electromechanical events generate sounds appearing at different moments of time during the cardiac cycle. This timing is of great importance in diagnosis assessment.

#### First heart sound S1

**Origins of S1** The first heart sound is generated by intracardiac events associated with closure of the mitral and the tricuspid valves, termed M1 and T1 respectively, as well as the blood mass flow through the stretched leaflets of these atrioventricular valves during closure (section I.4). During the isovolumetric ventricular contraction, the flexible curtains of the atrioventricular valves ensure impact of the leaflets and move toward the atrium. The papillary muscle and cordae tendinae suddenly block this blood mass at the elastic limit of the valvular leaflets and produces a shock wave perceived louder at the apex. At the onset of the systole, the left ventricle contracts

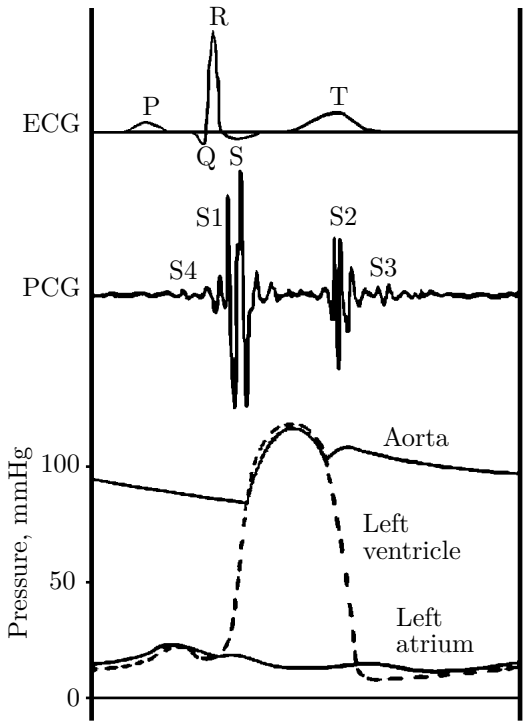


Figure I.16: Temporal relationship between the Electrocardiogram (ECG), the Phonocardiogram (PCG) and left atrial, left ventricular, and aortic pressures. From [18], reprinted with permission from IEEE, (© 1982 IEEE).

which rises its intern pressure to exceed the left atrial pressure. This event shut the mitral valve to produce the first heart sound S1. The left ventricular pressure increases to above the pressure within the aorta which allow the opening of the aortic valve.

**Normal S1 heart sound** The T1 component is softer than M1, and can be best heard at the left lower sternal border of the chest. The M1 component is the main component of S1 since intracardiac pressure within the left ventricle is much higher than that of the right ventricle where T1 is produced. Under normal conditions, the first heart sound S1 is louder than S2 when auscultated at the apex. The intensity of S1 is influenced by intraventricular pressure, structure of the valve leaflets as well as their position at the beginning of the systole. The intensity of S1 sound can be louder than S2 at the cardiac base. For instance, under increased contractility and myocardial tension in hyperkinetic states which can occur in anemia, pregnancy, anxiety, hyperthyroidism, and fever. Or under mitral valve leaflet thickening and

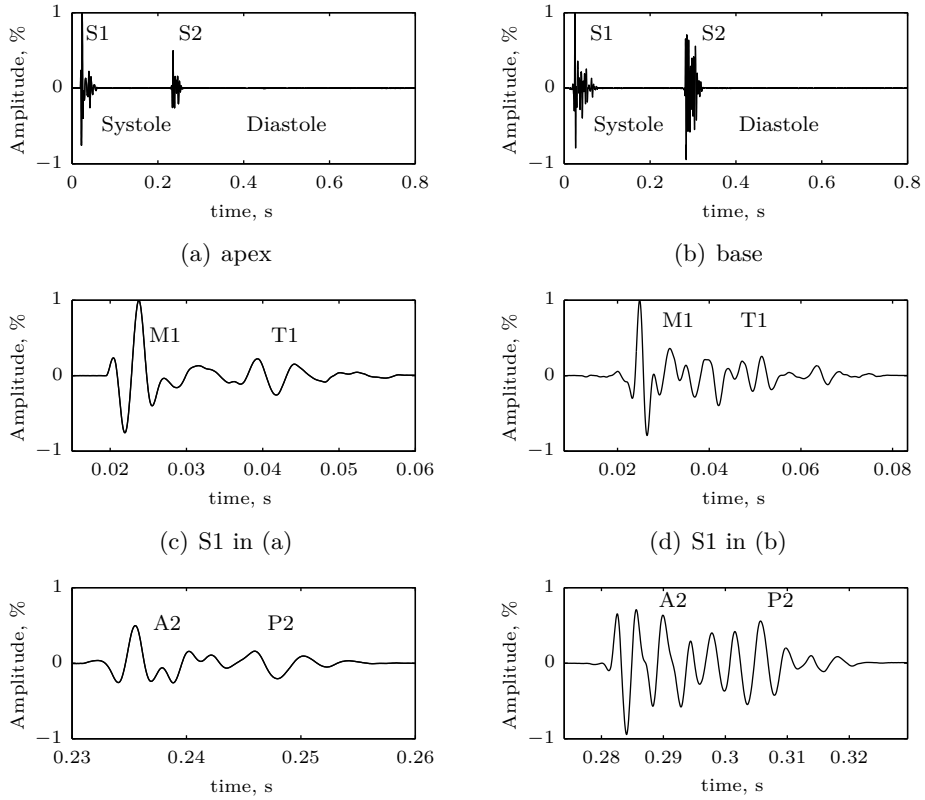


(a) apex (b) base

(c) S1 in (a) (d) S1 in (b)

(e) S2 in (a): soft (f) S2 in (b): loud

Figure I.17: One cycle PCG signal recorded at the (a) apex and (b) base of the heart. First heart sounds S1 in (c) and (d) and second heart sounds S2 in (e) and (f) correspond to PCG signals in (a) and (b), respectively. The S2 in (f) is louder at the base in comparison to that recorded at the apex in (e) [1]

scarring despite a certain valve mobility. This conditions are related to mitral stenosis. The S1 sound can be of reduced intensity when S2 is louder at the cardiac apex, for instance; in congestive heart failure owing to the insufficient ventricular contractility and the reduced intracardiac tension, or in severe mitral stenosis owing to an immobile mitral valve.

The intensity of S1 can change from cycle to cycle owing to variability of the atrioventricular valves position. This variability can occur in atrial fibrillation, third degree heart block, and patients with ventricular demand pacemakers. Therefore, atrioventricular valves at the onset of the systole can be partially shut or completely open, since the atrial and ventricular contraction are not synchronised.

Splitting of S1 is uncommon in normal subjects owing to the low intensity sound of the tricuspid valve closure in comparison to that of the mitral valve. Splitting of S1 into two components (mitral and tricuspid) of approximately 30 ms, can be localised at the tricuspid auscultation area (lower left sternal border) to favour the tricuspid valve closure to be well heard. A split sound, which can be heard at the

cardiac apex, usually formed by an atrial sound (S4) plus mitral valve closure sound, or a mitral valve closure plus an ejection sound, should not be confused with a split S1 sound. A wide splitting of S1 can occur in pathological cases owing to a delayed tricuspid valve closure, for instance in right bundle branch block (RBBB).

Luisada *et al.* studied the duration of heart sounds in 185 normal subjects [39]. The results they obtained are depicted in Table I.1. The duration of S1 is around 100 ms [39, 56].

| age (years) | S1 | | S2 | |
|---|---|---|---|---|
| | Max | Min | Max | Min |
| 11–20 | 160 | 120 | 120 | 80 |
| 21–40 | 220 | 90 | 180 | 40 |
| 41–60 | 220 | 70 | 160 | 50 |

(b)

| age (years) | S1 | | S2 | |
|---|---|---|---|---|
| | Max | Min | Max | Min |
| 11–20 | 160 | 110 | 120 | 80 |
| 21–40 | 220 | 100 | 160 | 80 |
| 41–60 | 200 | 90 | 140 | 60 |

(b)

| Auscultation area | S1 | S2 | S3 |
|---|---|---|---|
| Apex | 146 | 104 | 59 |
| Aortic | 140 | 97 | 42 |

(c)

Table I.1: Extreme durations, in milliseconds, of S1 and S2 recorded from the (a) apex and the (b) aortic area, and (c) average durations of S1, S2, and S3 for the overall age groups

**Split S1 heart sound** Splitting of S1 is uncommon in normal subjects owing to the low intensity sound of the tricuspid valve closure in comparison to that of the mitral valve. Splitting of S1 into two components (mitral and tricuspid) of approximately 30 ms, can be localised at the tricuspid auscultation area (lower left sternal border) to favour the tricuspid valve closure to be well heard. A split sound, which can be heard at the cardiac apex, usually formed by an atrial sound (S4) plus and mitral valve closure sound, or a mitral valve closure plus an ejection sound, should not be confused with a split S1 sound. A wide splitting of S1 can occur in pathological cases owing to a delayed tricuspid valve closure, for instance in right bundle branch block (RBBB).

Deceleration of the intracardiac blood mass contributes in generating the heart sound which the intensity is correlated with the created pressure momentum. The first sound S1 is mainly formed by blood mass flow through the stretched leaflets of both mitral and tricuspid valves during closure (section I.4). During the isovolumetric ventricular contraction, flexible curtains of atrioventricular valves ensure impact of the leaflets and move toward the atrium. The papillary muscle and cordae tendinae suddenly block this blood mass at the elastic limit of the valvular leaflets. This

event produces a shock wave at the apex which is the best auscultation area of the first heart sound.

The second heart sound is generated by blood outflow returning from the aortic and pulmonary trunks when semilunar valves reaches their elastic limits. The produced shock wave is generated toward the base of the heart, where the second heart sound is best heard.

### Second heart sound S2

**Origins of S2 heart sound** The second heart sound S2 is generated by intracardiac events associated with closure of the aortic and pulmonary valves termed A2 and P2 respectively. The A2 component is louder than P2 owing to the higher intracardiac pressure of the left ventricle in comparison with the right ventricle. Therefore, the aortic A2 component radiates in all auscultation areas, and is louder at the right upper sternal border. The pulmonary P2 component can be heard only at the left upper sternal border. Thus, the A2 component constituted the major energy of the second heart sound S2. The second heart sound is generated of blood outflow returning from the aortic and pulmonary trunks when the semilunar valves reaches their elastic limits. The produced shock wave is generated toward the base of the heart, where the second heart sound is best heard. The S2 sound is produced by the aortic valve at the onset of the diastole when the left ventricular pressure drops below the aortic pressure.

**Normal S2 heart sound** The S2 sound is of high–frequency content and shorter in duration than the S1 sound. At the cardiac base (second intercostal space), S2 is louder than S1. The right ventricular ejection covers the left ventricular ejection in duration. Indeed, the right ventricular ejection begins the first and ends the last in comparison to the left ventricular ejection. Thus, the pulmonary valve closure (P2) occurs after the aortic valve closure (A2). The first component (A2) is associated with closure of the aortic valve. The A2 component is the louder of the two components, and is readily heard in the second right intercostal space, the second and third left intercostal spaces, the lower left sternal border, and at the cardiac apex. The second component (P2) is associated with closure of the pulmonic valve. Because P2 is softer than A2, P2 is normally heard only at the second or third left intercostal spaces. P2 may increase in intensity as a result of pulmonary hypertension, and then may be heard along the lower left sternal border and at the cardiac apex. When S2 is increased in intensity, it will be louder than S1 at the cardiac apex. If S2 heart sound is louder than S1 heart sound at the apex, and if splitting of S2 is heard at the apex, then pulmonary hypertension is likely confirmed. Both A2 and P2 components lasts less than 60 ms [39] (table I.1).

**Split S2 heart sound** The S2 heart sound can be separated into two components in relation to aortic and pulmonary valves closures. This phenomenon can be observed in individuals less than 50 years old rather than older subjects. A split S2

can be best heard at pulmonic auscultation area (left upper sternal border). Split of the S2 heart sound can be persistent (widened), fixed, or paradoxical (reversed).

**Physiologic split of S2 heart sound**

In normal subjects, the aortic A2 component occurs before P2. A physiological split of S2 is confirmed when the P2 component is delayed to be easily differentiated from the A2 component. The usual cause of the physiological split of S2 is inspiration, which increases the venous blood returning to the right heart. Thus, the closure of the pulmonary valve is delayed, and the aortic closure is accelerated.

The rising pulmonary compliance during inspiration affects closure of the pulmonary valve. By inspiration, more blood fills up the right heart cavities and therefore increases the right ventricular output into more compliant lungs. Expiration restrains the right heart filling and inversely favours left heart filling by applying positive pressure on the lungs. Expiration reduces this effect and the split of the S2 sound becomes narrower. The S2 split can be best heard at the pulmonary area to favour the pulmonary P2 component which is softer than A2.

Splitting of S2 heart sound is qualified as physiologic in normal subjects when the time separating the aortic and pulmonary closures widens during inspiration. The delay is primarily related to late closure of the pulmonic valve during inspiration. The intrathoracic pressure fades during inspiration which rises the capacitance of the pulmonary vascular bed. Consequently, the pulmonary vascular impedance decreases and pulmonary vessels open. Therefore, the right ventricular ejectional inflow lasts longer than usual. Thus, the pulmonic valve closure, which generates P2, arises lately until the forward blood flow vanishes. The S2 is split and expanded to 40 up to 50 ms and best heard at the left intercostal space. The pulmonary vascular capacitance fades as the pulmonary vessels closes as a result of the rising intrathoracic pressure during expiration. Consequently, the pulmonic vascular impedance rises which reduces the forward blood flow from right ventricular ejection. Therefore, the S2 heart sound is perceived as a single sound with a narrow A2–P2 split at 10 up to 20 ms.

A wide physiologic splitting of the S2 sound can be related to a delayed pulmonary valve closure or an early aortic valve closure. During inspiration, the split can reach 60 ms, and on expiration it decreases to 30–40 ms. Physiologic splitting is observed under conditions that expand the right ventricular ejection (*e.g.* pulmonary stenosis), delay the beginning of the right ventricular ejection (*e.g.* RBBB), or reduce the left ventricular ejection (*e.g.* mitral regurgitation, or VSD).

**Paradoxical splitting of S2 heart sound**

A paradoxical split of S2 (Figure I.19) occurs when the split of S2 sound is recorded only in expiration. This happens when the aortic A2 closure is delayed to merge with the pulmonary P2 closure. Several abnormalities can cause this split, such as a severe aortic stenosis, a hypertrophic obstructive cardiomyopathy (HOCM), or a left bundle branch block (LBBB). Reversed (paradoxic) split results from an extended left ventricular ejection which permutes the order of S2 components, so that A2 occurs after P2. Thus, the S2 split narrows with inspiration and

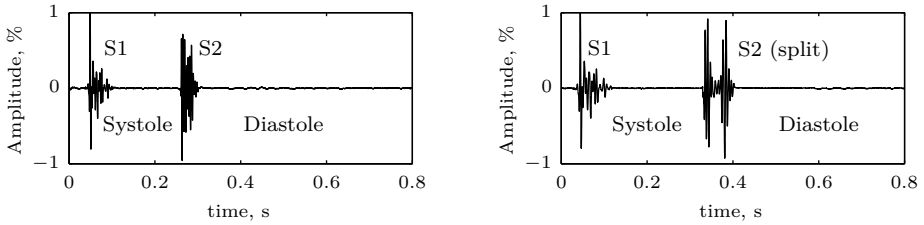


(a) S2: no split

(b) S2: physiological split (inspiration)

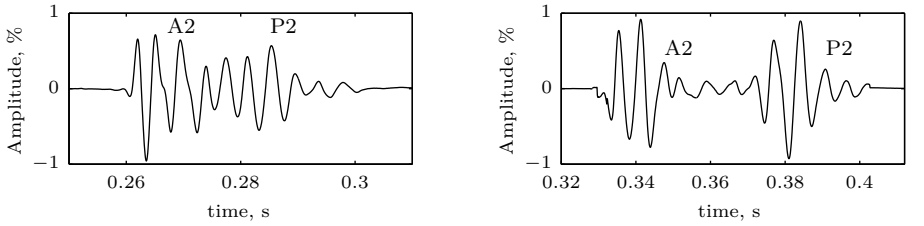


(c) S2 in (a): merged A2 & P2

(d) S2 in (b): split A2 & P2

Figure I.18: Physiological split of S2. (a): unsplit S2 during normal respiration, (b): split S2 during inspiration, (c): S2 in (a); A2 & P2 are merged, (d): S2 in (b); P2 is delayed from A2 [1]

widens with expiration.

A reversed splitting S2 can be observed in patients with aortic stenosis, Hypertrophic cardiomyopathy[19], and severe systemic hypertension. The common pathology behind reversed splitting of S2 is left bundle branch block.

**Pathological split** The wide fixed splitting of S2 heart sound is not variable with respiration, and is audible in both inspiration and expiration. This kind of split of S2 is related to atrial ventricular septal defects. In atrial septal defects, the left to right blood shunt results an exceed in the right ventricular forward cardiac output over that of the left ventricle. Consequently, the pulmonary vascular capacitance is independent of breathing and remains always high.

Therefore, the pulmonary vascular capacitance, which still unchanged by breathing, reduces considerably the pulmonary vascular impedance below normal values. The length right ventricular ejection which is due to the right ventricular ejection induces a wide split. The S2 heart sound shows a split as a result of two mechanisms.

When the pulmonary vascular impedance is below normal values, then respiration has a tiny effect on the duration of the right ventricular ejection blood flow. In septal defects, blood has two different ways to go back to the right heart. The first path is ensured by the great veins. The second one is to go from the left chambers of the heart through the septum hole. During inspiration, an equilibrium is maintained between the rising systemic venous and the decreasing shunted septal defect volumes.

[19]also known as Idiopathic hypertrophic subaortic stenosis (IHSS)

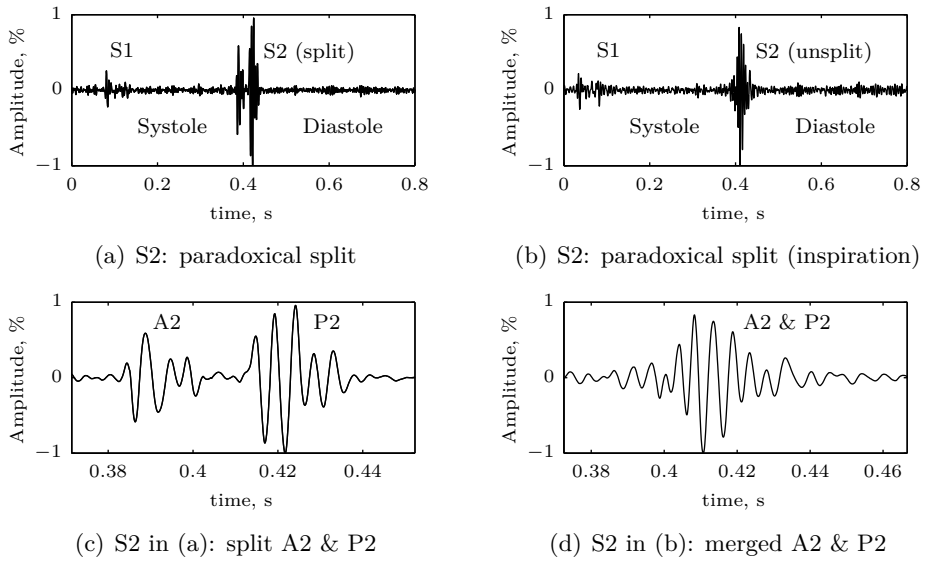


(a) S2: paradoxical split

(b) S2: paradoxical split (inspiration)

(c) S2 in (a): split A2 & P2

(d) S2 in (b): merged A2 & P2

Figure I.19: Paradoxical split of S2. (a): paradoxical split of S2 during normal respiration, (b): S2 merged during inspiration, (c): S2 in (a), (d): S2 in (b) [1].

Consequently, the right ventricle incoming blood flow is constant and the duration of the right ventricular ejection is fixed.

A tapered physiological split is a sign of severe pulmonary hypertension. In that case, pulmonary vascular resistance rises as well as the amplitude of the P2 sound component due to the shortened right ventricular ejection. However, a wide split of the S2 heart sound occurs at the early right ventricle failure.

Both A2 and P2 components lasts less than 60 ms [39]. Luisada *et al.* studied the duration of heart sounds in 185 normal subjects [39](Table I.1).

### Third heart sound S3

A third heart sound, termed S3 (Figure I.20), can be heard if an important amount of blood fills a very compliant left ventricle. When the mitral valve opens to allow a passive filling of the left ventricle, an S3 sound occurs. This sound is also known as *ventricular gallop*. The S3 sound cannot be auscultated in normal cardiac output in adults owing to the usually noncompliant left ventricle. However, this sound can be recorded in children, pregnant females and athletes. In pathological context, the S3 sound can be an indicator of a systolic heart failure. Indeed, an overcompliance of the myocardium effects a dilation of the left ventricle. The S3 sound is of low–frequency content in comparison to S2. This is helpful to distinguish it from a neighbouring split S2 sound. The S3 sound is auscultated best at the apex, and to favour its auscultation, the patient should be in left lateral decubitus position. A rapid left ventricular filling occurs in early diastole after mitral valve opening. The ventricular wall decelerates the ejected blood mass. In young adults and children,

the created blood turbulence may produce an S3 heart sound. In old adults, an S3 heart sound is observed as a result of variation in ventricular compliance.

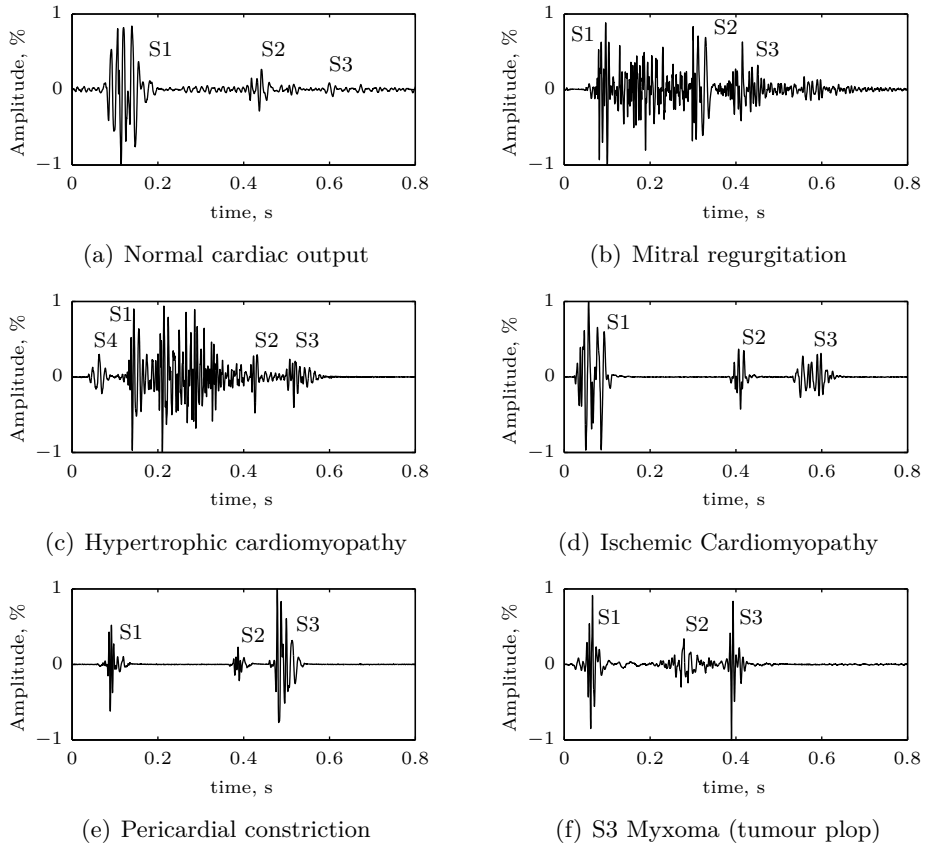


(a) Normal cardiac output

(b) Mitral regurgitation

(c) Hypertrophic cardiomyopathy

(d) Ischemic Cardiomyopathy

(e) Pericardial constriction

(f) S3 Myxoma (tumour plop)

Figure I.20: Third heart sound (S3) [1]

The S3 heart sound can be observed in early diastole after S2 heart sound at around 120 up to 200 ms. This sound is also known as protodiastolic gallop. The S3 heart sound is considered as a pathological sign in people over forty years old, and normally occurs in younger people. For better auscultation, the patient should be placed in left decubitus position to get a high amplitude S3 heart sound when originated from the left ventricle. A higher S3 heart sound can then be heard at the apex. When the right ventricle is the origin of that sound, a better auscultation can then be carried out from $4^{\text{th}}$ left intercostal space near the sternum. The third heart sound (S3) is of low frequency content and should be auscultated by the bell of the stethoscope.

When the S3 heart sound occurs at the end of the early ventricular filling, it is originated from the impact of the heart against the internal chest wall. However, this sound can occur during the early diastolic filling when blood inflow reaches an overfilled ventricle, *e.g.* in congestive heart failure or valvular regurgitation. The amplitude of S3 heart sound can be increased as a result of movements that rises the venous return (*e.g.* leg elevation). Moreover, its timing moves closer to S2 heart

sound.

The S3 heart sound occurs in several pathological cases, as follows;

**Mitral Regurgitation: Third Sound and Diastolic Rumble** Under severe systolic backflow, a considerable regurgitated blood inflow returns rapidly to the ventricle. Therefore, the mitral regurgitation causes a holosystolic murmur as well as a mid–diastolic rumble and an S3 heart sound (Figure I.20(b)).

**Hypertrophic Cardiomyopathy** The rapidly ejected left ventricular blood causes mitral regurgitation perceived as a systolic murmur. An S3 heart sound is produced under mitral regurgitated diastolic inflow going back to the ventricle which returns to its passive capacity. An atrial contraction augments the ventricular volume and produces a presystolic S4 heart sound (Figure I.20(c)).

**Ischemic Cardiomyopathy** An S3 heart sound is produced by the resistance of the dilated ventricle to passive filling. This ventricular dysfunction, which is similar to dilated cardiomyopathy, causes lower ejection (Figure I.20(d)).

**Pericardial Constriction: Pericardial Knock** The passive filling of a restricted ventricle by endomyocardial disease or constrictive pericarditis generates an S3 heart sound. In constrictive pericarditis, the S3 heart sound is sharper than usual thud sound of a full ventricle and thus is also described as pericardial knock. A pericardial knock produced by the right ventricle usually rises with inspiration (Figure I.20(e)).

**Myxoma: Tumour Plop** A left atrial myxoma[20] produces an S3 heart sound. The left atrial myxoma moves to and fro from the atrium to the ventricle through the mitral valve. Movement of this tumour produces an S3 heart sound which is known as "tumour plop" (Figure I.20(f)).

### Fourth heart sound S4

The fourth heart sound, termed S4 (Figure I.21), also known as atrial gallop or presystolic gallop, occurs 40 up to 120 ms earlier to S1. This sound occurs as a result of a forceful late atrial contraction which initiates the ventricular contraction due to the venous return at the limit of ventricular distensibility. The presence of S4 may be considered as a pathological variation in ventricular compliance. Indeed, the S4 heart sound is produced by blood mass impact within a stiff and non–compliant ventricle.

Therefore, the ventricular stiffness is a pathological sign of ventricular hypertrophy (Figure I.21(a)), as usually observed in pulmonary or systemic hypertension,

[20] gelatinous tumour attached to the atrial septum.

pulmonic or aortic stenosis, as well as a persistent aftereffect of myocardial infarction. The left ventricle is affected by hypertrophy in hypertension, aortic stenosis or hypertrophic cardiomyopathy (Figure I.21(b) & section I.5.1), or a right ventricle with pulmonary stenosis or pulmonary hypertension.

The S4 heart sound can be best heard at the apex when produced by the left ventricle, and loudest at the 4th left intercostal space adjacent to the sternum when generated by the right ventricle. This atrial sound is low pitched and occurs in late diastole. This sound disappears with standing, is rarely observed in normal subjects, and is always absent in patients with atrial fibrillation.

The left sided S4 is differentiated from a split S1 through their respective auscultation areas. Indeed, a split S1 loudest at the LSB, whilst S4 is best heard at the apex.

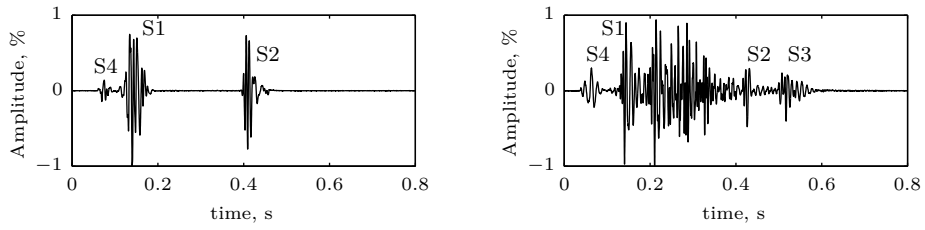


(a) Hypertensive ventricle (b) Hypertrophic cardiomyopathy

Figure I.21: Fourth heart sound S4: (a) Hypertensive ventricle, (b) Hypertrophic cardiomyopathy (same as I.20(c)) [1]

### Extra–systolic sounds

Extra–systolic sounds can be categorised into two classes; ejection sounds and mid–systolic clicks. The ejection sounds are produced by pulmonic or aortic stenosis which can be observed during early systole. Mid–systolic clicks are perceived in mitral or tricuspid valve prolapse during late systole. The sounds of both classes are high pitched and are generated under abrupt valvular stretching at their highest distensibility.

**Ejection sounds** Ejection sounds occurs just after S1 at 40 up to 60 ms,ăăand are high pitched with a short duration. These sounds are described to be vascular when caused by ejection of blood into great vessels, and valvular when generated by aortic or pulmonary valves reaching their elastic limits. In pulmonic stenosis, the ejection sound is perceived at the 2nd or the 3rd intercostal space and decreases with inspiration. In aortic stenosis, the ejection sound is best heard at the apex and 2nd right intercostal space. A murmur is always pathological when associated to an ejection sound.

Ejection sounds, also known as ejection click, occurs in bicuspid aortic valve, pulmonic stenosis, or in aortic stenosis.

**Bicuspid aortic valve** The blood mass ejected from the ventricle under aortic or pulmonic stenosis causes a loud and sharp ejection sound occurring just after S1. Therefore, the S1 first heart sound is heard as split. A mid–systolic murmur occurs as a result of blood turbulence across the stenosed valve (Figure I.22(a)).

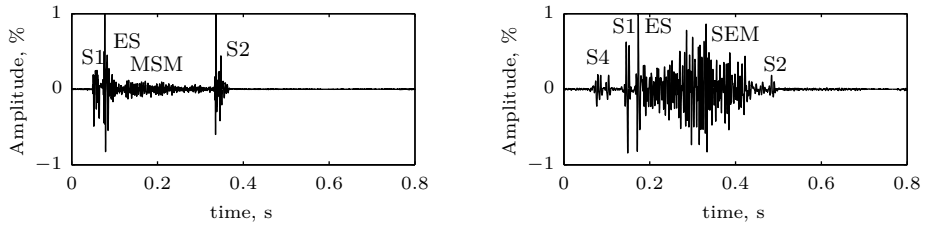


(a) Bicuspid aortic valve (b) Pulmonic stenosis

Figure I.22: Ejection sounds: (a) Bicuspid aortic valve, (b) Pulmonic stenosis [1].

**Pulmonic stenosis** The ventricular ejection exerts pressure on the valve leaflets to form a dome which decelerates the blood mass. An ejection sound occurs nearly merged with S1when the right ventricular diastolic pressure is augmented by hypertrophy and a high inspiration to surpass pulmonary arterial diastolic pressure. The ejection sound is completely merged with S1 during inspiration, and heard just after S1 with help expiration. An S4 heart sound, mid–systolic murmur, and soft and delayed pulmonary component are also perceived in conjunction with the ejection sound (Figure I.22(b)).

**Aortic regurgitation** The S1 heart sound is split and best heard at the apex. In aortic regurgitation, the ejection sound is attributed to opening of the aortic valve leaflets and for the rapid extension of the aortic root during the ventricular ejection. This ejection sound is very similar to that of the aortic stenosis. An early diastolic murmur also occurs and is loudest at the left sternal border (Figure I.23).

**Mid–systolic clicks** The mid–systolic click (MSC) is high pitched and is generated by the extension of the chordae tendineae in mitral or tricuspid valve prolapse.

**Mobile Click: Standing and Squatting** A systolic click occurs as a consequence of expanded blood systolic volume exerted on competent prolapsed valves. The mobile click is very similar to an ejection sound. Postural manoeuvres moves mobile clicks, whilst ejections sounds remains without any timing effect. Standing reduces the left ventricle cavity size, and therefore increases the disproportion between the valve and the ventricle. When the separation is short, then the valve inflates in early systole and attains its upper limit expansion in mid systole to produce the click sound. Inversely, squatting delays the click to the late systole due to the ventricular volume rising and the yellow callipers[21] expansion (Figure I.24).

[21]The yellow callipers measure the distance between the annulus and papillary muscle.

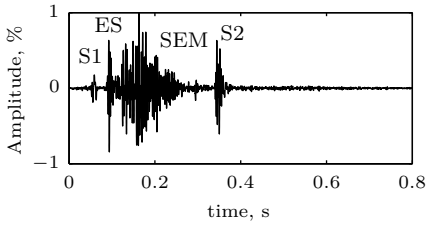


(a) Aortic area

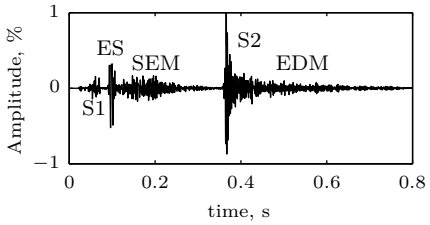


(b) $4^{\text{th}}$ left intercostal space

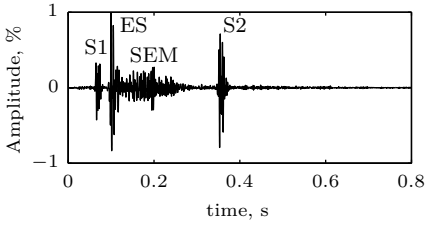


(c) Apex

Figure I.23: Ejection sounds: Aortic regurgitation. (a): Aortic area; Ejection sound (ES) + Systolic ejection murmur (SEM), (b): $4^{\text{th}}$ left intercostal space; ES + SEM + Early diastolic murmur (EDM), (c): Apex; ES + SEM [1].

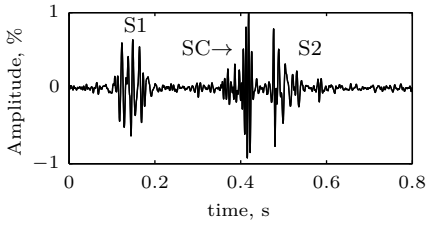


(a) Moving click: squatting

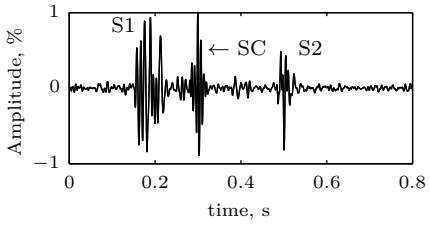


(b) Moving click: standing

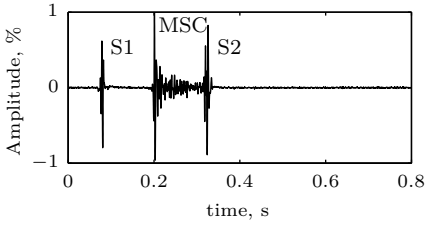


(c) Mitral valve prolapse

Figure I.24: Mid–systolic clicks. (a): Moving click: squatting, (b): Moving click: standing, (c): Mitral valve prolapse [1].

**Mitral prolapse** The non–ejection click is caused by prolapse of the thickened mitral valve into the left atrium, and occurs in mid or late systole. In contrast to ejection sounds, the non–ejection click appears at various timings according to fluctuations in ventricular filling which may result from respiration or postural manoeuvres (standing, squatting, etc.). A late murmur occurs after the non–ejection

click as a results of severe mitral valve prolapse when the mitral valve becomes incompetent.

#### Opening sounds

The opening snap (OS) occurs in early diastole immediately after A2 at 30 up to 150 ms. The OS is a high pitched sound caused by opening of mitral or tricuspid valves in mitral or tricuspid stenosis, respectively. In mitral stenosis, the OS is auscultated between the lower left sternal border and the apex, and is loudest at the $3^{rd}$ left intercostal space. In tricuspid stenosis, the OS is best heard at the $4^{th}$ intercostal space at the left sternal border.

An OS can be distinguished from the second component of a splitting S2 by two clues. The OS is louder at the apex than at the $2^{nd}$ left intercostal space. The time delay before the OS up to S2 rises on standing.

### I.5.2 Timing of murmurs

Heart murmurs have various shapes and timing during the cardiac cycle. Indeed, a heart murmur can occur in systole (*e.g.* systolic in aortic stenosis and mitral regurgitation) or in diastole (*e.g.* aortic regurgitation and mitral stenosis). Heart murmurs can also be continuous such for patent ductus arteriosus.

#### Systolic murmurs

Systolic murmurs have several shapes with regard to their localisation upon the chest of the patient as well as their timing within the cardiac cycle (Figure I.25).

The timing of a systolic murmur within the cardiac cycle as well as its high intensity auscultation area over the chest determines which pathology is originating it. For instance, early systolic or holosystolic murmurs can be generated by mitral or tricuspid regurgitation, ventricular septal defect, or probably pulmonic stenosis. Ejection murmurs, also known as mid systolic murmurs, are caused by the high outflow velocity or the obstruction of the ventricular outflow.

Late systolic murmurs which reaches their highest intensity at the late systole phase can occur as a result of the mitral prolapse or the hypertrophic cardiomyopathy. This is due to the disproportion between the valve and the ventricle that is soared during the systole when the ventricle attains its minimal volume capacity.

**Early systolic murmurs** An early systolic murmur, also known as pansystolic or holosystolic murmur, starts with S1 and stops at S2, without a gap between murmur and heart sounds. Holosystolic murmurs, also described as pansystolic, occurs as a a result of retrograde blood flow from a high pressure chamber to a low pressure chamber. Holosystolic murmurs are usually generated by backward regurgitant blood flow through atrioventricular valves.

This murmur occurs at the onset of S1 heart sound and goes on above A2. This murmur can be caused by the mitral regurgitation, tricuspid regurgitation or ventricular septal defect.

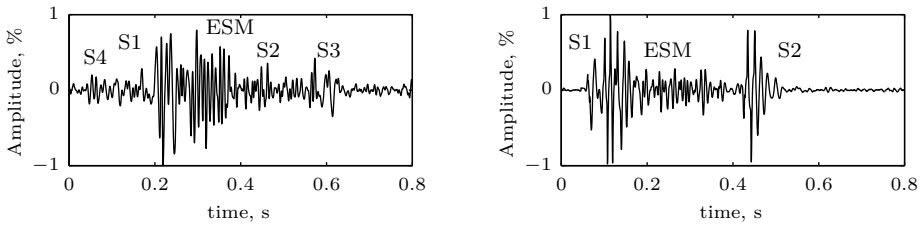


(a) Acute severe MR (b) MVP: standing after squatting

Figure I.25: Systolic murmurs: early systolic murmurs (ESM). (a): Acute severe mitral regurgitation (apex), (b) MVP: standing after squatting (apex) [1]

**Holosystolic murmurs** The holosystolic murmur occurring in mitral regurgitation is plateau–shaped. It is usually loudest than the S1 heart sound and is best heard at the apex with a noticeable radiation to the axilla. Moreover, a wide split of the S2 heart sound is observed. The left ventricular ejection is shortened and induces an early S2 heart sound. Moreover, a S3 gallop can be heard at the apex (Figure I.26).

If the holosystolic murmur is generated by a ruptured anterior chordae, then the radiation should be perceived at the mid–thoracic spine. This murmur is softer with Valsalva and inspiration.

The tricuspid regurgitation is also characterised by a plateau shaped holosystolic murmur. This holosystolic murmur is differentiated from that of the mitral insufficiency by the following features. It is best heard at the $4^{\text{th}}$–$5^{\text{th}}$ interspaces along the left sternal border with no radiation into the axilla and becomes louder with inspiration (Carvallo's sign).

The ventricular septal defect (VSD) causes a holosystolic murmur which is harsh than that of mitral or tricuspid regurgitation. This murmur is best heard at the $4^{\text{th}}$, $5^{\text{th}}$, and $6^{\text{th}}$ intercostal spaces to the left of the sternum. The murmur of the VSD has no radiation into the axilla (unlike MR) and does not increase with inspiration (unlike TR). These acoustic features differentiate the murmur of the VSD from that of mitral and tricuspid regurgitation as well. Moreover, the VSD is characterised by a fixed and occasionally wide split of S2 heart sound.

**Mid systolic murmurs** Systolic ejection murmurs, also known as midsystolic murmurs, are generated by blood inflow within the ventricle. Midsystolic murmurs occur after S1 heart sound and end before S2 heart sound. These murmurs are diamond shaped (crescendo–decrescendo or saw–like shape) and are acoustically harsh (Figure I.27(d)).

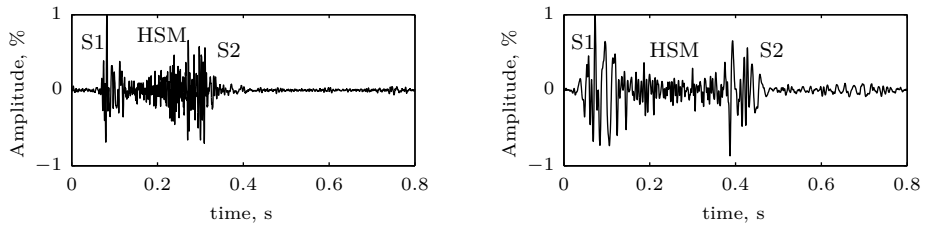


(a) HSM MR (b) HSM TR

Figure I.26: Systolic murmurs: Holosystolic murmurs (HSM). (a): MR from ruptured cordae tendinae (apex), (b) Tricuspid regurgitation with respiration (apex) [1]

Midsystolic murmurs occurs as a result of:

- A rising blood flow through aortic or pulmonary valves which can be caused by pregnancy, thyroid excess states, exercise, anaemia, or fever.
- Blood ejection into a dilated aorta which can be caused by arteriosclerosis or aneurysm.
- Blood ejection through thickened valve or calcified aorta due to aortic sclerosis. Aortic sclerosis can be differentiated from aortic stenosis by a normal carotid artery pulse.
- Blood ejection through a stenosed aortic or pulmonary valve.

Valvular aortic stenosis produces the classic mid–systolic ejection murmur. This murmur occurs as a result of turbulent blood flow through a stenosed aortic valve. The murmur can be heard at the $2^{\text{nd}}$ right intercostal space, $3^{\text{rd}}$ left intercostal space, and at the apex. Aortic stenosis is bound up with a tapered pulse pressure. Chronic pressure overloading on the left ventricle results in a sustained apical impulse characteristic of left ventricular hypertrophy. A more delayed aortic ejection causes a split S2 heart sound which can be narrow or paradoxical. This murmur is decreased during inspiration and sustained Valsalva.

A mid–systolic murmur can be generated under hypertrophic obstructive cardiomyopathy (IHSS). This murmur is caused by hypertrophy of the interventricular septum which obstructs the left ventricular outflow and thwarts the mitral leaflets during systole. Therefore, a systolic pressure gradient occurs and give rise to blood turbulence which leads to a mid–systolic murmur. The murmur is best auscultated along the left sternal border.

A mid–systolic can be generated by pulmonic stenosis due to the narrow pulmonic valve. This murmur is differentiated from that of the aortic stenosis by the following features;

- The pulmonic stenosis murmur is higher at the $2^{\text{nd}}$ and $3^{\text{rd}}$ left intercostal spaces and is of lower intensities than that of aortic stenosis.

- There is no radiation of the pulmonic stenosis murmur into carotid arteries.
- The pulmonic stenosis generates a left parasternal sustained impulse due to right ventricular hypertrophy.
- During inspiration, the intensity of the murmur follows the right heart venous return rising.

Brief Silent durations are observed between the murmur and S1 and S2 heart sounds. These gaps confirms that the murmur is mid–systolic rather than pansystolic.

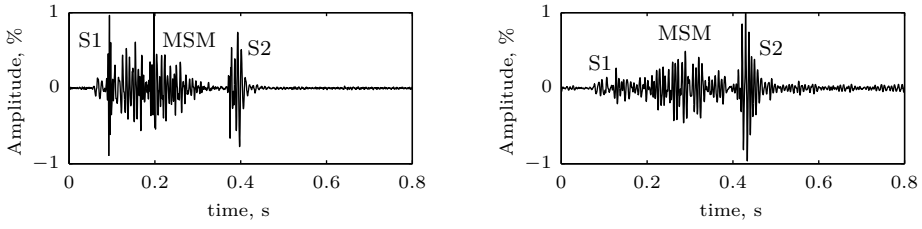


(a) MSM BAV




(b) MSM AS

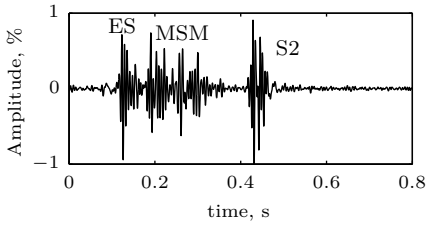


(c) MSM AR

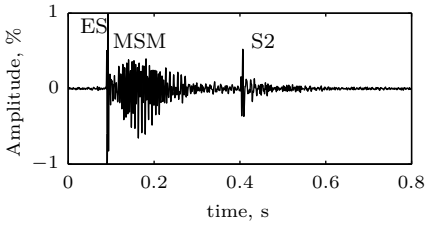


(d) MSM PS

Figure I.27: Systolic murmurs: Mid systolic murmurs (MSM). (a) Congenital aortic stenosis; bicuspid aortic valve ($2^{nd}$ right intercostal space, RIS), (b) Aortic stenosis; calcified aortic valve ($2^{nd}$ RIS), Aortic regurgitation ($2^{nd}$ RIS), (d) Moderate pulmonary valvular stenosis; Greatly dilated pulmonary artery (left infraclavicular) [1]

**Late systolic murmurs** Late systolic murmurs are observed under mitral and tricuspid valve prolapse. This kind of murmurs are usually associated with an early mid–systolic click. The murmur has a crescendo shape towards S2 heart sound (Figure I.28).

Transient late systolic murmurs are observed in patients with mitral or tricuspid prolapse, *i.e.* the occurrence of these murmurs is occasional.

### Diastolic murmurs

There are two types of diastolic murmurs; filling and regurgitant murmurs. Diastolic filling murmurs, known as rumbles, are generated by forward blood flow

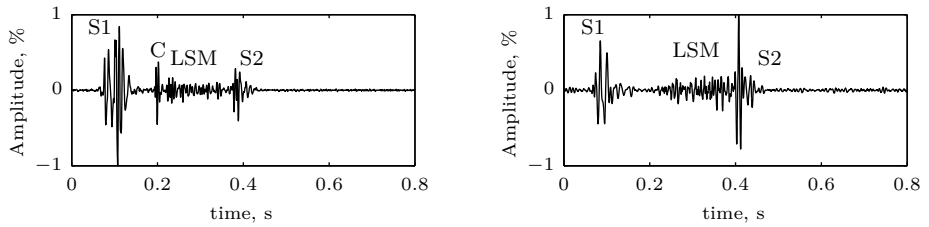


(a) LSM MVP (b) LSM MVP (apex)

Figure I.28: Systolic murmurs: Late systolic murmurs (LSM). (a): Mitral valve prolapse (Lower left sternal border), (b): MVP (apex) [1]

through incompetent atrioventricular valves. Diastolic regurgitant murmurs are due to retrograde blood flow through unobstructed semilunar valves.

Mid–diastolic and presystolic murmurs are due to stenosis of atrioventricular valves. These murmurs occur with an S3, also known as S3 rumbles, which are observed in mitral or tricuspid regurgitation. Austin–Flint murmur effects from the interaction between the aortic and the mitral valves during aortic regurgitation. This murmur starts in mid–diastole and may continue to presystole (Figures I.29&I.29).

**Early diastolic murmurs** Early diastolic murmurs begin right after S2 and fades before S1. This type of murmurs is associated with regurgitant blood flow through unobstructed semilunar valves. Therefore, the differential diagnosis is confined to aortic and pulmonic regurgitation.

**Aortic insufficiency** The diastolic regurgitant murmur can be generated from the left heart as a result of aortic regurgitation. The murmur occurs with A2, follows a decrescendo shape, and fades in late diastole phase. The murmur is high pitched and best heard at the $2^{\text{nd}}$ right intercostal space, $3^{\text{rd}}$ left intercostal space, and apex. The murmur is accentuated as peripheral vascular resistance increases, *e.g.* handgrip, squatting, and exercise.

The aortic insufficiency is characterised by a snapping S2 heart sound. Moreover, an S3 heart sound occurs as a result of rapid ventricular filling at a high volume. Two supplementary murmurs usually occur in aortic regurgitation. The first one is a midsystolic aortic ejection murmur that is generated by the rising blood volume ejected through the aortic valve. The second is a mid to late diastolic rumbling murmur (Austin–Flint) appearing at the apex. This murmur is low pitched and is caused by regurgitant blood flow occurring around mitral valve leaflets. The created pressure gradient partially closes the mitral valve. This is a functional mitral stenosis. The generated murmur reveals a severe aortic regurgitation.

**Pulmonic regurgitation** The murmur occurring in pulmonary regurgitation[22] is differentiated from that of the aortic regurgitation by its rising intensity during inspiration. Moreover, this murmur is not related to peripheral effects of the aortic regurgitation (wide pulse pressure, bounding pulses, large left ventricle, etc.).

**Mitral stenosis** The murmur generated by mitral stenosis is rumbling, low pitched, and best heard at the apex in the left lateral decubitus position. An opening snap sound begins the murmur right after S2. The murmur fades at the mid–diastole and rises towards S1. This acoustic crescendo effect, also known as the presystolic accentuation, is stressed by atrial contraction. An increased S1 is usually considered as a significant sign of mitral stenosis.

**Tricuspid stenosis** The murmur of tricuspid stenosis is distinguished from that of mitral stenosis since it is louder at the the $4^{\text{th}}$ intercostal space at the left sternal border and rises during inspiration.

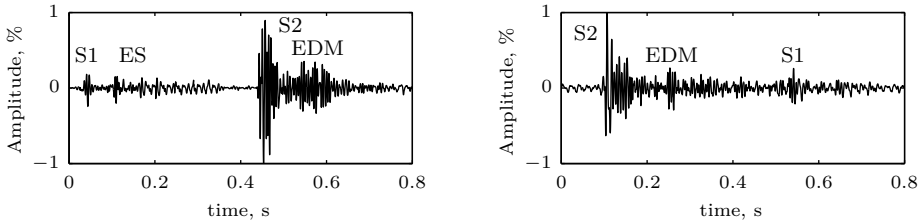


(a) EDM AR (b) EDM PR

Figure I.29: Diastolic murmurs: Early diastolic murmurs (EDM). (a): Acute severe aortic regurgitation, (b): Moderate pulmonic regurgitation; Eisenmenger ventricular septal defect (inspiration) [1]

**Mid–diastolic and presystolic murmurs** Mid–diastolic and presystolic murmurs are caused by turbulent blood flow through atrioventricular valves. The common example of the diastolic filling murmur is that of mitral stenosis (Figure I.30).

This diastolic murmur is rumbling and low pitched and is best heard a the apex in the left lateral decubitus position. A mid–diastolic murmur occurs right after S2. This murmur can merge with a late diastolic murmur. When an opening snap occurs after S2, then the murmur fades by mid–diastole.

### I.5.3 Valvular lesions

Cardiovascular pathologies effects morphological alterations of the phonocardiogram waveforms. Valvular anomalies are classified in two categories whether it results form a valve stenosis, insufficiency, or regurgitation.

[22]The murmur due to pulmonary regurgitation resulting from pulmonary hypertension is known as Graham Steel murmur.

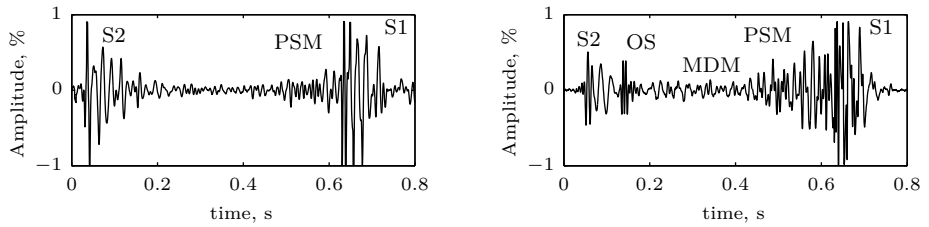


(a) TS (b) MD & PS murmurs

Figure I.30: Diastolic murmurs: Mid–diastolic (MD) & presystolic murmurs (PS). (a): Tricuspid stenosis (TS), (b): Moderate mitral stenosis [1]

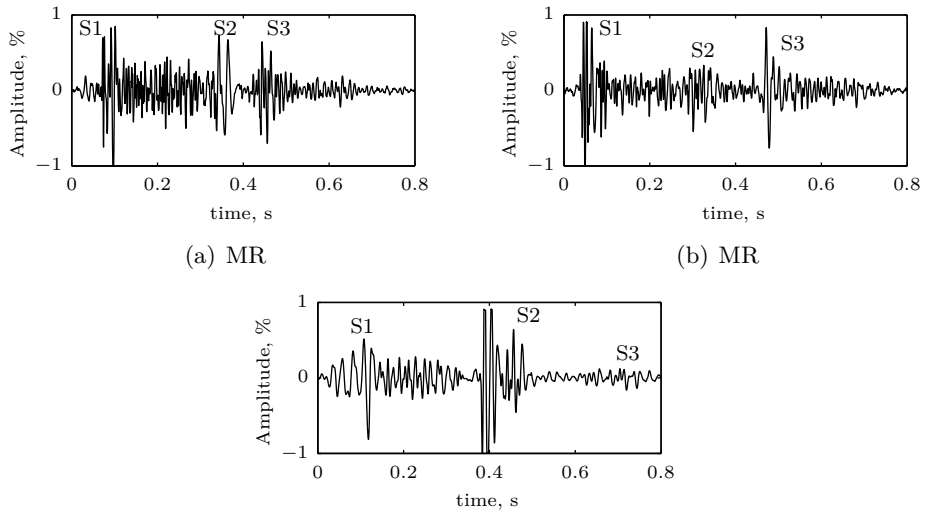


(a) MR (b) MR

(c) MR

Figure I.31: Diastolic murmurs: S3 rumbles. (a): Chronic severe mitral regurgitation, (b): Tricuspid regurgitation, (c): Atrial septal defect [1]

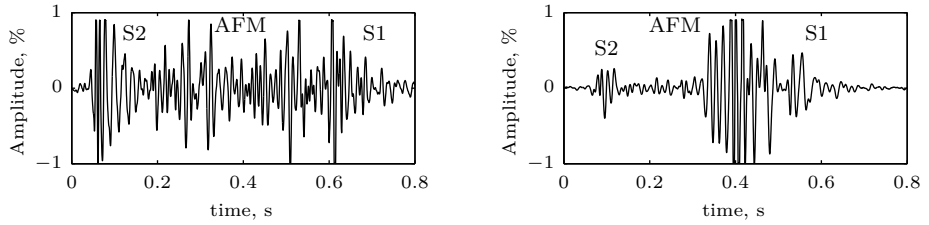


(a) Chronic AR (b) Acute severe AR

Figure I.32: Diastolic murmurs: Austin Flint murmurs. (a): Chronic aortic regurgitation, (b): Acute severe aortic regurgitation [1]

These valvular anomalies may result from rheumatic fever or tissue degeneration due to ageing. The most frequent valvular disease are mitral stenosis (MS), mitral

insufficiency (MI), aortic stenosis (AS), and aortic insufficiency (AI). More seldom observed are pulmonic stenosis (PS) due to congenital origins and Coarctation of the aorta (COA).

### Mitral stenosis

Stenosis of the mitral orifice disturbs the normal filling of the left ventricle. Therefore, pressures increase upstream of the left atrium and pulmonary capillaries. This alters the normal structure of the corresponding phonocardiographic signal. The opening snap (OS) of the mitral valve can be recorded in early diastole just after S2 as shown in Figure I.33. No doubt, the opening snap of the mitral valve is one important pathological sign of mitral stenosis; it lasts between 30 to 130 ms. For this pathology, the pulmonary component of the second heart sound (S2), is usually accentuated.

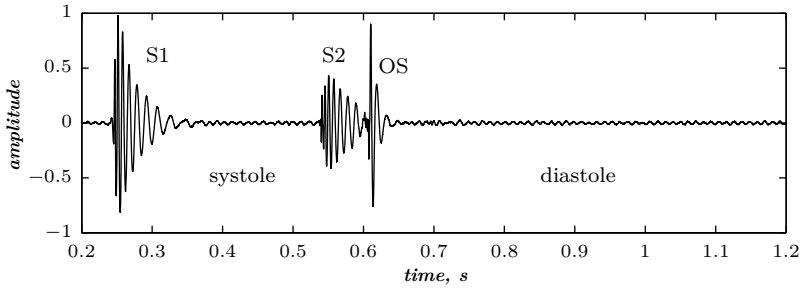


Figure I.33: Mitral Stenosis: Opening snap (OS) [24].

When the stenosis is more severe, a diastolic murmur can occur after the opening snap of the mitral valve, it is composed of two elementary components; The early diastolic murmur (decrescendo type) appearing at the rapid ventricular filling and the late diastolic murmur (crescendo type) which occurs at the atrial contraction as shown in Figure I.34. The intensity of these murmurs determines the severity of the stenosis.

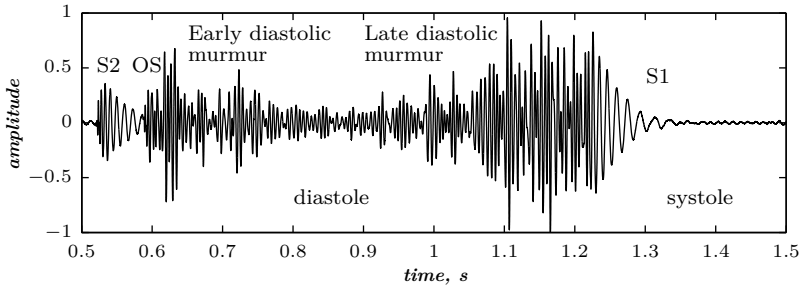


Figure I.34: Mitral Stenosis: Opening snap + Diastolic murmur [24].

These diastolic murmurs are due to blood flowing from the left atrium into the left ventricle through the restricted mitral orifice. The diastolic murmur is due

to the forceful ventricular filling through the stenosed mitral orifice. Its intensity depends on the filling velocity, which reaches its maximum at the end of the diastole phase. This murmur is distinguishable from that of aortic insufficiency by taking a time delay after S2 to appear. This lateness is due to the ventricular isovolumetric relaxation between the aortic valve closure and the beginning of mitral valve opening. It usually lasts more than 100 ms.

A systolic murmur can occur as shown in Figure I.35. It is a functional mitral regurgitation murmur due to the increasing ventricular ejection volume.

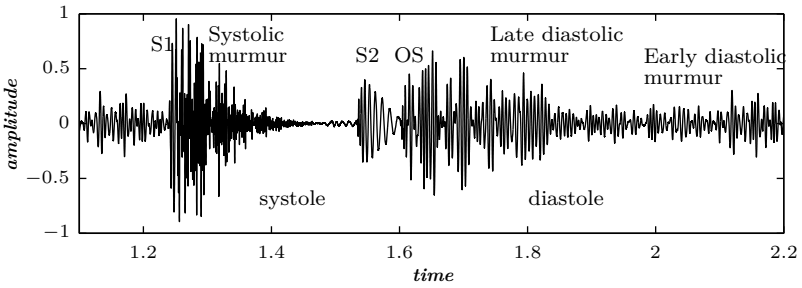


Figure I.35: Mitral Stenosis: Opening snap + Diastolic murmur + systolic murmur [24].

### Mitral insufficiency

Closure of the mitral valve depends on interaction between papillary muscles, ropes, and the valvular ring. The malfunction of one or several elements of this mitral system influences normal closure of the mitral valve. This produces blood ebb from the ventricle to the atrium in the left heart during systole phase.

Mitral insufficiency is mainly characterised by the backward ventricular blood flow. This will overload the left ventricle, which must pump much more blood, but unfortunately without the efficiency of the entire blood volume. Therefore, the left ventricle will suffer from dilation and hypertrophy. In addition, blood ebb coming from the left ventricle dilates the left atrium passively. During mitral insufficiency, regulation mechanisms of the pulmonary circulation, which aims to have suitable left ventricular filling, are completely absent. Therefore, there is no pressure increasing in the pulmonary circulation. This makes the main symptom of this pathology being the tiredness of the patient due to the lack of a sufficient peripheral vascularisation.

The incontinence of mitral valve elicits blood regurgitation from the left ventricle to the left atrium during systole phase. This will generate a rectangular-shaped decrescendo systolic murmur occurring just after the first heart sound as illustrated in Figure I.36. The systolic murmur does not last to the beginning of the second heart sound except for severe insufficiency. In more severe cases, this systolic murmur loses its decrescendo shape.

The valvular vibratory capabilities are deteriorated under valvular degeneration

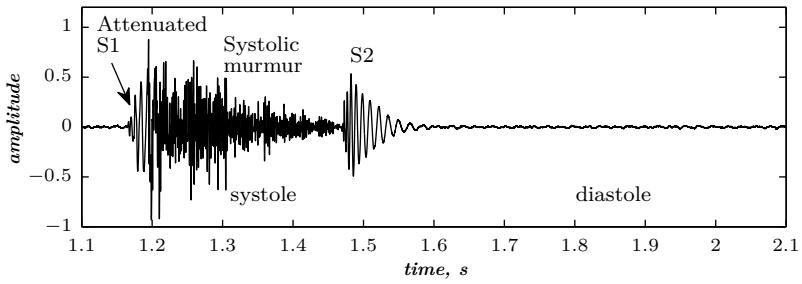


Figure I.36: Mitral Insufficiency: S1 attenuated + Systolic murmur [24].

and calcification. The attenuation of the first heart sound is due to the weak electromyocardial activation of the insufficient valve. Because of ventricular blood ebb, the left atrium is full at the end of diastole, which can generate an accentuated third heart sound (S3) as shown in Figure I.37.

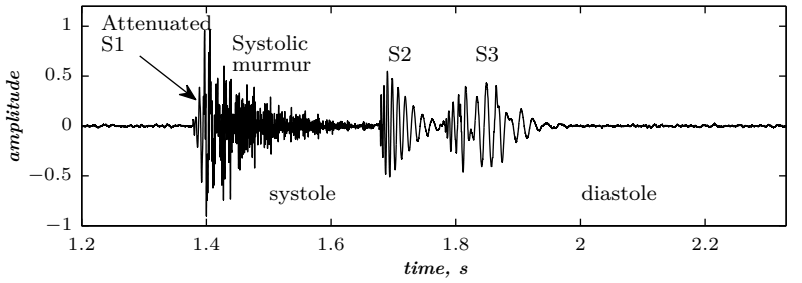


Figure I.37: Mitral Insufficiency: S1 attenuated + Systolic murmur + S3 [24].

Mitral insufficiency cannot be easily recognised when the third heart sound is lacking, especially in old patients. The Phonocardiographic signal can give more information about the beginning and the end of the systolic murmur. The decrescendo slope and the duration of the murmur can be informative about the pathology severity.

Sometimes, a doubled second heart sound (S2) can be recorded. This is due to decreasing of the ventricular ejection volume. The third heart sound is also clear. Recording of a fourth heart sound (S4) indicates severe mitral insufficiency.

When regurgitation volume and diastolic filling velocity are high, the third heart sound is followed by a functional diastolic murmur characterised by a low frequency content as shown in Figure I.38.

### Aortic stenosis

Stenosis of the aortic valve leads to disturbances in blood ejection from the left ventricle to aorta during the systole phase. Hence, aortic blood flow decreases and generates a systolic diamond–shaped ejection murmur as shown in Figure I.39.

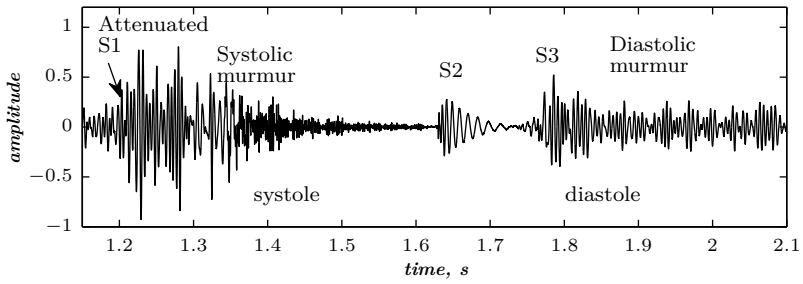


Figure I.38: Mitral Insufficiency: S1 attenuated + Systolic murmur + S3 + diastolic murmur [24].

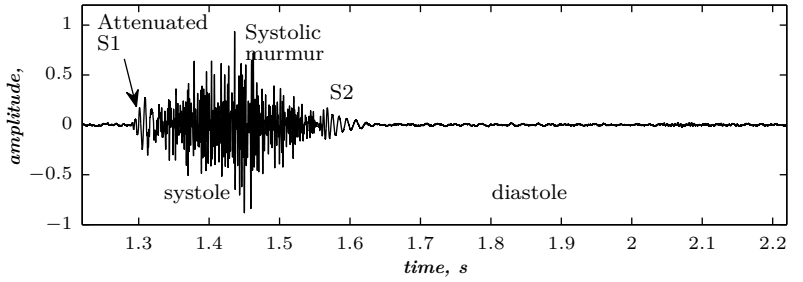


Figure I.39: Aortic Stenosis; S1 and S2 attenuated + Systolic murmur [24].

Stenosis of the ejection duct can yield a hypertrophy of the left ventricle, the dilation is often weak since the ejection volume do not considerably increase, and it is generally absent as long as the left ventricle is compensated.

The systolic murmur of aortic stenosis, occurring at the ejection phase, is distinguishable from mitral insufficiency murmur since it is generated after a hiatus from the first heart sound. It reaches a maximum, which depends on the severity of the stenosis and the ejection volume quantity. This maximum is localised at the middle of the systole, and is slightly attenuated and moved to the last third of the systole phase for severe stenosis. This is due to decreasing of the gradient between ventricular and atrial pressures at the end of systole.

Generally, for aortic stenosis cases, the first and second heart sounds are attenuated. In severe cases, the second heart sound (S2) is doubled and inversed because of the stretching of left ventricular systole. The weakness of the first heart sound is due to the forceful hypertrophy of the left ventricle. The increasing of left heart volume decreases considerably the cardiac rhythm. The increasing of left ventricular pressure will make the mitral valve thicker which limits its vibration capabilities.

As illustrated in Figure I.40, an aortic ejectional click is an indication of the aortic stenosis severity.

In the case of left ventricular hypertrophy, the atrial systole is carried out under high pressure, which yields accentuated atrial sounds (Figure I.41).

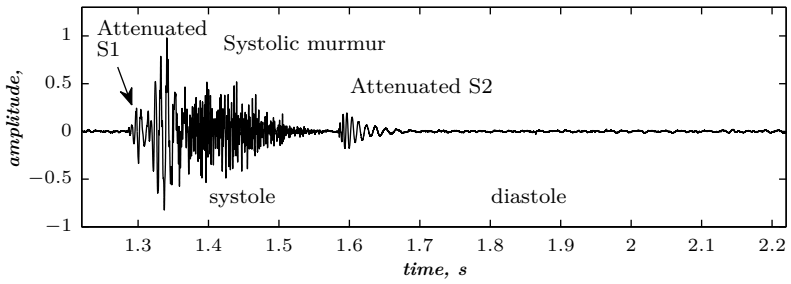


Figure I.40: Aortic Stenosis; S1 and S2 attenuated + Systolic murmur + aortic dilation murmur [24].

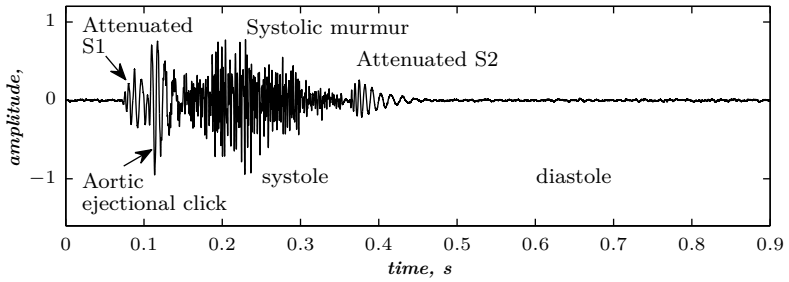


Figure I.41: Aortic Stenosis; S1 and S2 attenuated + Systolic murmur + aortic dilation murmur + atrial murmur [24].

A diamond–shaped rough murmur appears at the end of ventricular ejection. Left ventricular hypertrophy provides a high–pressure ventricular filling from the left atrium. Therefore, a diastolic murmur can be recorded (Figure I.42).

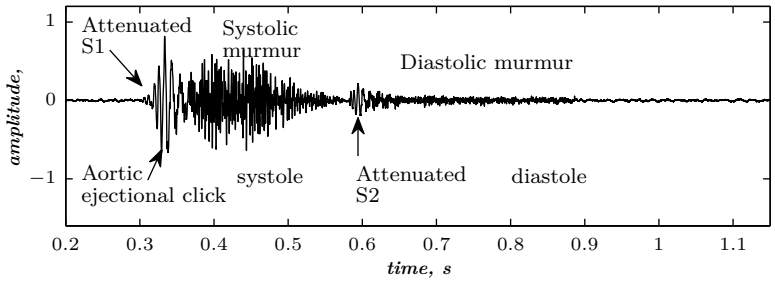


Figure I.42: Aortic Stenosis; S1 and S2 attenuated + Systolic murmur + aortic dilation murmur + atrial murmur + diastolic murmur [24].

### Aortic insufficiency

During diastole, blood circulates through the insufficient sigmoid valves, and hence a diastolic decrescendo murmur occurs (Figure I.43). Insufficiency of the aortic valve

yields blood regurgitation in the left ventricle during diastole phase. The ejection volume increases at every systole period to have the same amount of blood ejected to the periphery. The continuous increasing of ejection blood volume will produce a hypertrophy and a dilation of the left ventricle. The left atrium and the right ventricle are not modified as long as the heart still compensated.

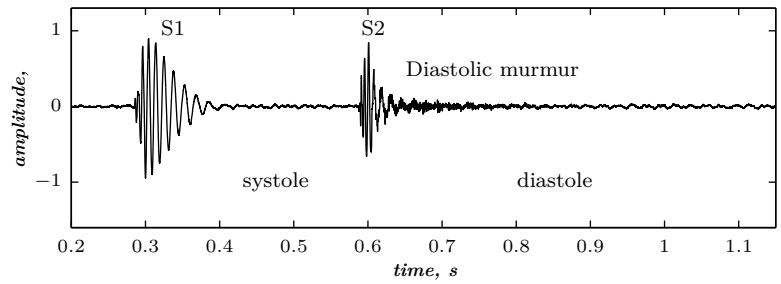


Figure I.43: Aortic Insufficiency: Diastolic murmur [24].

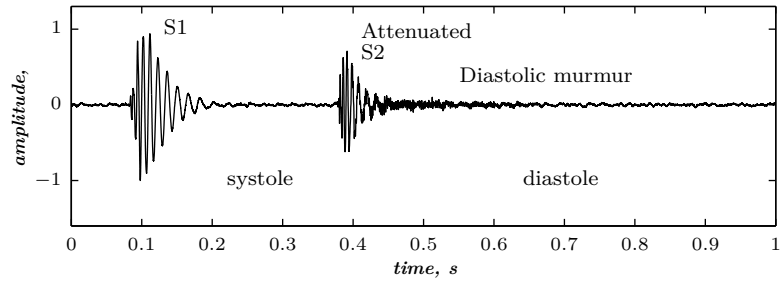


Figure I.44: Aortic Insufficiency; Diastolic murmur, attenuated S2 [24].

Due to their similarity, murmurs of aortic insufficiency and mitral stenosis can be usually mixed up. Therefore, Physicians could distinguish the acute aspect of aortic insufficiency from the deep rumble aspect of mitral stenosis. Since the pressure difference between the root of the aorta and left ventricle, in its relaxation period, is very high at the onset of diastole, then the murmur begins just after the second heart sound.

When the insufficiency is more severe, blood regurgitation provides an accentuated diastolic stretched murmur (Figure I.45).

Usually, a systolic murmur can be recorded (Figure I.46). It can be originated by a coexistent stenosis. However, this murmur can be recorded even for a pure aortic insufficiency. It is a functional murmur, it always occurs when the ejection volume is increased. This murmur can disappear when the aortic insufficiency is moderate.

A diastolic murmur, which can have the same features of mitral stenosis murmur, can seldom be recorded. This murmur does not give any indication of the existence of a mitral stenosis. It can be a functional murmur, which the origin can be in relation with blood coming from the aorta. Hence, the generated flow affects the

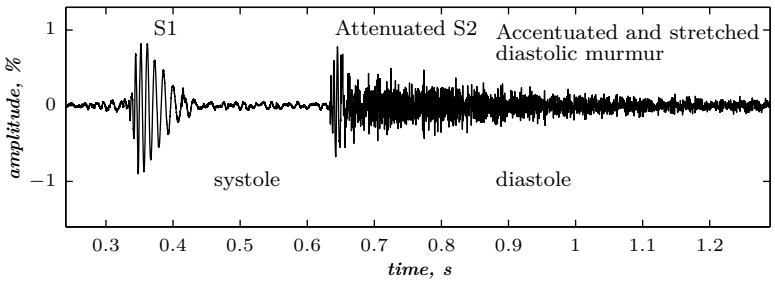


Figure I.45: Aortic Insufficiency; diastolic stretched murmur, attenuated S2 [24].

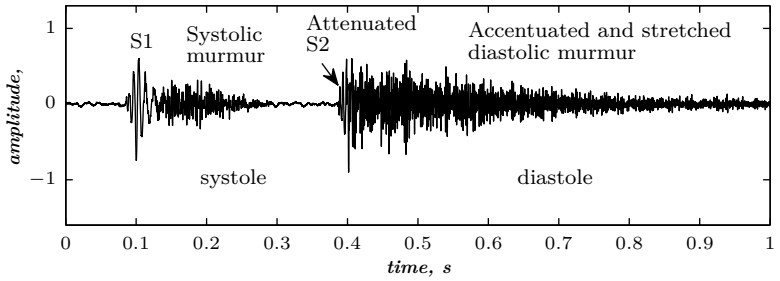


Figure I.46: Aortic Insufficiency; diastolic stretched murmur, attenuated S2 + systolic murmur [24].

mitral valve and cause a functional stenosis. This murmur is also called Austin–Flint murmur (Figure I.47).

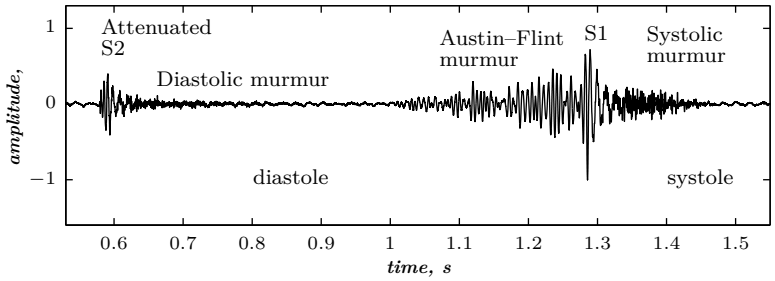


Figure I.47: Aortic Insufficiency; diastolic stretched murmur, attenuated S2 + systolic murmur + Austin–Flint murmur [24].

### Pulmonary stenosis (congenital pathology)

This pathology is characterised by a systolic ejection murmur. It is usually due to congenital origins. Sometimes, rheumatic causes can generate this anomaly. During decompensation of the right heart, systolic shudders occur and generate a murmur.

| | S1 | S2 | Additional sounds | Murmurs |
|---|---|---|---|---|
| Mitral stenosis | Bursted | Sometimes accentuated P2 | OS (30 up to 120 ms after the onset of S2) | Systolic and diastolic murmurs |
| Mitral insufficiency | More attenuated when the insufficiency is severe | unattenuated with accentuated P2 | S3 usually recorded | Systolic murmur |
| Aortic stenosis | Usually attenuated | Usually attenuated | S4 usually recorded, ejection click | Intense systolic diamond–shaped murmur |
| Aortic insufficiency | Unchanged | Attenuation in grave insufficiency | Non–typical | Systolic and diastolic murmurs, Austin–Flint murmur |
| Pulmonic stenosis | Unchanged | Doubled | Pulmonic ejectional click | Diamond–shaped systolic murmur |

Table I.2: Phonocardiographic content of common valvular pathologies.

Intensity of the first heart sound is normal. The second heart sound is doubled because of the stretching of the right ventricular systole, and their aortic and pulmonic components are clearly distinguishable. The pulmonic component is usually attenuated, but sometimes is not audible for severe cases. The first heart sound is followed by a pulmonic ejection click, which becomes weaker in inspiration and appears early in expiration, followed by an intense diamond–shaped ejectional murmur as shown in Figure I.48. Its maximum is delayed as long as pressure gradient is higher. The fourth heart sound, which is interrelated with the raise of the diastolic right ventricular pressure, can be recorded.

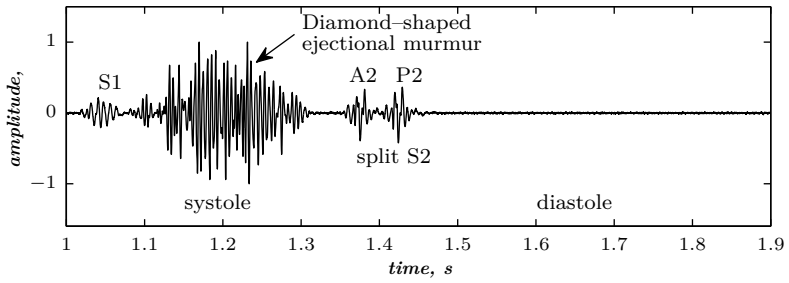


Figure I.48: Pulmonic stenosis: Harsh systolic ejection murmur [24]

The systolic murmur can reach the second heart sound because of the delay in the right ventricular ejection, and can sometimes overtake the aortic component. This makes it more distinguishable from the aortic stenosis murmur. Table 1 summarizes some acoustical features of these pathologies.

## I.6 Conclusion

In conclusion, digital phonocardiography is useful as a cardiac diagnosis technique. However, the issue encountered in establishing a strong and widely recognised theory for heart sounds genesis is probably due to the fact that both the valvular and cardiohemic theories may be partly valid. Thus, genesis and propagation of heart sounds through the chest wall is a very complex phenomenon that cannot be described by a simplistic theory based only on vibration of either heart valves or the entire heart as one whole. Nevertheless, the recorded heart sounds and murmurs known as thoracic phonocardiogram includes both valvular, heart cavities and blood flow vibrations. The multidegree of freedom theory validates both the cardiohemic and valvular theories.

# Chapter II

# Time–frequency analysis methods

This chapter presents the theoretical background of time–frequency methods used to analyse phonocardiographic data. Localising information in both time and frequency domains is the main purpose of time–frequency analysis.

Fourier theory provides frequency representation of sinusoids but still limited when dealing with non–stationary signals as phonocardiographic signals. Therefore, time–frequency representations computed by Fourier–based methods such as the spectrogram are of restricted performance regarding adequate time–frequency representation because of their unavoidable time and frequency resolution trade–off. Indeed, classical methods are useless in investigating information within biomedical signals which is usually concealed within their non–stationary content.

Adapted methods to phonocardiographic signals analysis are presented and studied with their respective properties. Thus, time–frequency methods are categorised into two main classes; namely energy distributions and atomic decomposition methods. Energy distributions are studied through the Wigner–Ville distribution (WVD) which is the basic method of the overall Cohen's class. In addition to the desired properties of the WVD–based methods, its smoothed versions; namely the Pseudo–WVD (PWVD), smoothed–PWVD (SPWVD), as well as the Reassigned–SPWVD (RSPWVD) as additional improvements are also presented. The atomic decomposition class is studied through the Continuous Wavelet Transform (CWT), the Discrete Wavelet Transform (DWT), and Wavelet packets (WP). The squared modulus of the CWT yields an estimation of the signal's energy within the time–scale plane also known as the scalogram.

Practical illustrations of each method are presented to show its benefits and setbacks as a preliminary analysis step. Discussion of the obtained results helps to select the appropriate analysis method to be applied on phonocardiographic signals.

This chapter is mainly partitioned into two sections. Firstly, sectionII.1, entitled "Energy distributions", gathers the theoretical background of energy distributions as well as their practical benefits and drawbacks. Secondly, section II.2, entitled

"Atomic decompositions", presents the theoretical background of the Continuous wavelet transform, discrete wavelet transform, and wavelet packets.

## II.1 Energy distributions

The aim of energy distributions is to distribute the energy of the analysed signal both in time and frequency domains. This distribution leads to a time–frequency representation also called time–frequency distribution which refers to energy distribution within the time–frequency plane.

**Energy** The energy $E_x$ of a given signal $x(t)$ is defined in the time domain by (II.1),

$$E_x = \int_{-\infty}^{+\infty} |x(t)|^2 \, \mathrm{d}t \tag{II.1}$$

or alternatively in the frequency domain by (II.2),

$$E_x = \int_{-\infty}^{+\infty} |X(f)|^2 \, \mathrm{d}f \tag{II.2}$$

where $X(f)$ represents the Fourier transform of the signal $x(t)$.

**Energy density** Since frequency is related to time, and vice–versa, then it is obvious to search for a combined joint time–frequency formulation of the energy $E_x$. Therefore, a logic formulation occurs as given in (II.3),

$$E_x = \iint_{-\infty}^{+\infty} \rho_x(t, f) \, \mathrm{d}t \, \mathrm{d}f \tag{II.3}$$

Therefore, the term $\rho_x(t, f)$ represents the energy density of the analysed signal $x(t)$ over the time–frequency plane. Thus, in order to get a correct representation of the energy $E_x$ both in time and frequency within the time–frequency plane, it is necessary that the energy density satisfies the *marginals properties* both in time and frequency domains as given in (II.4) and (II.5),

$$\int_{-\infty}^{+\infty} \rho_x(t, f) \, \mathrm{d}f = |x(t)|^2 \tag{II.4}$$

$$\int_{-\infty}^{+\infty} \rho_x(t, f) \, \mathrm{d}t = |X(f)|^2 \tag{II.5}$$

The energy synthesis described in (II.4) and (II.5) ensures recovery of the energy of the analysed signal $x(t)$ both in time and frequency domains. This suitable property is recommended to select among the various time–frequency methods which one

could effectively represent information within phonocardiographic signals. Moreover, this information can only be viewed through the inevitable uncertainty principle over the time–frequency plane.

**Uncertainty principle** According to the uncertainty principle[1], a signal can be localised both in time and frequency domains with an inevitable spread. Thus, mean values of duration and bandwidth, as well as mean time and frequency for each spectral component are defined.

The *mean time* $t_m$ of the signal $x(t)$ is given by (II.6),

$$t_m = \frac{1}{E_x} \int_{-\infty}^{+\infty} t|x(t)|^2 dt, \tag{II.6}$$

and its *duration* $T$ is given by (II.7),

$$T = \frac{4\pi}{E_x} \int_{-\infty}^{+\infty} (t - t_m)|x(t)|^2 dt \tag{II.7}$$

Its *mean frequency* $f_m$ is given by (II.8),

$$f_m = \frac{1}{E_x} \int_{-\infty}^{+\infty} f|X(f)|^2 df, \tag{II.8}$$

and its *bandwidth* $B$ is given by (II.9),

$$B = \frac{4\pi}{E_x} \int_{-\infty}^{+\infty} (f - f_m)|X(f)|^2 df \tag{II.9}$$

The product $BT$ has a minimum which is uniquely reached for Gaussian functions as written in (II.10),

$$BT \geq 1 \tag{II.10}$$

Properties (II.1)[2], (II.2)[3] and (II.3)[4] are suitable for the time–frequency energy density $\rho_x(t, f)$. Additional constraints are imposed to time–frequency energy distributions to yield a correct representation. Indeed, the Cohen's class [57] gathers time–frequency distributions with desirable properties, *e.g.* time and frequency shifts which terms the Cohen's class as covariant or shift–invariant class.

[1] also known as Heisenberg principle.
[2] Energy of the signal $x(t)$ in the time domain (see page 60).
[3] Energy of the signal $x(t)$ in the frequency domain (see page 60).
[4] Energy density of the signal $x(t)$ in the time–frequency plane (see page 60).

### II.1.1 Wigner–Ville Distribution (WVD)

The Wigner–Ville distribution (WVD) [58] is the basic energy distribution of the Cohen's class, and is defined by (II.11),

$$W_x(t,\nu) = \int_{-\infty}^{+\infty} x\left(t+\frac{\tau}{2}\right) x^*\left(t-\frac{\tau}{2}\right) e^{-j2\pi\nu\tau}\mathrm{d}\tau \tag{II.11}$$

where $x(.)$ refers to the analysed signal, and the asterisk denotes the complex conjugate.

or alternatively by (II.12)

$$W_x(t,\nu) = \int_{-\infty}^{+\infty} X\left(\nu+\frac{\theta}{2}\right) X^*\left(\nu-\frac{\theta}{2}\right) e^{j2\pi\theta t}\mathrm{d}\theta \tag{II.12}$$

**Properties - WVD** The WVD combines the time and frequency representations with some required properties to adequately represent a given signal $x(t)$ in the time–frequency plane [58]. The WVD has some nice properties which are summarised as follows.

1. The WVD is an element of the Cohen's class with a weighting function $g$ such that $g(\nu,\tau) = 1$.
2. *Realness:* The WVD is of real values over the time–frequency plane which makes it suitable for representing the energy of the analysed signal.
3. *Time and frequency marginals*: According to (II.4) and (II.5), and as shown in (II.13), the integration of the time–frequency distribution over the time domain yields the spectral density of the signal. Moreover, and as stated in (II.14), the integration of the time–frequency distribution over the frequency domain yields the instantaneous power of the analysed signal $x(t)$, as follows;

$$\int W_x(t,f)\ \mathrm{d}t = |X(f)|^2 \tag{II.13}$$

$$\int W_x(t,f)\ \mathrm{d}f = |x(t)|^2 \tag{II.14}$$

   where $X(f)$ denotes the Fourier transform of the signal $x(t)$, and $W_x(t,f)$ represents its WVD.
4. *Global energy conservation*: Integration of the WVD over the time–frequency plane yields the global energy $E_x$ of the analysed signal as follows;

$$\iint W_x(t,f)\ \mathrm{d}t\ \mathrm{d}f = E_x \tag{II.15}$$

5. *Instantaneous frequency (IF)*: the first moment of the WVD with respect to frequency of the analytic signal yields the IF as follows;

6. *Time delay (TD)*: the first moment of the WVD with respect to time of the analytic signal yields the TD as follows;

$$\frac{\int t W_x(t,f)\mathrm{d}t}{\int W_x(t,f)\mathrm{d}t} = -\frac{1}{2\pi}\frac{\mathrm{d}}{\mathrm{d}f}\left[\arg X(f)\right] \tag{II.16}$$

7. *Time and frequency support conservation*: The WVD is limited to time–frequency support defined by the duration and bandwidth of the analysed signal $x(t)$.

8. *Convolution invariance*: The WVD of the time–convolution of two signals $x_1(t)$ and $x_2(t)$, yields the time–convolution of their respective WVDs $W_{x_1}(t,f)$ and $W_{x_2}(t,f)$ as in (II.17);

$$\begin{aligned} x_3(t) &= x_1(t) \underset{t}{*} x_2(t) \\ \Rightarrow W_{x_3}(t,f) &= W_{x_1}(t,f) \underset{t}{*} W_{x_2}(t,f) \end{aligned} \tag{II.17}$$

9. *Modulation invariance*: The WVD of the frequency–convolution of two signals $x_1(t)$ and $x_2(t)$ yields the frequency–convolution of their respective WVDs $W_{x_1}(t,f)$ and $W_{x_2}(t,f)$ as in (II.18);

$$\begin{aligned} x_3(t) &= x_1(t) \cdot x_2(t) \\ \Rightarrow W_{x_3}(t,f) &= W_{x_1}(t,f) \underset{f}{*} W_{x_2}(t,f) \end{aligned} \tag{II.18}$$

10. *Unitarity (Moyal's formula)*: The energy calculated in the time domain is conserved in the time–frequency domain through WVDs of the elementary components $x(t)$ and $y(t)$ of a given signal, as in (II.19);

$$\left|\int_{-\infty}^{+\infty} x(t)\, y^*(t)\, \mathrm{d}t\right|^2 = \iint_{-\infty}^{+\infty} W_x(t,\nu)\; W_y^*(t,\nu)\, \mathrm{d}t\, \mathrm{d}\nu \tag{II.19}$$

**Interferences - WVD** The WVD is time and frequency invariant. Furthermore, a range of peaks of the IF and TD of the analysed signal are directly readable on the WVD [59, 60]. The WVD covers the spectral bandwidth of the analysed signal. Moreover, fluctuations of the maximum frequency of the analysed signal is well represented over the time domain by the WVD [61].

The analytic form of the analysed signal is necessary to avoid interference between positive and negative frequency components. However, cross–terms within the WVD

are unavoidable between components of the analysed signal. For a multicomponent signal $x(t) = x_1(t) + x_2(t)$, the WVD can be written as in (II.20);

$$W_x(t,\nu) = W_{x_1}(t,\nu) + W_{x_2}(t,\nu) + 2\Re W_{x_1 x_2}(t,\nu) \tag{II.20}$$

where $W_{x_1}$ and $W_{x_2}$ are auto–terms, also know as signal–terms, are the WVDs of $x_1(t)$ and $x_2(t)$ which are assumed to be analytic as well as $x(t)$. Whereas the term $W_{x_1 \cdot x_2}$ represents cross–terms, also known as outer–artefacts, which appear midway between $W_{x_1}$ and $W_{x_2}$ within the time–frequency plane. Therefore, the WVD of $x(t)$ is formed by the WVDs of its constituents and cross–terms which represents their cross–Wigner–Ville distribution (XWVD). Unfortunately, the obtained time–frequency representation becomes unreadable for multicomponent signals.

**Interferences (WVD) – practical illustration** To clarify the interference mechanism induced by the bilinear structure of the WVD, a signal of 256 samples formed by 4 gaussian atoms is synthesised and then analysed by the WVD, as illustrated in Figure II.1. Moreover, the analytic form of the synthesised signal is used instead of the original signal in order to reduce interferences between the negative and positive frequencies.

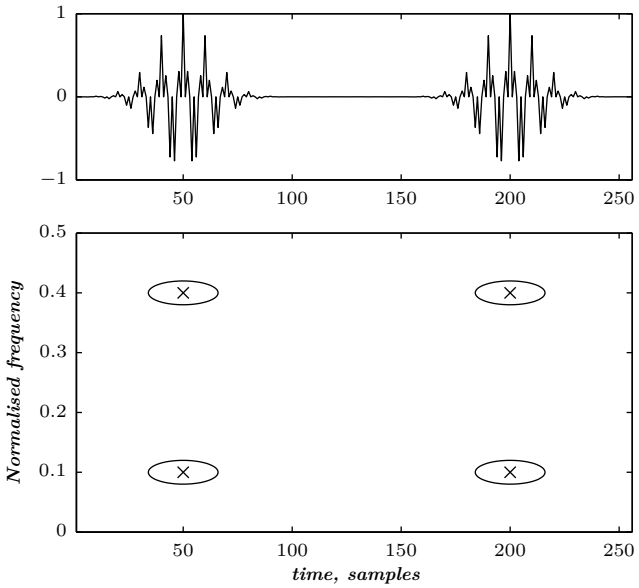


Figure II.1: Synthesised signal: four gaussian atoms (256 samples): (n,f) = (50,0.1), (50,0.4), (200,0.1), (200,0.4), where $n$ and $f$ denotes the time index and normalised frequency respectively.

Obviously, six cross–terms should occur between auto–terms shown in Figure II.1. It should be noticed that two cross–terms between the two diagonally opposite components are superimposed. Each interference occurs midway between each opposite

atoms and the three other atoms. To clarify the mechanism of these spurious interfering terms, the analytic form of the signal of Figure II.1 is analysed by the WVD, and the obtained time–frequency distribution is represented in Figure II.2.

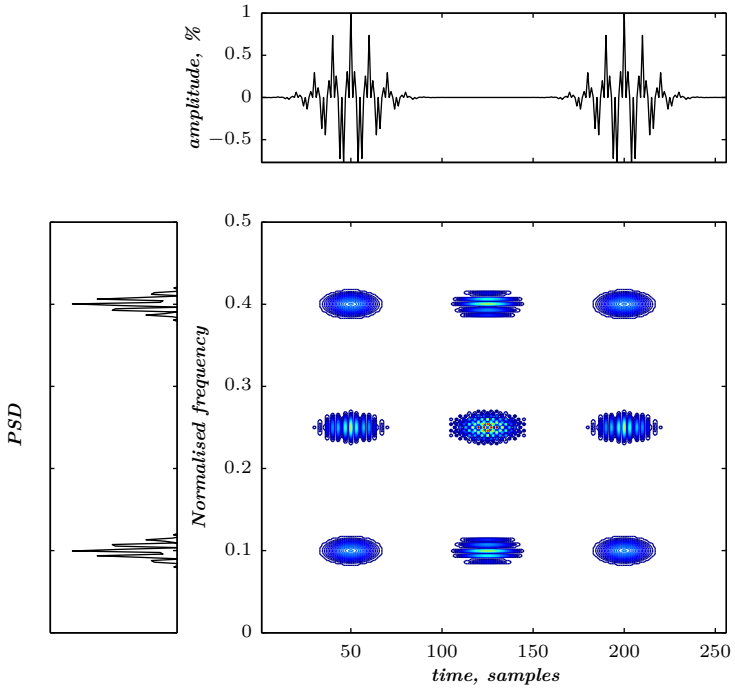


Figure II.2: WVD of the analytic form of the four gaussian atoms' signal. The top and left panels illustrates the analysed signal (Figure II.1) and its periodogram–PSD respectively.

Auto–terms of the gaussian atoms are recognised within the time–frequency plane as components localised at the intersection between their time and frequency supports as illustrated in top and left panels of Figure II.3.

The use of analytic signal is helpful to avoid interference between positive and negative frequencies. Indeed, Figure II.3 illustrates the WVD of the original synthesised signal of Figure II.1. In comparison to WVD depicted in Figure II.2, the obtained distribution is blurred with additional cross–terms between positive and negative frequencies within the time–frequency plane. These cross–terms considerably affect the readability of the computed distribution and confirms the usefulness of the analytic form of the analysed signal instead of the signal itself.

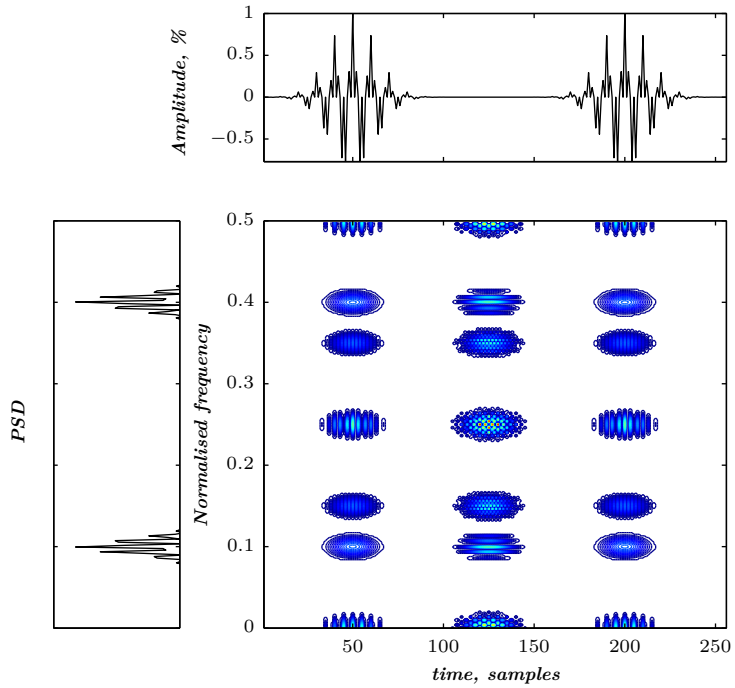


Figure II.3: WVD of the four gaussian atoms' signal. The top and left panels illustrates the analysed signal (Figure II.1) and its periodogram–PSD respectively.

**Analytic signal** The time–domain sampling of the WVD should be handled with care. The WVD defined in (II.11) can be written[5] by (II.21),

$$W_x(t,f) = 2\int_{-\infty}^{+\infty} x(t+\tau)\, x^*(t-\tau)\, e^{-j4\pi f\tau} \mathrm{d}\tau \tag{II.21}$$

Sampling the time variable in the WVD expression in (II.21) yields to a discrete–time continuous–frequency expression, as in (II.22),

$$W_x[n,f] = 2T_s \sum_k x[n+k]\, x^*[n-k] e^{-j4\pi fk} \tag{II.22}$$

where $T_s$ refers to the sampling period of the signal $x(t)$ such that the discrete signal is written by $x[n] = x(n\,T_s)$, where $n$ refers to the discrete time index.

The expression (II.22) is periodic in the frequency domain at $\dfrac{1}{2\,T_s}$. If the signal is sampled at the Nyquist rate[6], its discrete WVD is aliased despite its correct spectral representation through Fourier theory. Two solutions occurs regarding the signal,

[5] after a change of variable $\dfrac{\tau}{2} \to \tau$ in (II.11) in pp.62.

[6] In Fourier theory, spectral aliasing can be avoided by sampling the signal at least at twice its bandwidth which defines the Nyquist rate.

applying a dyadic upsampling or using its analytic form. The bandwidth of the analytic signal is half that of the original one. Moreover, this halved bandwidth considerably reduces the interferences within the time–frequency plane. Therefore, the analytic signal allows unambiguous extraction of the phase and the amplitude of a signal, and therefore allows to define the instantaneous frequency.

The analytic signal of $x(t)$ is given by (II.23),

$$x_a(t) = x(t) + j\,\mathrm{HT}\{x(t)\} \tag{II.23}$$

where HT denotes the Hilbert transform.

The analytic signal can also be defined in the frequency domain by (II.24),

$$X_a(f) = \begin{cases} 0 & \text{if} \quad f < 0 \\ X(0) & \text{if} \quad f = 0 \\ 2X(f) & \text{if} \quad f > 0 \end{cases} \tag{II.24}$$

where $X(f)$ refers to the Fourier transform of $x_a(t)$, the analytic signal of $x(t)$. The spectrum of $x(t)$ is then zero for the negative frequencies.

**Analytic signal – practical illustration** As illustrated in Figure II.4, a signal formed by 2 gaussian atoms is considered to show the usefulness of the analytic form of a given signal when calculating its WVD.

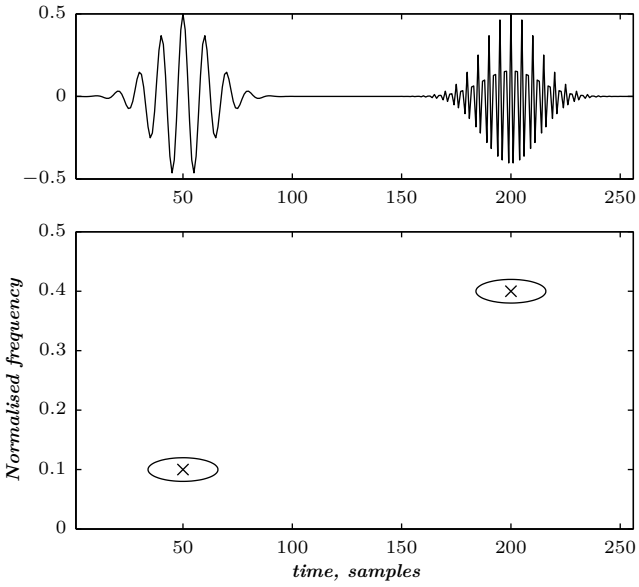


Figure II.4: Synthesised signal: two gaussian atoms, 256 samples.

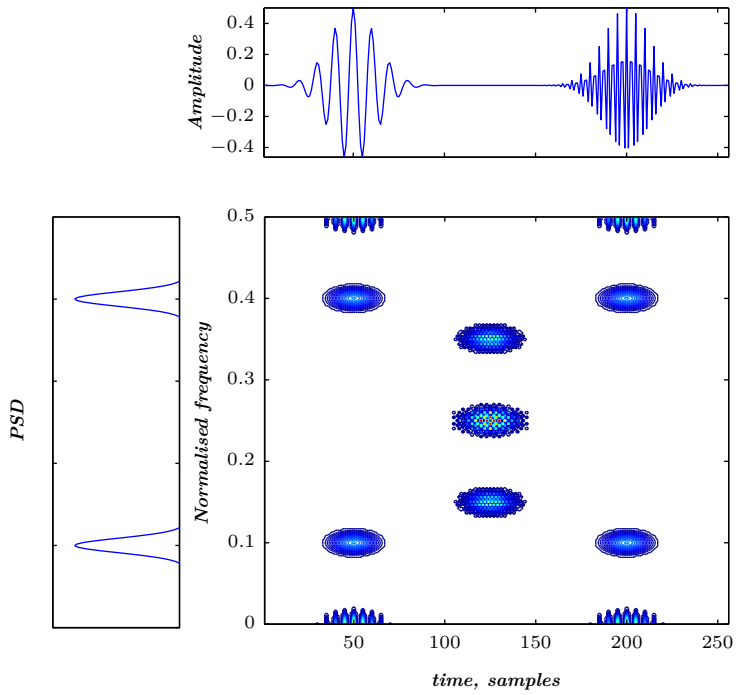


Figure II.5: WVD of the two gaussian atoms' signal (real signal) of Figure II.4.

As illustrated in Figure II.4, four terms appears in the WVD rather than two because of spectral aliasing. Additional spurious terms are also present due to interferences with negative normalised frequency terms located between $-0.5$ and 0. To remove these unwanted terms except for interference term occurring midway between auto–terms, the analytic version of the analysed signal is used to bring about a smoothed time–frequency distribution.

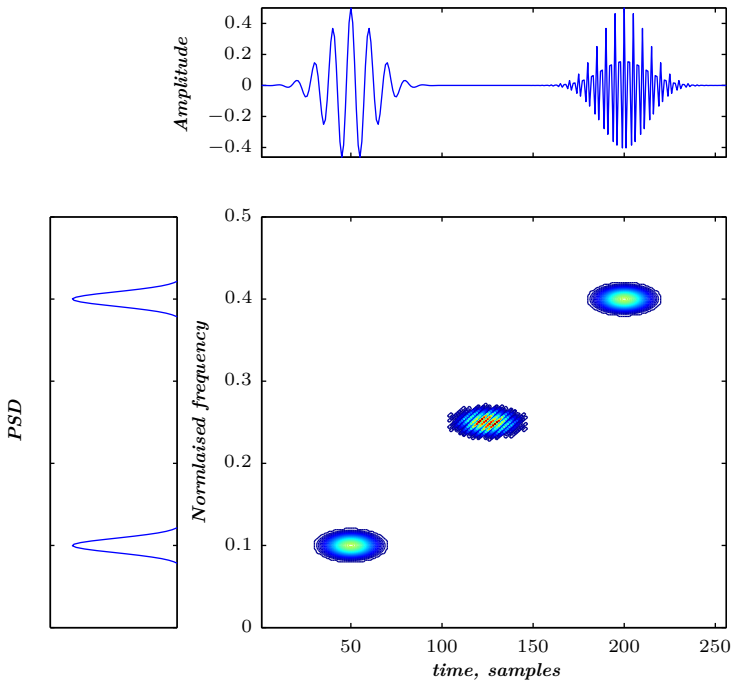


Figure II.6: WVD of the two gaussian atoms' signal (analytic signal) of Figure II.4.

As depicted in Figure II.6, auto–terms are well recognised with an unavoidable midway interfering term. Spectral aliasing disappears as well as interference between positive and negative frequencies. Indeed, the analytic signal as a complex version of the analysed signal shows its usefulness in improving the WVD representation. However, the remaining cross–terms needs additional smoothing through modified distributions to be removed.

### II.1.2 Pseudo Wigner–Ville distribution (PWVD)

The energy of the analysed signal can be estimated by using the term $q_x(t,\tau) = x\left(t+\frac{\tau}{2}\right)x^*\left(t-\frac{\tau}{2}\right)$. This formulation generates a windowed estimation of that energy since the analysed signal have a limited time support. The consequent distribution, which is inevitably a smoothed version of the WVD, is also known as Pseudo Wigner–Ville distribution (PWVD), as in (II.25);

$$PW_x(t,\nu) = \int_{-\infty}^{+\infty} h(\tau)\, x\left(t+\frac{\tau}{2}\right)\, x^*\left(t-\frac{\tau}{2}\right)\, e^{-j2\pi\nu\tau}\,\mathrm{d}\tau \qquad \text{(II.25)}$$

where $h(t)$ is the window function. This time windowing yields frequency smoothing of the WVD, as in (II.26);

$$PW_x(t,\nu) = \int_{-\infty}^{+\infty} H(\nu-\theta)\, W_x(t,\theta)\,\mathrm{d}\theta \qquad \text{(II.26)}$$

where $H(\nu)$ denotes the Fourier transform of $h(t)$. The obtained time–frequency distribution is smoothed over the frequency domain. However, this smoothing is carried out at the cost of losing some nice properties, *e.g.* marginals' property, unitarity, frequency support conservation. Moreover, each auto–term is widened within the time–frequency plane.

**Pseudo–WVD – practical illustration** As depicted in Figure II.7, frequency smoothing carried out through time windowing removes cross–terms oscillating perpendicularly to the frequency axis.

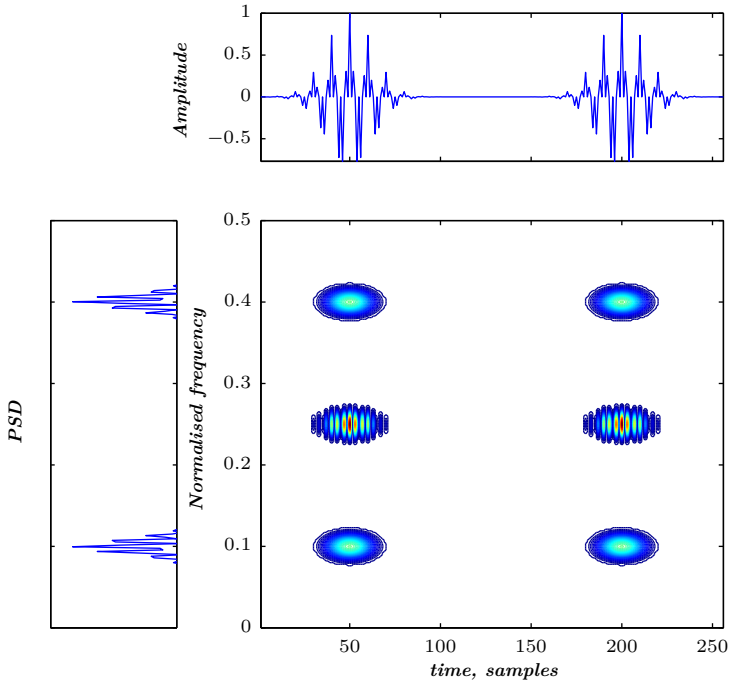


Figure II.7: PWVD of the Four gaussian atoms' signal (analytic signal) of Figure II.1.

Moreover, the analytic version of the analysed signal can be used to improve the obtained time–frequency representation calculated through PWVD. Figure II.8 illustrates the PWVD of the analytic version of the two gaussians' signal of Figure II.4. Indeed, auto–terms are well emphasised by removing cross–terms within the time–frequency plane.

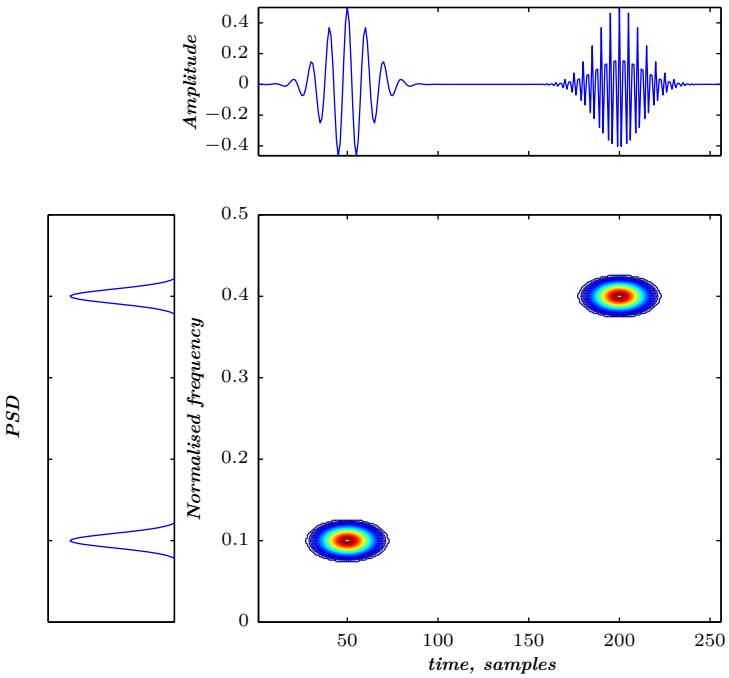


Figure II.8: PWVD of the two gaussian atoms' signal (analytic signal) of Figure II.4.

**WVD vs spectrogram** In order of highlight the benefits behind using the WVD, it is worthy to compare it with the spectrogram (section II.2.1). The spectrogram is quadratic, therefore, it is one of the Cohen's class distributions [62, 63]. The spectrogram is calculated by a linear then a bilinear operations. Firstly, the linear operator consists of a Fourier transform, and secondly the squared modulus as a bilinear operator is applied to the signal to be analysed. In contrast, the WVD begins with a quadratic estimation of the energy and then a Fourier transform is applied to the signal's energy according to (II.11) [64]. The spectrogram satisfies time and frequency covariance as well as property (II.3). However, its main downside is that marginal properties (II.4) and (II.5) which are not satisfied.

### II.1.3 The Cohen's class – definition

Covariance in time and frequency domains is the main property of the Cohen's class. Indeed, the distribution of a modulated and delayed signal is accordingly shifted within the time–frequency plane. This property makes the Cohen's class to be considered as the generalised formulation of the WVD, as in (II.27),

$$C_x(t,\nu;f) = \iiint_{-\infty}^{+\infty} e^{j2\pi\theta(s-t)}\ \phi(\theta,\tau)\ x(s+\frac{\tau}{2})\,x^*(s-\frac{\tau}{2})\,e^{-j2\pi\nu\tau}\,\mathrm{d}\theta\,\mathrm{d}s\,\mathrm{d}\tau \quad \text{(II.27)}$$

where $\phi(\theta, \tau)$ is an arbitrary function called the kernel [62] of the time–frequency representation. This two–dimensional function ensures smoothing the time and frequency domains. Different distributions are formulated by using different kernels which leads to design various time–frequency distributions.

The Cohen's class can also be defined equivalently in the frequency domain, as in (II.28);

$$C_x(t, \nu; \Pi) = \iint_{-\infty}^{+\infty} \Pi(s - t, \theta - \nu)\ W_x(s, \theta)\, \mathrm{d}s\, \mathrm{d}\theta \tag{II.28}$$

with

$$\Pi(t, \nu) = \iint_{-\infty}^{+\infty} \phi(\theta, \tau)\ e^{-j2\pi(\nu\tau + \theta t)}\, \mathrm{d}t\, \mathrm{d}\nu \tag{II.29}$$

Where $\Pi$ refers to the Fourier transform of the kernel $\phi$. For the WVD, the function $\Pi$ is a double Dirac impulse $\Pi(t, \nu) = \delta(t)\ \delta(\nu)$ also defined in the time domain by $\phi(\theta, \tau) = 1$.

According to the unified formulation of (II.28), the WVD is considered as the basic time–frequency distribution which allows to construct the overall distributions of the Cohen's class.

### II.1.4 Smoothed Pseudo Wigner–Ville Distribution (SPWVD)

By recalling the Moyal's formula in (II.19), the spectrogram can be considered as a smoothed WVD, as in II.30;

$$S_x(t, \nu) = \int_{-\infty}^{+\infty} W_h(s - t, \theta - \nu)\ W_x(s, \theta)\, \mathrm{d}s\, \mathrm{d}\theta \tag{II.30}$$

Therefore, the $\Pi(s, \theta) = W_h(s, \theta)$ smoothing function of the spectrogram is the WVD of the windowing function $h$. Therefore, the unavoidable time and frequency resolutions trade–off can be construed through the WVD of the windowing functions. The duration of the smoothing function defines the time resolution which is inversely proportional to frequency resolution. However, by considering an additional smoothing function $\Pi(t, \nu)$, as in (II.31),

$$\Pi(t, \nu) = g(t)\ H(-\nu) \tag{II.31}$$

where $H(\nu)$ is the Fourier transform of the smoothing window $h(t)$. The smoothing achieved through the function $\Pi(s, \theta) = W_h(s, \theta)$ of the spectrogram is now replaced by a double smoothing both in time and frequency domains. Therefore, time and frequency domains within the WVD are smoothed independently. The resulting distribution is known as the Smoothed pseudo Wigner–Ville distribution (SPWVD).

The SPWVD reduces the unwanted cross–terms of the WVD by two–dimensional low–pass filtering. This smoothing is achieved by a double convolution in time and frequency by two functions $g$ and $h$ through the kernel $\phi(u,\Omega) = g(u)H(\Omega)$ according to (II.32) [65];

The SPWVD has a separable smoothing kernel formed by $\Big(g(t), H(f)\Big)$ which provides an independent control of the time and frequency resolutions. For a zero time–resolution, i.e., $g(t) = \delta(t)$, the calculated SPWVD has no time smoothing. Thus, the resulting time–frequency distribution is the Pseudo–WVD (PWVD).

$$SPW_x(t,\nu) = \int_{-\infty}^{+\infty} h(\tau) \int_{-\infty}^{+\infty} g(s-t) x\left(s+\frac{\tau}{2}\right) x^*\left(s-\frac{\tau}{2}\right) \mathrm{d}s\, e^{-j2\pi\nu\tau} \mathrm{d}\tau \quad \text{(II.32)}$$

where $g$ and $h$ are two weighting functions.

Smoothing the time–frequency distribution affects localising the signal within the time–frequency plane. Therefore, a trade–off between interference attenuation and time–frequency localisation should be respected [66, 67, 62, 68, 57].

**SPWVD - practical illustration** Figure II.9 illustrates the SPWVD of the analytic version of a signal formed by 4 gaussian atoms (Figure II.1). The obtained time–frequency representation contains no interference terms but at the cost of widening each auto–term of the analysed signal.

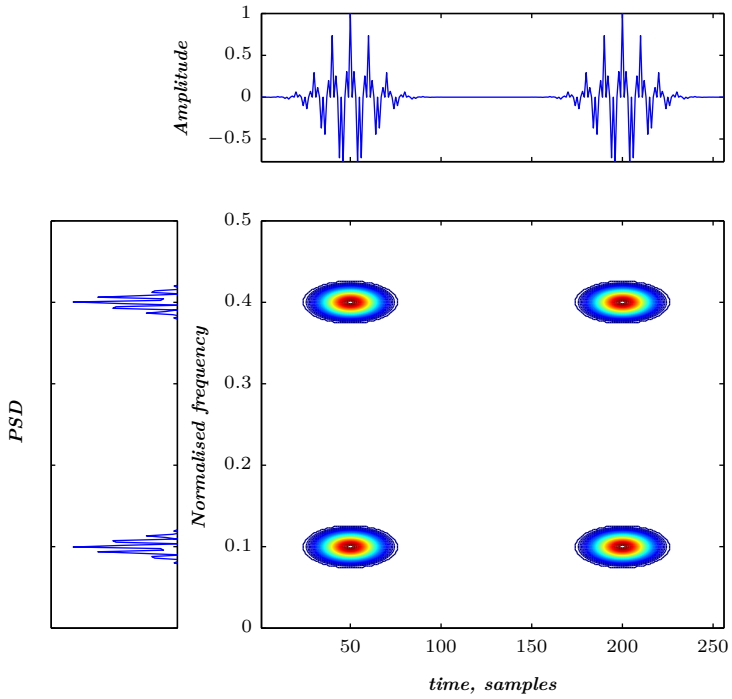


Figure II.9: SPWVD of the four gaussian atoms' signal (analytic signal) of Figure II.1.

### II.1.5 Reassigned Smoothed Pseudo Wigner–Ville Distribution (RSPWVD)

The reassignment method was first applied by Kodera *et al.* [69, 70] to the spectrogram to surpass its unavoidable Gabor–Heisenberg inequality [71, 57] to provide a better time–frequency representation. Auger *et al.* [72] studied the reassignment method and demonstrated its effectiveness to improve the readability of all the bilinear time–frequency representations. This method rearranges the coefficients of the time–frequency distribution around new zones to yield a high resolution TFR. Thus, this method can be used as a complement to any bilinear time–frequency distribution.

The reassignment method can be formulated by recalling the generalised time–frequency representation of the Cohen's class (section II.1.3). Integration within the time–frequency distribution in (II.27) refers to the sum of distributions at a point $(t,\omega)$ within the time–frequency plane. This is the sum of the terms $\phi_{TF}(u,\Omega)WV(x;t-u,\omega-\Omega)$ which represents the weighted coefficients of the WVD in the points at the vicinity of $(x;t-u,\omega-\Omega)$. Therefore, the distribution is concentrated at the time–frequency support of the kernel $\phi_{TF}(u,\Omega)$. Unfortunately, cross–terms are attenuated at the cost of spreading the auto–terms of the analysed signal. The modified time–frequency distribution attributes new values of each coefficient to its neighbouring centre of gravity according to (II.33) and (II.34) as follows;

$$\hat{t}(x;t,\omega) = t - \frac{\iint u\cdot\phi_{TF}(u,\Omega)WV_x(t-u,\omega-\Omega)\mathrm{d}u\dfrac{\mathrm{d}\Omega}{2\pi}}{\iint \phi_{TF}(u,\Omega)WV_x(t-u,\omega-\Omega)\mathrm{d}u\dfrac{\mathrm{d}\Omega}{2\pi}} \tag{II.33}$$

$$\hat{\omega}(x;t,\omega) = \omega - \frac{\iint \Omega\cdot\phi_{TF}(u,\Omega)WV_x(t-u,\omega-\Omega)\mathrm{d}u\dfrac{\mathrm{d}\Omega}{2\pi}}{\iint \phi_{TF}(u,\Omega)WV_x(t-u,\omega-\Omega)\mathrm{d}u\dfrac{\mathrm{d}\Omega}{2\pi}} \tag{II.34}$$

The reassigned time–frequency representation is then formulated by (II.35) as follows;

$$RTFR(x;t',\omega') = \iint TFR(x;t,\omega)\delta\Big(t'-\hat{t}(x;t,\omega)\Big) \cdot\delta\Big(\omega'-\hat{\omega}(x;t,\omega)\Big)\mathrm{d}t\frac{\mathrm{d}\omega}{2\pi} \tag{II.35}$$

where $\delta(.)$ denotes the Dirac impulse.

The reassigned distribution is time and frequency shift–invariant, and respects the energy conservation property. Moreover, the reassignment perfectly localises chirps [72]. The reassignment method [73] applied to the SPWVD modifies values of

the time–frequency representation by calculating the local centres of gravity $t_a(t,\nu)$ and $\nu_a(t,\nu)$ of the SPWVD in every point of the time–frequency representation, then by assigning the energetic content to the new point within the time–frequency plane according to (II.36) as follows;

$$|F_x(t,\nu)|^2 \longrightarrow S_x\Big(t_a(t,\nu),\nu_a(t,\nu)\Big) \tag{II.36}$$

Therefore, the reassignment method improves the readability of the calculated time–frequency representation by boosting the time and frequency resolutions [72, 73, 74].

**Reassigned–SPWVD – practical illustration** Figure II.10 illustrates the SPWVD of the signal formed by four gaussian atoms of Figure II.1 by smoothing functions $g$ and $h$ of 32 samples. The obtained time–frequency distribution is recovering the actual conent of the synthesised signal of Figure II.1. Therefore, the reassignment of time–frequency distributions should be a powerful method towards analysing the non–stationary content of phonocardiographic signals.

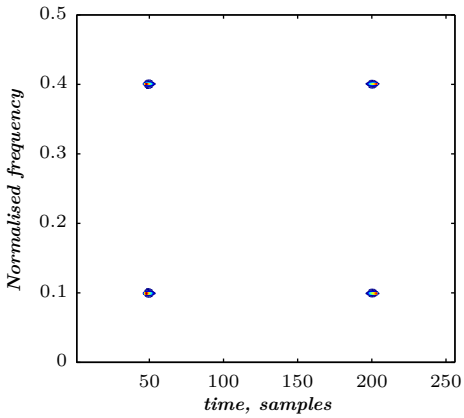


Figure II.10: RSPWVD of the four gaussian atoms' signal of Figure II.1: $g$ and $h$ functions of 32 samples.

### II.1.6 Additional methods

Several time–frequency methods exists with various properties. In this section, some time–frequency analysis methods are presented; namely Page distribution, Rihaczek distribution, Margenau–Hill distribution, and Choi–Williams distribution. Benefits and drawbacks of these methods are studied through their theoretical background, as well as practical illustrations applied on gaussian atoms based signals. This discussion supports selecting which method to be considered in analysing phonocardiogram signals.

**Page distribution** Power spectral density rules out representing the signal content in the time domain. To overcome this drawback, Page proposed a causal energy density calculated at each time instant through the overall duration of the signal.

Page considered a running time (denoted $t'$) and the present time (denoted $t$) to define the running spectrum of a signal. This causality reasoning is expressed as in (II.37);

$$\begin{aligned} X_t^-(\nu) &= \int_{-\infty}^{+\infty} x_t(t')\, e^{-j2\pi\nu t'}\, \mathrm{d}t' \\ &= \int_{-\infty}^{t} x_t(t')\, e^{-j2\pi\nu t'}\, \mathrm{d}t' \end{aligned} \tag{II.37}$$

where the $(-)$ sign refers to prior time instants observed down to $-\infty$. The cumulative energy up to instant $t$ is estimated as given in (II.38);

$$\int_{-\infty}^{t} P^-(t',\nu)\, \mathrm{d}t' = \left| X_t^-(\nu) \right|^2 \tag{II.38}$$

By differentiating (II.38) with respect to time, Page defined an instantaneous power spectrum based on the temporal variation of the causal energy density [57, 75]. Thus, the Page distribution is defined, as expressed in (II.39);

$$P^-(t,\nu) = \frac{\mathrm{d}}{\mathrm{d}t} \left| X_t^-(\nu) \right|^2 \tag{II.39}$$

This distribution is an element of the Cohen's class generated by a kernel $\phi$, such that $\phi(\theta,\tau) = e^{j\theta|\tau|/2}$. By substituting (II.37) in (II.38), the Page distribution can be expressed by (II.40) as follows;

$$\begin{aligned} P^-(t,\nu) &= \frac{\mathrm{d}}{\mathrm{d}t} \left\{ \left| \int_{-\infty}^{t} x(u)\, e^{-j2\pi\nu u} \mathrm{d}u \right|^2 \right\} \\ &= 2\Re \left\{ x^*(t) X_t^-(\nu)\, e^{j2\pi\nu t} \right\} \end{aligned} \tag{II.40}$$

According to its theoretical formulation, the Page distribution is a gradient of energy distribution of the analysed signal.

**The Rihaczek distribution** The Rihaczek distribution (RD) estimates the signal's energy within an elementary time and frequency intervals. The analysed signal is then viewed during a reduced temporal interval $\delta_T$ centred on instant $t$. The frequency support is also reduced to a band–pass filter $\delta_B$ centred on $\nu$. The signal $x(t)$ and its Fourier transform defines the signal's energy within a time–frequency box reduced to $\delta_T$ in time and to $\delta_B$ in frequency which yields a complex valued estimate of the signal energy around $(t,\nu)$ as expressed in (II.41);

$$\delta_T \delta_B \left[ x(t) X^*(\nu) e^{-j2\pi\nu t} \right] \tag{II.41}$$

According to (II.41), the Rihaczek distribution is defined as expressed in (II.42);

$$R_x(t,\nu) = x(t) X^*(\nu) e^{-j2\pi\nu t} \tag{II.42}$$

The Rihaczek distribution[7] is an element of the Cohen's class with a kernel $\phi(\theta,\tau) = e^{j\pi\theta\tau}$.

**The Margenau–Hill distribution** The real part of the RD is calculated to yield a new distribution named the Margenau–Hill distribution (MHD)[8]. This new distribution is also an element of the Cohen's class with $\phi(\theta,\tau) = \cos(\pi\theta\tau)$ as a kernel.

The main drawback of the RD and MHD is their interference structure which occur at different locations in comparison to the WVD. Interferences between two time–frequency regions located at $(t_1,\nu_1)$ and $(t_2,\nu_2)$ appears simultaneously at $(t_1,\nu_2)$ and $(t_2,\nu_1)$.

**The Margenau–Hill distribution – practical illustration** Figure II.11 illustrates the MHD of a synthesised signal formed by two gaussian atoms localised at $(n,f) = (50,0.1)$ and $(200,0.4)$ within the time–frequency plane. Indeed, cross–terms appears at inverted positions of the original gaussian atoms within the time–frequency plane; *i.e.* at $(50,0.4)$ and $(200,0.1)$.

[7] According to (II.41), the Rihaczek distribution is complex valued. It verifies several nice properties, namely; energy conservation, marginals properties, translation & dilation covariance, compatibility with filtering & modulation, wide–sense support conservation, unitarity, instantaneous frequency, and group delay.

[8] The Margenau–Hill distribution verifies several properties; energy conservation, marginal properties, real–valued, translation and dilation covariance, wide–sense support conservation, instantaneous frequency, and group delay.

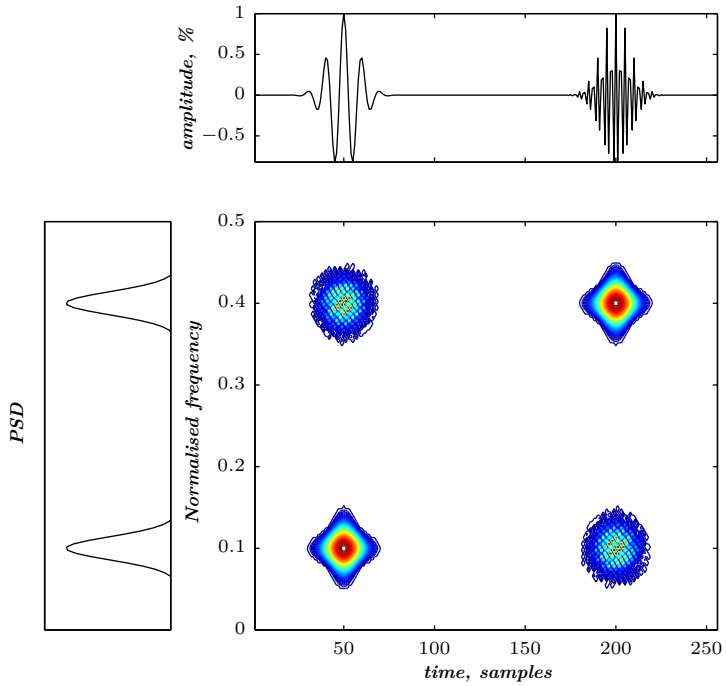


Figure II.11: Margenau–Hill distribution of the two gaussian atoms synthesised signal (Figure II.4): (n,f) = (50,0.1), (200,0.4). Duration: 256 samples.

This interference structure fails to adequately represent multicomponent signals since cross–terms can overlap with auto–terms of the analysed signal. Therefore, the Rihaczek and Margenau–Hill distributions are unsuited for the multicomponent content of PCG signals.

**The Choi–Williams distribution** The Choi–Williams distribution (CWD)[9] is defined through a joint–smoothing of the WVD by a kernel $\phi$ depending only on the product $\tau\theta$ as in (II.43);

$$\phi(\theta,\tau) = \Phi(\tau\theta) \tag{II.43}$$

where $\Phi$ is a decreasing function such that $\Phi(0) = 1$.

Interferences are reduced by the kernel $\phi$, which defines a category within the Cohen's class known as Reduced Interference Distributions (RIDs). The kernel which defines the Choi–Williams distribution is expressed by (II.44) as follows;

$$\phi(\theta,\tau) = e^{-\frac{(\pi\theta\tau)^2}{2\sigma^2}} \tag{II.44}$$

[9]The Choi–Williams distribution (CWD) verifies several properties, namely; energy conservation, marginals properties, real–valued, translation & dilation covariance, instantaneous frequency, and group delay.

According to the gaussian formulation of the kernel of (II.44), the Choi–Williams distribution is then expressed as in (II.45);

$$CW_x(t,\nu) = \sqrt{\frac{2}{\pi}} \iint_{-\infty}^{+\infty} \frac{\sigma}{|\tau|} e^{-\frac{2\sigma^2(s-t)^2}{\tau^2}} x\left(s+\frac{\tau}{2}\right) x^*\left(s-\frac{\tau}{2}\right) e^{-j2\pi\nu\tau} \mathrm{d}s\mathrm{d}\tau \tag{II.45}$$

Where $\sigma$ represents the kernel width, which controls interferences in the time–frequency plane; *i.e.* a best interference smoothing can be obtained for small values of $\sigma$. Conversely, the Choi–Williams distribution turns into a WVD for larger values of $\sigma$ tending to infinity.

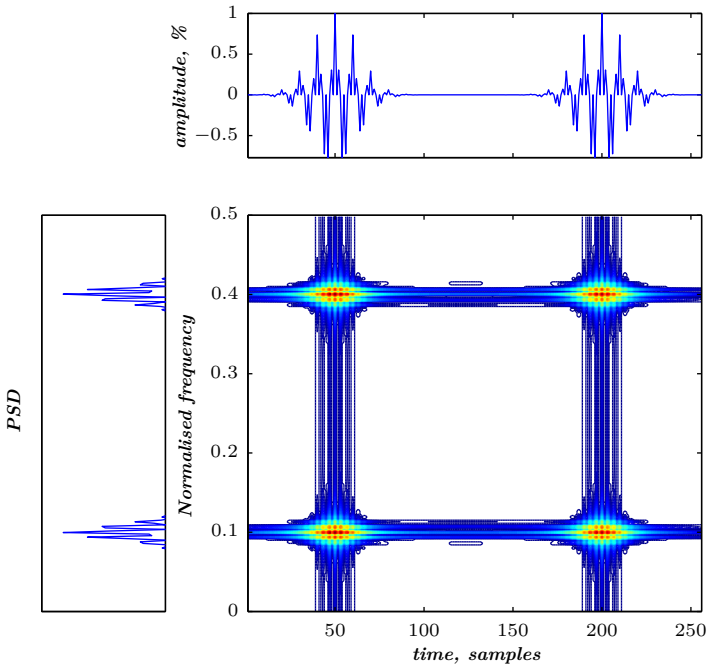


Figure II.12: Choi–Williams distribution (CWD) of a signal formed by 4 gaussian atoms: (n,f) = (50,0.1), (50,0.4), (200,0.1), (200,0.4). Duration: 256 samples.

The kernel of the CWD is interfering for regions localised at same time or frequency regions over the time–frequency plane. Therefore, the effectiveness of the CWD depends enormously on the content of the analysed signal.

**The Choi–Williams distribution – practical illustration** To highlight this interference structure, the 4 gaussian atoms of the signal of Figure II.1 are moved around each other within the time–frequency plane at different time and frequency supports which leads to 2 additional signals used for analysis.

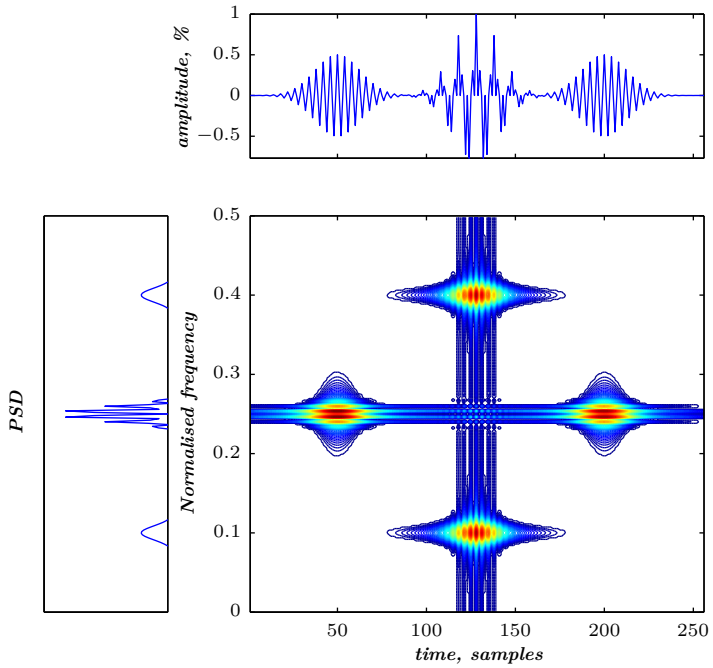


Figure II.13: Choi–Williams distribution (CWD) of a signal formed by 4 gaussian atoms: (n,f) = (50,0.25), (128,0.1), (128,0.4), (200,0.25). Duration: 256 samples.

By comparing Figures II.12, II.13, & II.14, the limitation of the CWD in analysing multicomponent signals became obvious. Indeed, Figures II.12 & II.13 show clearly that the interferences occurs between atoms sharing the same time and frequency supports.

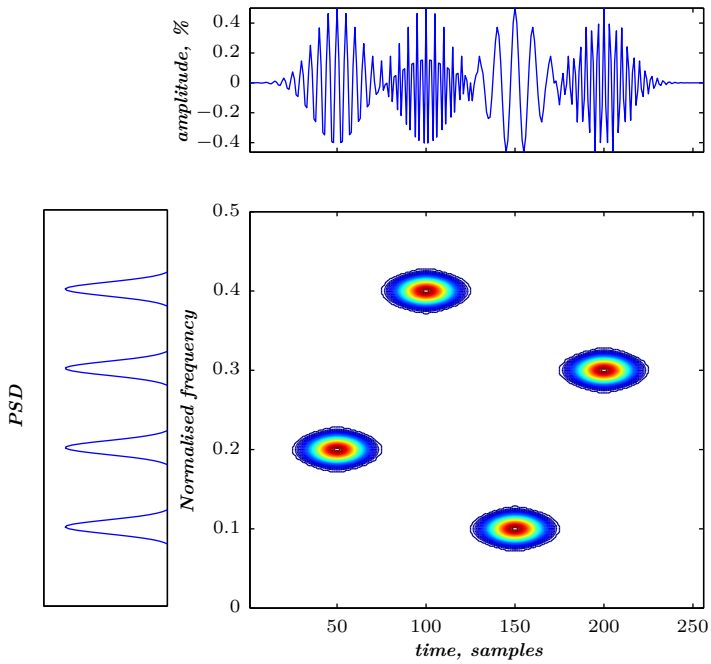


Figure II.14: Choi–Williams distribution (CWD) of a signal formed by 4 gaussian atoms: (n,f) = (50,0.2), (100,0.4), (150,0.1), (200,0.3). Duration: 256 samples.

Moreover, the CWD of Figure II.14 shows no interferences within the time–frequency plane since the atoms do not share the same time and frequency supports. Thus, interferences occurring between time–frequency regions at overlapping time and frequency supports is the main drawback of the CWD which is revealed to be unsuitable for analysing multicomponent signals such as PCG signals.

## II.2 Atomic decompositions

Fourier transform decomposes the signal into infinite sinusoids which is inappropriate for limited time–support signals. A time–frequency representation can be defined by sliding the analysis window over the time domain, which leads to the Short–time Fourier transform (STFT). This is the first trivial and basic time–frequency representation within atomic decomposition class also known as the Linear time–frequency representations class.

Wavelet transforms decompose signals into wavelets rather than infinite sinusoids as done by the STFT. The Continuous wavelet transform (CWT) represents the basic concept of time–scale analysis as a trivial extension of the STFT. This transition is theoretically achieved by replacing the infinite sinusoids by a zero–mean functions known as wavelets. These wavelets are generated by translating a mother wavelet dilated and compressed through the scale domain.

Mallat [76, 77, 78] proved that multiresolution analysis is a filtering process

achieved through Quadrature mirror filters (QMFs). Therefore, the Discrete wavelet transform (DWT) can be calculated by high–pass and low–pass filtering of the analysed signal over the analysis levels to yield approximations and details, respectively.

Additionally, wavelet packets (WP) is a natural extension of the DWT by decomposing every single node in approximation and detail. The obtained decomposition tree is a an extended tree of that of the DWT. All packets are of equal bandwidth up to half the sampling frequency of the analysed signal.

### II.2.1 Short–time Fourier transform

The Short–time Fourier transform (STFT) of a given signal $x(t)$ is defined as its sliding Fourier transform over the time domain, as in (II.46);

$$STFT_x(t, f; h) = \int_{-\infty}^{+\infty} x(u)\ h^*(u-t)\ e^{-j2\pi fu}\ \mathrm{d}u \tag{II.46}$$

where $h(t)$ is the analysis window.

This running spectrum can be improved by overlapping the sliding weighting windows to recover information at the beginning and the end of each window. According to Welch[79], the best overlapping can be reached at 50% of the weighting function duration.

The finite duration of the weighting function makes the STFT invertible, as in (II.47);

$$x(t) = \frac{1}{E_h} \iint_{-\infty}^{+\infty} STFT_x(u, \xi; h)\ h(t-u)\ e^{j2\pi u\xi}\ \mathrm{d}u\mathrm{d}\xi \tag{II.47}$$

where $E_h$ represents energy of the sliding window.

According to (II.47), the signal is decomposed into a sum of weighted functions formed by the weighting function and exponential term in (II.47), as in (II.48);

$$h_{t,f} = h(u-t)\ e^{j2\pi fu} \tag{II.48}$$

The instant $t$ becomes the localisation of the sliding window, and ensures the localisation of the STFT over the time–frequency plane. The signal is then decomposed into functions also known as *atoms*. The elementary atoms are formed by shifting the basic function $h(t)$ both in time and frequency. According the time–frequency duality, the STFT can also be expressed as in (II.49);

$$STFT_x(t, f; h) = \int_{-\infty}^{+\infty} X(\xi)\ H^*(\xi - f)\ e^{j2\pi t(\xi - f)}\ \mathrm{d}\xi \tag{II.49}$$

where $X$ and $H$ represent the Fourier transform of the analysed signal $x$ and the sliding window $h$, respectively. It became obvious that the STFT is the time–frequency representation of the filtered version of the analysed signal by a sliding

band–pass filter with a frequency response $H^*(\xi - f)$ centred at $f$ over the frequency domain. Therefore, the STFT is equivalent to a band–pass filter bank of constant bandwidth.

### The STFT – properties

The STFT preserves time and frequency shifts as in (II.50) and (II.51), respectively:

$$STFT_{\{x(t)\cdot e^{j2\pi t f_0}\}}(t, f; h) = STFT_{\{x(t)\}}(t, f - f_0; h) \tag{II.50}$$

$$STFT_{\{x(t-t_0)\}}(t, f; h) = STFT_{\{x(t)\cdot e^{j2\pi t_0 f}\}}(t - t_0, f; h) \tag{II.51}$$

The time and frequency resolutions of the STFT are inversely proportional. Therefore, a trade–off between the time and frequency resolutions should be ensured to get a better time–frequency representation. Indeed, a good time resolution can be reached by using a shorter weighting window $h(t)$ at the cost of a reduced frequency resolution, and vice versa.

### Spectrogram

The spectrogram is defined as the squared modulus of the STFT of a given signal $x(t)$. This transform is a linear projection combined with a quadratic operation which provides an energy estimation of the analysed signal [80], as in (II.52);

$$SPEC_x(t, \nu) = \left| \int x(\tau) h^*(\tau - t) e^{-j2\pi\nu\tau} \mathrm{d}\tau \right|^2 \tag{II.52}$$

where $h^*(t)$ is the sliding window.The spectrogram is faced to the same time and frequency resolutions trade–off of the STFT (section II.2.1), which is its main drawback. The spectrogram is a time and frequency smoothed version of the Wigner–Ville distribution [80]. Interferences exist within the spectrogram of a multicomponent signal at the midway region between autoterms over the time–frequency plane. This quadratic structure can be expressed as in (II.53);

$$SPEC_{x_1(t)+x_2(t)}(t, \nu) = SPEC_{x_1(t)}(t, \nu) + SPEC_{x_2(t)}(t, \nu) + \Re\Big\{SPEC_{x_1(t),x_2(t)}(t, \nu)\Big\} \tag{II.53}$$

where $SPEC_{x_1(t),x_2(t)}(t, \nu)$ represents the cross–spectrogram of $x_1(t)$ and $x_2(t)$, and $\Re$ denotes the real part.

The spectrogram respects the global energy distribution property as in (II.54);

$$\iint_{-\infty}^{+\infty} SPEC_x(t, \nu)\ \mathrm{d}t\ \mathrm{d}\nu = E_x \tag{II.54}$$

Since the spectrogram is covariant to time[10] and frequency[11] shifts, then it is an element of the Cohen's class.

### II.2.2 Wavelet transform

Wavelets were first introduced by Coifman, Meyer and Wickerhauser [81]. These functions are able to localise oscillations within a signal both in time and in scale domains. The scale parameter, which is introduced instead of frequency, take an inverse effect on the wavelet amplitude, so when the wavelet is dilated then its amplitude is reduced and vice versa. Wavelet transform known also as time–scale analysis is based on projecting the energy signal on a scale–varying basis functions, which cannot be accomplished by Fourier methods. Wavelet transform is revolutionary since the signal's energy is projected on a compact waves not infinite sinusoids as done through Fourier methods.

Wavelet packet (WP) ensues from the Discrete Wavelet Transform (DWT) which entails Quadrature Mirror Filters (QMFs) [82] to decompose the signal into its frequency subband versions. The DWT and WPs are non redundant in comparison to the Continuous Wavelet Transform (CWT), which calculate the wavelet transform at close values of the scale. The CWT is calculation time consuming since it is calculated as convolution between the analysed signal and the mother wavelet at different scales.

#### The refinement equation

The refinement equation of the scaling function $\varphi$ within wavelet analysis ensures multiresolution decomposition of analysed data. These functions combination allow to represent signals of finite energy at a given decomposition level $j$. Spaces formed by functions $V_j$ are conceived through the basis $\varphi\left(2^j t - k\right)$ at decomposition level $j$ and time shift $k$. Refinement of these spaces then formulated in (II.55).

$$V_j \oplus W_j = V_{j+1} \tag{II.55}$$

where $V_j$ and $V_{j+1}$ are spaces of functions at decomposition levels $j$ and $j+1$, respectively. The space $W_j$ is all functions combination of the Hilbert space $L^2$ resulting from the wavelet decomposition at level $j$. According to (II.56), this space contains the details of the signal and the $V_j$ spaces are the approximations spaces.

$$V_0 \subset V_1 \subset V_2 \cdots \tag{II.56}$$

where $V_0$ represents the coarse scale space, $V_1$ is the finer space, $V_2$ the even finer space and so on. The analysis is more finer according to the decomposition level which allow to qualify the wavelet analysis as multiresolution analysis. The space

[10] Time shift: $SPEC_{x(t-t_0)}(t,\nu) = SPEC_{x(t)}(t-t_0,\nu)$

[11] Frequency shift: $SPEC_{x(t-t_0)\cdot e^{j2\pi\nu_0 t}}(t,\nu) = SPEC_{x(t)}(t,\nu-\nu_0)$

$V_0$ is formed by all combinations of functions $\varphi$ with a temporal shift $k$ which can be denoted by $\varphi(t-k)$. Similarly, the $V_1$ space is constructed by all shifted combinations of functions $\varphi$ with a dyadic dilation of the time domain which provides squeezing of functions of this space in comparison to $V_0$ functions. Functions within the space $V_1$ are formulated as $\varphi(2t-k)$.

Let us consider the function $\varphi$, which is an element of $V_0$, to be expressed in terms of functions of the space $V_1$. Since $V_0 \subset V_1$, the function $\varphi$ can be written as combination of functions belonging to the space $V_1$ according to Equation (II.57).

$$\varphi(t) = 2\sum_{k=0}^{N} h_0(k)\,\varphi(2t-k) \tag{II.57}$$

where $h_0(k)$ represents coefficients defined by Mallat [78, 76]. According to (II.57), the function $\varphi$ is a convolution product between combination of the squeezed functions $\varphi(2t-k)$ and coefficients $h_0(k)$. Since $V_0$ is the resulting space of this convolution which represents the coarse scale, then coefficients $h_0(k)$ forms a low–pass filter. This is a key finding of researchers at the early 1980's, highlighting that there is no need to calculate a direct projection of a signal through a wavelet basis, but only low–pass filtering provides the same approximation space $V_0$.

### Continuous Wavelet Transform (CWT)

Wavelet transform [83, 82, 84] consists of sweeping the signal to be analysed by a mother wavelet at different levels. The Continuous Wavelet Transform $CWT_{a,b}$ of a given signal $x(t)$ is defined as the inner product between the signal and scaled and translated versions of the mother wavelet $\psi_{a,b}(t)$ as in (II.58);

$$CWT_{a,b}\{x(t)\} = \int_{-\infty}^{+\infty} x(t)\psi^*_{a,b}(t)\mathrm{d}t \tag{II.58}$$

where the asterisk denotes the complex conjugate.

The analysed signal is projected into a wavelet basis constructed by shifted and scaled versions of a *mother wavelet* as in (II.59).

$$\psi_{a,b}(t) = \frac{1}{\sqrt{|a|}}\psi\left(\frac{t-b}{a}\right) \tag{II.59}$$

where $a$ and $b$ represent the scale and time shift respectively. The factor $|a|^{-1/2}$ ensures energy normalisation. The wavelet should vanish rapidly and therefore satisfy the admissibility condition given in (II.60).

$$\int_{-\infty}^{+\infty} \psi(t)\; dt = 0 \tag{II.60}$$

The continuous nature of the CWT is about calculating coefficients of the wavelet transform at every scale. Therefore, shifting wavelets during computation is smooth so the CWT can be qualified as continuous. Unfortunately, this calculation structure makes the CWT redundant since neighbouring coefficients are of correlated values. Hence, The CWT is of heavy computation time which imply a reduced number of samples to be processed which is not coherent with monitoring biomedical signals done generally for long durations.

**Scalogram** Similarly to the spectrogram structure, the scalogram is defined as the squared modulus of the wavelet transform. The obtained time–frequency distribution preserves the energy of the analysed signal in both time and scale domains as in (II.61);

$$\iint_{-\infty}^{+\infty} |CWT_x(t,a;\psi)|^2 \, \mathrm{d}t \, \frac{\mathrm{d}a}{a^2} = E_x \tag{II.61}$$

The scalogram respects the same resolution behaviour of the wavelet transform. The time and frequency resolutions varies with the scale within the time–scale plane.

**Scalogram – practical illustration** To highlight the content dependent behaviour of the time and frequency resolutions of the scalogram, a signal formed by four atoms at $(t,f) = (50,0.2),(100,0.4),(150,0.1),\text{and}(200,0.3)$ over the time–frequency plane is considered for analysis, also used in Figure II.14. The time–scale representation is converted to a time–frequency representation by rearranging[12] the scalogram coefficients according to the central frequency of the mother wavelet.

[12] $F_a = \dfrac{F_c}{a \cdot \Delta}$, where $a$: scale, $\Delta$: sampling period, $F_c$: central frequency of the mother wavelet, $F_a$: pseudo–frequency corresponding to $a$.

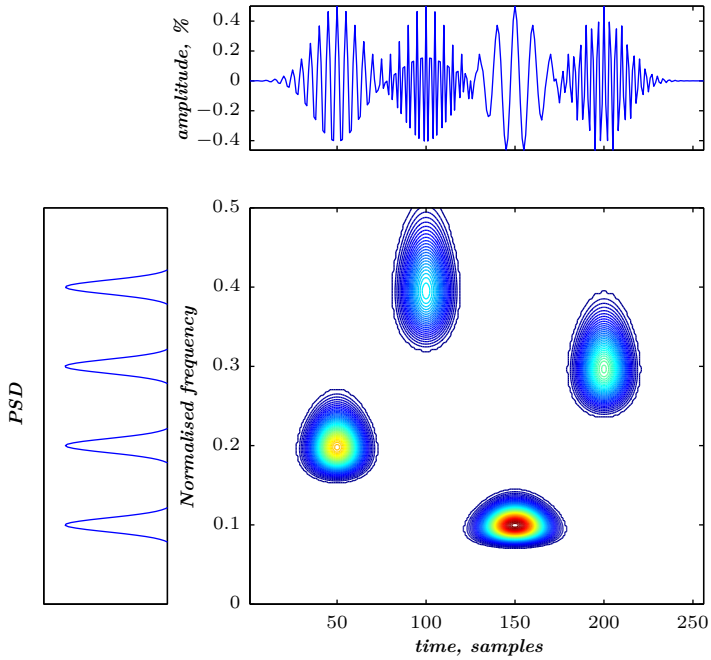


Figure II.15: Scalogram (Morlet wavelet) of the 4 gaussian atoms' signal at $(t, f) = (50, 0.2), (100, 0.4), (150, 0.1), (200, 0.3)$.

Indeed, as illustrated in Figure II.15, the four gaussian atoms are spread for higher scale values over the time domain with a better frequency resolution. For lower scale values, the atoms are narrower according to the time domain but spread through the frequency domain. Therefore, the frequency resolution increases as the signal's frequency decreases. Moreover, the obtained time–frequency distribution obviously confirms the cone shape of the scalogram through the scale domain.

### Discrete Wavelet Transform (DWT)

The Discrete Wavelet Transform (DWT) became a widely used method within advanced digital signal processing techniques thanks to the fast wavelet transform (FWT) developed by Mallat in 1988 [76]. The DWT allow quantifying the signal's energy over the frequency domain by means of quadrature mirror filters (QMFs) [78, 76, 77]. Indeed, as depicted in Table II.1, the signal to be analysed is high–pass and low–pass filtered at every decomposition level. The high–pass and low–pass filters yields high and low frequency contents called approximation (A) and detail (D), respectively.

Only approximations are split at every decomposition level.

| Level | Bandwidth | Signal, up to $\frac{F_s}{2}$ | | | | | | | |
|---|---|---|---|---|---|---|---|---|---|
| 1 | $\frac{F_s}{4}$ | A | | | | D | | | |
| 2 | $\frac{F_s}{8}$ | AA | | AD | | — | | — | |
| 3 | $\frac{F_s}{16}$ | AAA | AAD | — | — | — | — | — | — |

Table II.1: Frequency bands decomposition by the DWT.

| Level | Bandwidth | Signal, up to $\frac{F_s}{2}$ | | | | | | | |
|---|---|---|---|---|---|---|---|---|---|
| 1 | $\frac{F_s}{4}$ | A | | | | D | | | |
| 2 | $\frac{F_s}{8}$ | AA | | AD | | DA | | DD | |
| 3 | $\frac{F_s}{16}$ | AAA | AAD | ADA | ADD | DAA | DAD | DDA | DDD |

Table II.2: Frequency subbands decomposition by wavelet packets

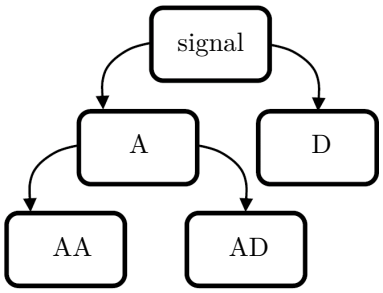


Figure II.16: Binary tree structure of the Discrete Wavelet Transform (DWT) at two decomposition levels.

**Wavelet packets**

A library of wavelet packets bases of orthogonal mother wavelet is a reliable tool for decomposing a given signal into subband signals. Wavelet packets is a reliable tool towards decomposing a given signal into its forming spectral subbands. The decomposition is achieved through quadrature mirror filters (QMFs) of an orthonormal base. The energy of the analysed signal is therefore partitioned according to each node through the binary tree of wavelet packets. The wavelet packet decomposition (WPD) is an obvious extension of the DWT which decomposes a signal into approximation and detail for every level as illustrated in Table II.2 and Figure II.17.

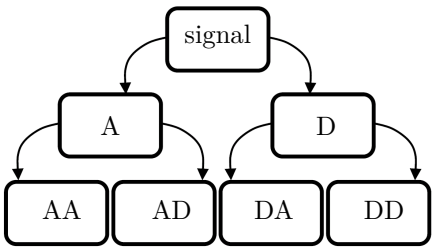


Figure II.17: Binary tree structure of wavelet packets at two decomposition levels.

Wavelet packets splits every detail for each decomposition level in approximation and detail. This is a time–scale method which provides successive filtering of the original signal into elementary signals at each decomposition level. Orthonormal wavelet packet bases involve quadrature mirror filters (QMFs) to represent the frequency content of a signal into multiple subbands. A discrete signal of $N$ samples can be decomposed into $2^{N/2}$ wavelet packet bases [77].

## II.3 Conclusion

In this chapter, various time–frequency methods were studied according to their theoretical background. Moreover, their practical structure were investigated through comparative examples to show their advantages and drawbacks. Two main categories gather the studied time–frequency methods; namely energy distributions and atomic decompositions.

The first methods' family is formed on the base of the Wigner–Ville distribution (WVD). The analysis kernel is key to define the Cohen's class. Indeed, the Cohen's class is naturally introduced through properties unifying several time–frequency methods with various analysis kernels. The theoretical study of these methods allows to select the appropriate methods to be used during analysis of phonocardiographic signals. The Cohen's class, also known as shift–invariant class, yields a generalised view of time–frequency methods.

The second family is basically formed on time–scale methods. Firstly, the Short–time Fourier transform (STFT), as a running spectrum over the time domain, decomposes the signal's energy through an exponential basis. The main drawback of the STFT is its inevitable time and frequency resolutions trade–off. The wavelet transform resolves this issue by ensuring a multiresolution analysis by decomposing the signal on a convenient waveform basis. However, selecting the mother wavelet during analysis over all existing wavelets still a problematic issue during analysis.

The spectrogram and the scalogram, which are the squared modulus of the STFT and the wavelet transform respectively, define atomic energy distributions. The spectrogram verifies some properties which make it an element of the Cohen's class.

The scalogram is an affine distribution which defines the affine energy distributions' class.

Additionally, wavelet packets as well as the discrete wavelet transform are powerful tools as multiresolution time–scale analysis methods. However, the main practical issue in time–scale analysis is selecting the mother wavelet to be used for decomposing phonocardiographic signals. Wavelet that respects orthogonality are required in wavelet packets to adequately represent energy of the analysed signals.

# Chapter III

# Time–frequency analysis of phonocardiograms

This chapter presents analysis results of phonocardiographic signals by time–frequency representations. The analysed data emanates from two sources; from the "LGB–IRCM Cardiac Valve Database" recorded at the "Institut de recherches cliniques de Montréal" and at the "Montreal General Jewish Hospital" in Quebec (Canada), and from the "Centre hospitalier universitaire de Tlemcen (Algeria)" recorded by the author by means of the *PCG Recorder* system (Figure III.1) **developed** during this work.

The intracardiac valvular functioning is to be explored within the time–frequency plane by energy distributions as well as atomic decompositions applied to heart sounds and murmurs. Each analysis methods' category is useful for a specific purpose.

The intracardiac activity is to be explored by time–frequency analysis methods. Indeed, Wigner–Ville based distributions with their high performance in representing multicomponent signals are to be applied to phonocardiographic signals. Thus, time and frequency smoothing over the time–frequency plane of the Smoothed pseudo Wigner–Ville distribution is to be applied on simulated and real PCG signals of the CHUT[1] and the LGB–IRCM[2] cardiac valve database. Improvement of the computed SPWVD can be achieved through reassignment of the obtained time–frequency representation. The scalogram computed as square modulus of the CWT rearranges coefficients of the time–scale representation into a time–frequency representation. An adapted mother wavelet to heart sounds is to be developed to achieve an ad hoc time–frequency representation of phonocardiographic signals. Additionally, wavelet packets reduces the redundancy of the CWT through elementary energy packets at various frequency subbands.

This chapter is partitioned into four sections. Section III.1, entitled "Phonocardiographic data", presents information about phonocardiographic signals recorded

[1]Centre hospitalier universitaire de Tlemcen, Algeria

[2]Laboratoire de génie biomédical–Insitut de recherches cliniques de Montréal, Quebec, Canada

within the CHUT (Centre hospitalier universitaire de Tlemcen), and emanating from the LGB–IRCM cardiac valve database. Section III.2, entitled "Segmentation of PCG signals", presents algorithms and segmentation results of phonocardiographic signals of the LGB–IRCM cardiac valve database. Section III.3, entitled "Time–frequency analysis of PCG signals" presents various developed analysis and detection techniques of phonocardiographic signals within the time–frequency plane. Finally, section III.4, entitled "Wavelet analysis applied to PCG signals" presents analysis results of phonocardiographic signals by the Continuous wavelet transform and wavelet packets.

## III.1 Phonocardiographic data

Phonocardiographic data analysed in this work originate from two sources. Firstly, from the CHUT[3] where several PCG signals were recorded using a phonocardiographic recording system. This system was *developed* within this present work by the author to record various PCG signals of patients admitted to the Cardiology department of the CHUT. Secondly, phonocardiographic data from the LGB–IRCM cardiac valve database, which are simultaneously recorded with an ECG signal for segmentation purposes.

### III.1.1 The CHUT database

A novel data acquisition system, named *PCG Recorder*, has been *developed* by the author [2, 3] to record phonocardiographic signals at the cardiology department of the Teaching hospital of Tlemcen.

#### Hardware

In comparison to data acquisition equipment, the *developed* system is largely cheaper. The hardware of our data acquisition system is based on sound cards of personal computers which are widely available nowadays. The hardware equipment consists of a stethoscope membrane, a microphone, an audio cable and a soundcard of a personal computer as illustrated in Figure III.1.

[3] Centre hospitalier universitaire de Tlemcen, Algeria.

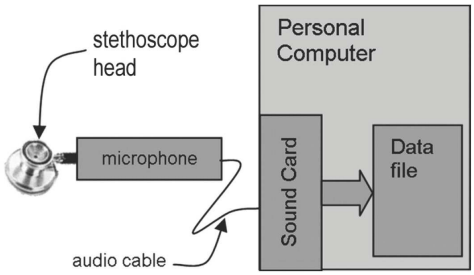


Figure III.1: PCG data acquisition system.

The acoustic probe is formed by a microphone, a stethoscope membrane, as well as an audio cable and an audio connector which are necessary to assemble all parts together as depicted in Figure III.2. Vibrations are then carried through the microphone which is connected to the analog input of a soundcard of a personal computer.

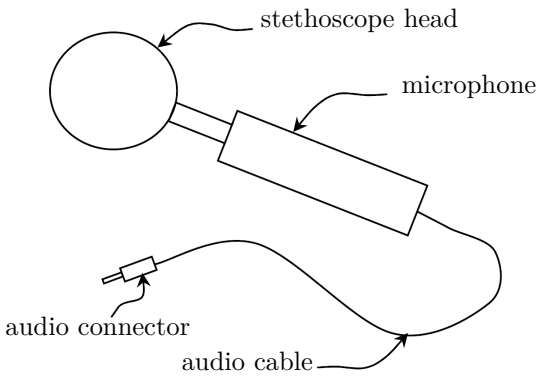


Figure III.2: Heart sounds' probe.

### Software

The software consists of a GUI[4] (Figure III.3) *developed* under a MATLAB environment. The core of this GUI allows acquisition of the analog input of the soundcard of a personal computer. The driving program uses functionalities of the *Data Acquisition Toolbox* of MATLAB for monitoring the acquisition task.

[4]Graphical User Interface

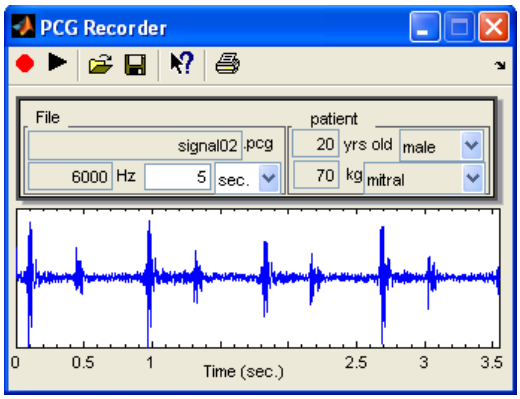


Figure III.3: PCG Recorder GUI [2, 3] *developed* under a MATLAB environment.

The *PCG Recorder* system acquires data at 16 bits resolution and a sampling frequency selected according to Nyquist sampling rate to avoid spectral aliasing. The acquired signal and patient clinical information are both saved within the same PCG data file with '.PCG' extension. Several parameters are saved within this data file, especially the sampling frequency. Moreover, clinical information of the examined patient are also stored as metadata within the same data file, *e.g.* the sex, age and weight of the patient as well as the auscultation area where the stethoscope membrane was placed during the recording.

#### Phonocardiogram Recording

Phonocardiographic data were acquired at the Cardiology department of the CHUT. Several cardiac disorders were investigated through PCG signals recorded *in situ* by means of the *developed* data acquisition system (*e.g.* aortic regurgitation, aortic stenosis, mitral regurgitation, mitral stenosis, pericardial friction rub, and ventricular septal defect).

Patients were diagnosed by experienced cardiologists. In a quiet room, the acoustic probe (Figure III.1) has been carefully positioned on the chest of the patient. However, the background noise is not avoidable during the recording process. Each patient recording includes PCG signals recorded from the four basic auscultation areas; namely the mitral, tricuspid, aortic and pulmonic areas.

### III.1.2 The LGB–IRCM cardiac valve database

This database is formed by simultaneously recorded ECG & PCG signals. The recording is carried out in the IRCM[5] and the Montreal JGH[6] on 172 patients with

[5]Institut de recherches cliniques de Montreal, Québec, Canada.
[6]Montral Jewish General Hospital, Quebec, Canada.

a prosthetic heart valve placed in the aortic or mitral cardiac orifices.

Among these patients, 108 patients had a bioprosthesis in the aortic position, 45 patients had a bioprosthesis in the mitral position, 3 patients had a mechanical prosthesis in the aortic position, 11 patients had a mechanical prosthesis in the mitral position. Five patients had a double valve replacement.

The patient was placed in dorsal decubitus in a recording room. The back of the bed was raised to have 45° between the bust of the patient and the horizontal plane. After that, a thorax auscultation had been carried out to localise the auscultation areas on the chest of the patient. Subsequently, the recording was carried out after 5 minutes rest and calm breathing. A precordial multi–sites recording was carried out from the aortic, pulmonary, left ventricular, and apical auscultation areas. For each PCG recording, the ECG (derivation II) signal was simultaneously recorded.

The PCG signal was band–pass filtered between cut–off frequencies of 50 and 2 kHz. The PCG and ECG signals were digitised by a 12 bits analog–to–digital converter on IBM–PC computer at sampling rates of 5 kHz and 500 Hz respectively. The ECG was recorded to be used as a reference signal in segmenting the PCG signal in systole and diastole phases. Each recording contains approximately 30 cardiac cycles.

## III.2 Segmentation of PCG signals

Phonocardiographic data of the LGB–IRCM cardiac valve database are segmented into systole and diastole phases before any analysis. This segmentation provide an averaged systole and diastole PCG signals. By joining these phases, a global overview of heart sounds is reached through the averaged cardiac cycle PCG signal of a considerably reduced background noise. This systole and diastole PCG segmentation is accomplished by detecting their synchronised waves within the simultaneously recorded ECG signal, namely the R peak and the end of the T wave.

This ECG waves detection is achieved by an algorithm proposed and validated by Zhang *et al.* [85, 86]. This algorithm allows to localise the R–peak and the end of the T–wave of the simultaneously recorded ECG signal, which are synchronised with the beginning of the S1 and S2 heart sounds, respectively. The R-peaks within ECG signals are detected by parabolic fitting. The T–waves of ECG signals are detected by calculating an integration in a sliding window which reaches its maximum at the end of these waveforms. The T–wave detection is based on its concavity feature and do not require any threshold assumption. This algorithm is validated on the QT database [87] of PhysioNet[7] by taking into account the noise level and the waveform morphology variation within the ECG signal. Zhang's algorithm ensures correct detection of systole and diastole phases for almost all ECG signals of the LGB–IRCM cardiac valve database.

[7] www.physionet.org

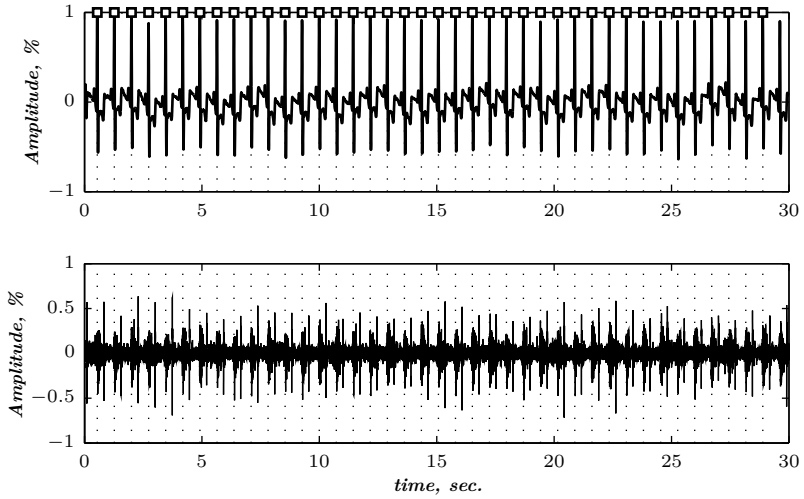


Figure III.4: Segmentation of the PCG signal in systole and diastole using an ECG–based R and T waves detection, LGB–IRCM cardiac valve database, data file: 10001.11 (40 cardiac cycles).

Before analysing PCG signals, the first and second heart sounds are adjusted among the running cardiac cycles by a cross–correlation algorithm developed within this work. The adjusted heart sounds are illustrated in Figure III.5. This novel technique overcomes jitter of the S2 heart sound among the segmented PCG signal.

## III.3 Time–frequency analysis of PCG signals

The Wigner–Ville distribution and its smoothed and reassigned versions are of great interest towards analysing heart sounds and murmurs. These bilinear methods overcome the basic time–frequency trade–off the spectrogram.

Xu *et al.* [88, 89] demonstrated that heart sounds are mainly formed by frequency modulated chirps. Furthermore, as argued by Boashash [90], the Wigner–Ville Distribution (WVD) can adequately represent chirps. Therefore, WVDs and its improved versions should yield high resolution time–frequency representations of heart sounds.

Time–frequency representations can also be generated through time–scale analysis. Indeed, the estimation of the central frequency of the mother wavelet within a Continuous wavelet transform (CWT) allow to rearrange the coefficients of the time–scale representation of the analysed signal [8, 91]. Since heart sounds are of frequency modulated chirp content, a chirp–based mother wavelet was studied and validated as a mother wavelet. Wavelet packet are then used as a global method to quantify the pathological nature of the analysed PCG signals.

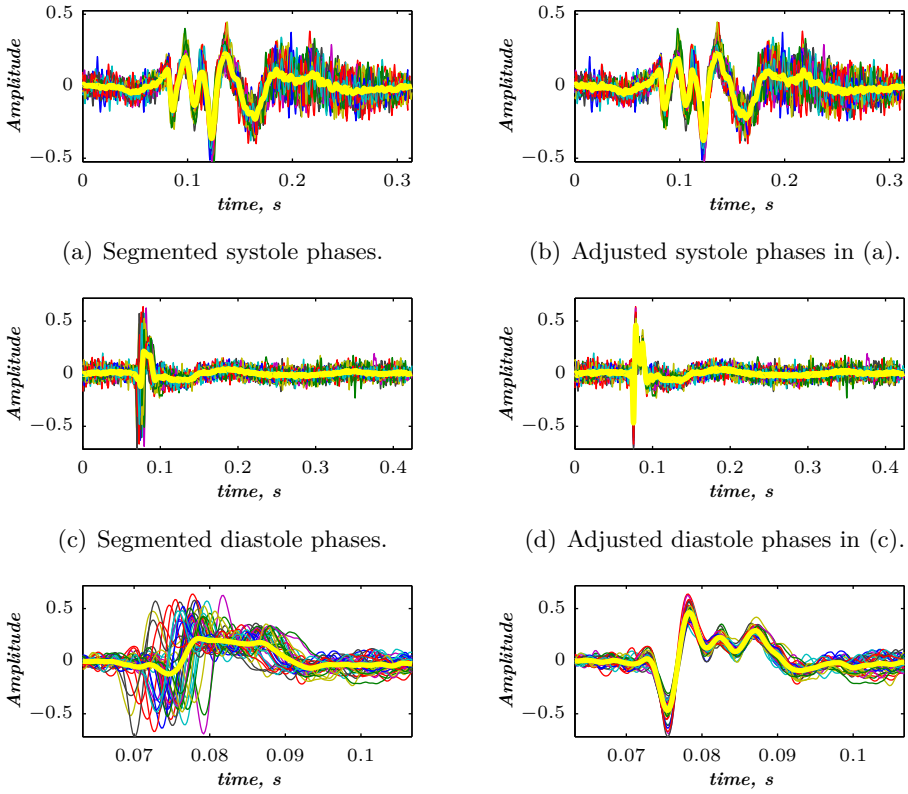


(a) Segmented systole phases.

(b) Adjusted systole phases in (a).

(c) Segmented diastole phases.

(d) Adjusted diastole phases in (c).

(e) S2 heart sound in (c).

(f) S2 heart sound in (d).

Figure III.5: Cross–correlation adjustment of the systole and diastole phases of the PCG signal within the LGB–IRCM data file: 10001.11. (a) Segmented systole phases, (b) Adjusted systole phases, (c) Segmented diastole phases, (d) Adjusted diastole phases.

### III.3.1 SPWVD of normal and abnormal PCGs

Using the acquisition system [2] described in section III.1.1, normal and abnormal heart sounds are recorded with appropriate settings. Phonocardiographic signals are recorded from the aortic, tricuspid, mitral and pulmonic auscultation areas.

#### SPWVD of normal heart sounds

At isovolumetric ventricular contraction, the closure of the mitral and tricuspid heart valves constitute the main origins of the first heart sound (S1) [92]. Indeed, as illustrated in Figure III.6; the S1 heart sound recorded from the aortic auscultation area is the more attenuated when compared to the other auscultation areas. This is due to the remoteness of the stethoscope head from its originating heart valves (mitral and tricuspid). Thus, at the mitral auscultation area, the first heart sound (S1) is stronger at its beginning, which should be the mitral valve contribution (M1).

From the aortic auscultation area, the aortic heart valve closure contributes strongly to the second heart sound (S2).

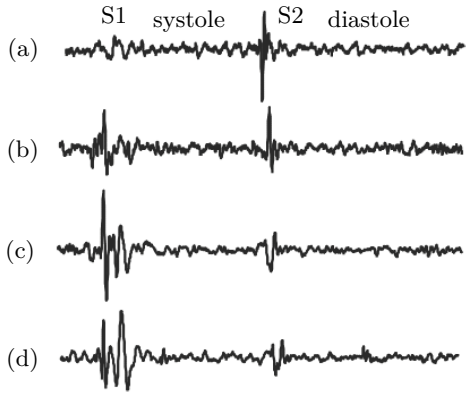


Figure III.6: Phonocardiogram signals (one cardiac cycle) of a normal subject recorded from the (a) aortic, (b) tricuspid, (c) mitral and (d) pulmonic auscultation areas.

Time–frequency representations (TFRs) of Figure III.7 are illustrated as bidimensional images, represented by gray tone changing from white (lower values) to black colour (higher values). Smoothing carried out by the SPWVD is obviously well characterising heart sounds within the time–frequency plane.

Thus, the SPWVD is suitable for the analysis if such non–stationary signal which still confusing the medical staff about its components origins. We should notice that the position of the acquiring stethoscope over the chest wall of the patient between mitral, tricuspid, aortic and pulmonic auscultation areas is filtering the acquired PCG signal carried out by the heart–thorax system hypothesised by Durand *et al.* [4]. Therefore, time–frequency bursts upon the obtained results could be related to the closer valves and cavities within the myocardium.

The acquisition carried out from the aortic auscultation area, as illustrated by Figure III.7(a); allow us to attribute the burst localised below 50 Hz to the aortic valve within the S1 heart sound spectral content. Thus, the snapping of the atrioventricular heart valves (mitral and tricuspid) could be filtered by the heart–thorax system as also quoted by Durand *et al.* [5]. As depicted by Figure III.7(b), for the tricuspid auscultation area, the relatively strong burst localised at the vicinity of 60 Hz could be related to the mitral valve activity. The tarnished second heart sound S2 is slightly marking frequencies below 50 Hz. As shown in Figure III.7(b), only the tricuspid auscultation area allows the S1 and S2 heart sounds to be recorded with comparative amplitudes. Moreover, the shape of the clearly delimited bursts in Figure III.7 confirms modulation laws hypothesis towards heart sounds content also quoted by Wood *et al.* [93, 94]. Thus, the first and second heart sounds, S1 and

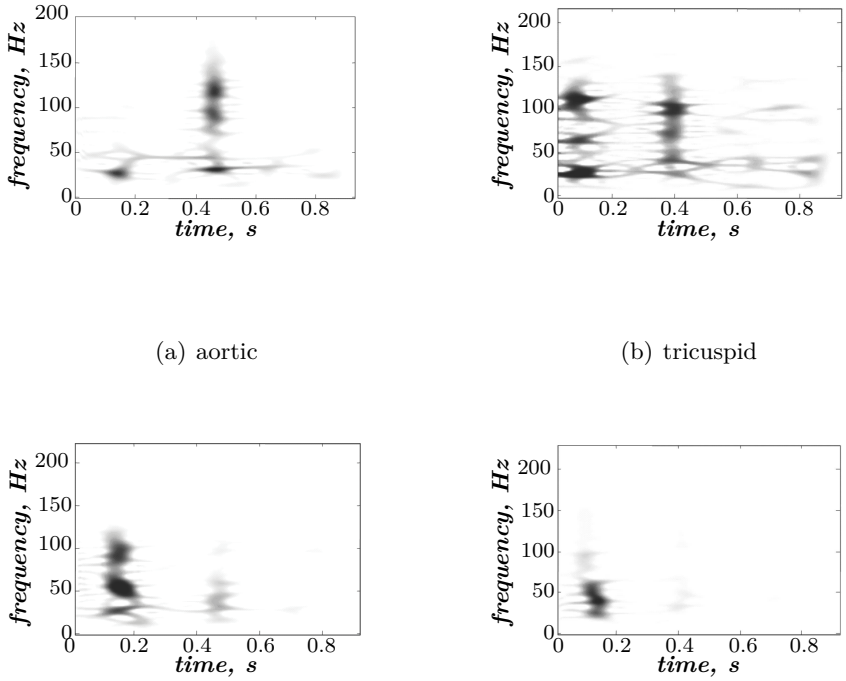


(a) aortic

(b) tricuspid

(c) mitral

(d) pulmonary

Figure III.7: SPWVDs of normal PCG signals of Figure III.6:(a) aortic, (b) tricuspid, (c) mitral, and (d) pulmonic auscultation areas.

S2, are mainly generated by atrioventricular valves snapping as well as intracardiac blood flow circulation.

Thus, the spectral activity in the S1 heart sound in Figure III.7(a) concerns the aortic valve opening. Spectral bursts of each TFR within Figure III.7 are summarised in Table III.1 shown below. Indeed, we remark that spectral contents of S1 and S2 are alternating between each chest wall auscultation area. For instance, the 25 Hz component appears in S1 heart sound when acquired from the four auscultation areas, and is absent at the pulmonic area. Thus, this spectral component could be the effect of the tricuspid heart valve snapping.

The finding that should emphasise is the obvious alternating aspect of the frequency regions of normal S1 and S2 heart sounds [95]. Indeed, alternating cardiac activities are highlighted by the same gray tone colour within Table III.1. The S1 and S2 heart sounds occupies the same regions within the time–frequency plane but with changed intensities for auscultation area within the same cardiac cavities.

It should be noticed that heart valves are sharing cardiac cavities within the myocardium affects considerably the generated frequencies. Thus, Within the right

| | S1 | S2 |
|---|---|---|
| Aortic | M 25 Hz | S 25 Hz |
| | | M 90 Hz |
| | | M 120 Hz |
| Pulmonic | from 20 to 70 Hz | |
| | M 40 Hz | — |
| Mitral | M 25 Hz | |
| | S 50 Hz | VW 25 Hz |
| | M 90 Hz | |
| Tricuspid | S 25 Hz | M 40 Hz |
| | M 60 Hz | M 70 Hz |
| | S 120 Hz | S 100 Hz |

S: strong
M: medium
VW: very weak

Table III.1: Spectral content of S1 and S2 with regard to auscultation areas.

ventricle the pulmonic and the tricuspid valves interactively vibrate which yield this frequency alternating sounds, and vice versa for the aortic and the mitral valves which share the left ventricle. Indeed, we reexamine Table III.1 by highlighting the shared frequencies between tricuspid and pulmonic valves, also between mitral and aortic valves. Indeed, the 40 Hz component is present for only pulmonic and tricuspid auscultation areas. Concerning the mitral and aortic valves, it can be evidently confirmed that the 25 Hz and the 90 Hz spectral components are both present. The spectral content around 25 Hz should represent the aortic heart valve closing and is also strongly present at the S2 heart sound when acquired from the aortic area.

### SPWVD of abnormal heart sounds

Aortic stenosis heart sounds, which are mainly characterised by a systolic ejection murmur and a reduced or absent second heart sound, are analysed for comparison purposes. Hence, additional murmurs and changes upon heart sounds within the PCG signal can be well characterised in the time–frequency plane. An example of the recorded PCG signals of a subject with an aortic stenosis is illustrated in Figure III.8.

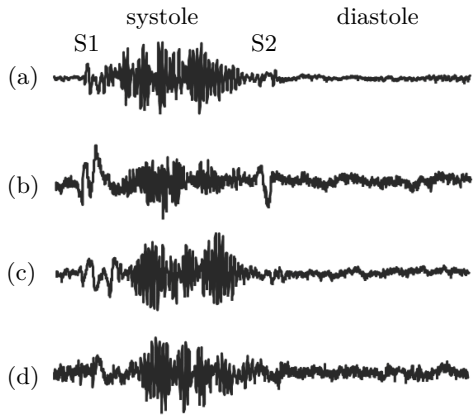


Figure III.8: Phonocardiogram signals (one cardiac cycle) of an abnormal subject (aortic stenosis) recorded from the (a) aortic, (b) tricuspid, (c) mitral and (d) pulmonic auscultation areas.

As illustrated in Figure III.8, the aortic and pulmonic components of S2 in aortic stenosis phonocardiograms are attenuated in comparison to S1. The whole systole is covered by a strong diamond–shaped systolic murmur. This murmur is correlated with the turbulent blood flow around the aortic orifice. The S1 heart sound is loudest at the tricuspid (Figure III.8(b)) and mitral (Figure III.8(c)) auscultation areas, which generates its main valvular components; namely T1 and M1, respectively.

Similarly to the normal case, only the tricuspid auscultation area allows us to record strongest S1 and S2 heart sounds, but at displaced frequencies. Indeed, the first heart sound S1 can be localised below 60 Hz when recorded from the tricuspid auscultation area, and still weaker for other recordings. On the other hand, for the same auscultation area, weaker second heart sound S2 can be perceived at frequencies lower than 60 Hz. Indeed, as shown in Figure III.9(b), the first heart sound S1 contains two separated bursts at 20 and 50 Hz. Furthermore, the second heart sound S2 losses its high frequency content and conserves a burst around 30 Hz. This should be the consequence of the stricture of the aortic valve and to the intracardiac pressure due to regurgitated blood. The attenuation of S1 and S2 heart sounds is confirmed to be one of the main characteristics of aortic stenosis lesion. Moreover, the systolic ejection of blood through the stenosed aortic orifice begets a systolic murmur clearly delimited in the time–frequency plane. Indeed, this murmur conserves its energy for all auscultation areas but with different shapes and at displaced frequencies. However, the systolic murmur within the aortic stenosis PCG signal is mainly characterised by two frequency modulation laws, at respectively 150 Hz and 180 Hz, which appear with different shapes for every auscultation area upon the chest. Another burst appearing between 0.6 sec. and 0.8 sec. in the time domain and lower than 20 Hz for the frequency domain (Figure III.9(b)), within the time–frequency plane could be a third heart sound S3. The third heart sound is un-

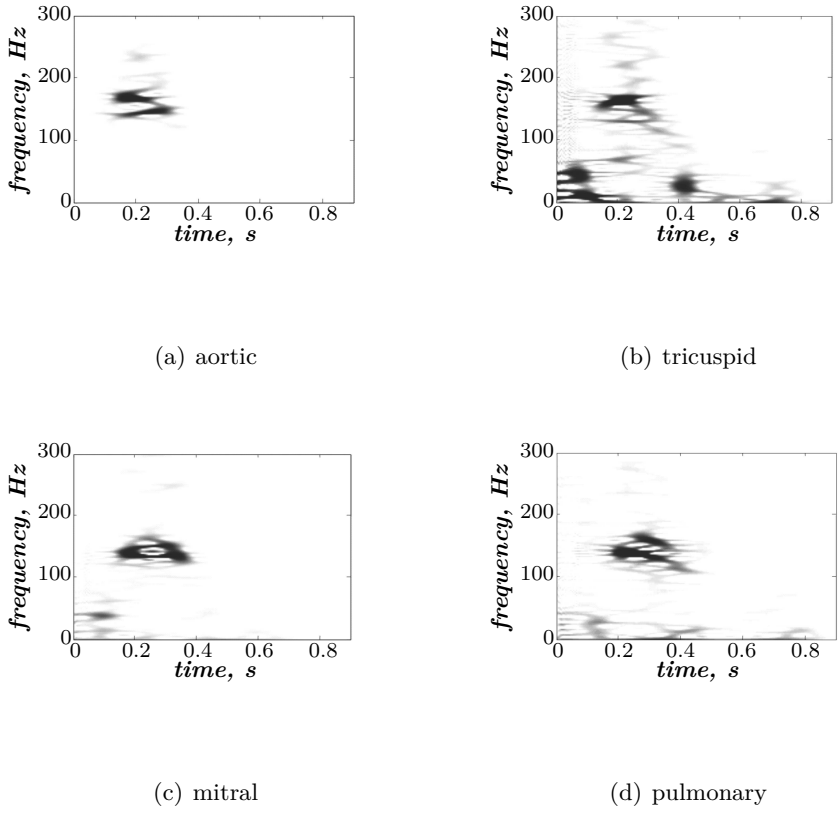


(a) aortic

(b) tricuspid

(c) mitral

(d) pulmonary

Figure III.9: SPWVDs of abnormal (aortic stenosis) PCG signal of Figure III.8: (a) aortic, (b) tricuspid, (c) mitral and (d) pulmonary auscultation areas.

common for patients with aortic stenosis disease but usually indicate the presence of systolic dysfunction and elevated filling pressure [96, 97].

### III.3.2 Reassigned–SPWVD applied to PCG signals

The PCG signal depicted in Figure III.10(a) was recorded by the data acquisition system *developed* by the author (Figure III.1). This signal is downsampled from 6 $kHz$ to 1 $kHz$ to lighten the computational load. Therefore, the signal bandwidth is then viewed up to 500 $Hz$ which covers adequately the heart sounds and murmurs spectral content.

As illustrated in Figure III.10(b), the spectral content of the PCG signal of Figure III.10(a) is concentrated below 150 $Hz$. This periodogram PSD is calculated by taking the modulus squared of the discrete Fourier transform (DFT) calculated by means of a fast Fourier transform (FFT) algorithm. Spectral analysis previews the frequency bandwidth of the PCG signal to be analysed.

Figure III.11 illustrates the WVD of the same PCG signal (Figure III.10(a)). The

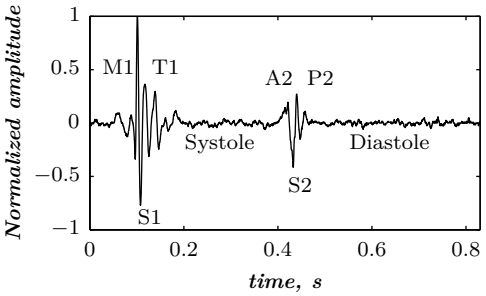


(a) Normal S1 and S2 heart sounds (tricuspid area)

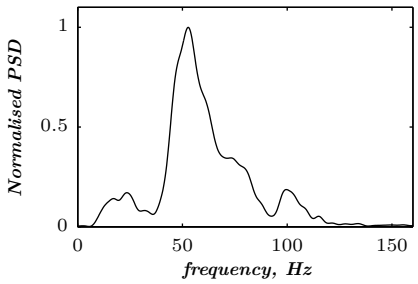


(b) Periodogram–based PSD of the PCG signal of Figure (a).

Figure III.10: (a) Normal PCG signal (recorded by the developed DAQ system illustrated in Figure III.1) and its (b) power spectral density.

main drawback within this TFR is cross–terms appearing at the midpoint between the S1 and the S2 heart sounds. The PSD of Figure III.10(b) is very useful in discussing the TFR of Figure III.11. Indeed, the WVD illustrated within Figure III.11 detects an interesting feature of cross–terms. As illustrated in Figure III.10(b), the main energy of the analysed PCG signal appears between 50 $Hz$ and 100 $Hz$. The WVD of Figure III.11 presents then another unwanted content below 50 $Hz$. This is the negative frequencies interference that affect the WVD of Figure III.11. We can correct this effect by using the analytic signal (see section II.1.1 on page 66) [98] of the PCG signal rather than the original signal. Figure III.12 illustrates the WVD of the analytic signal of the PCG of Figure III.10(a).

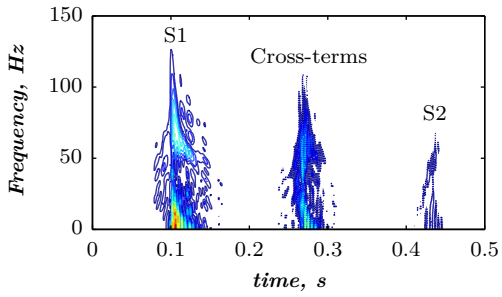


Figure III.11: WVD of the PCG signal of Figure III.10(a).

Figure III.12 show the correct content of the S1 and S2 heart sounds. However, cross–terms are still blurring the obtained TFR.

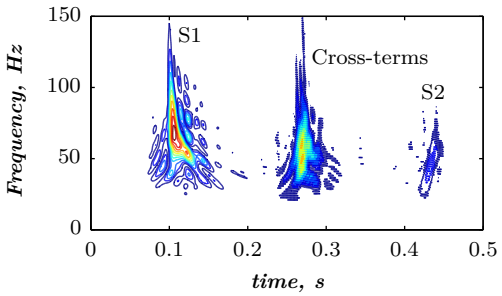


Figure III.12: WVD of the analytic signal of the PCG of Figure III.10(a).

As shown in Figure III.13, the SPWVD efficiently reduces cross–terms. Unfortunately, energy bursts of both S1 and S2 heart sounds within the time–frequency plane are spread out. To adjust these energy regions around their original chirp frequency modulated laws, we apply a reassignment operation to get a RSPWVD as illustrated in Figure III.14. This TFR is improved in terms of time and frequency resolutions. We zoomed the obtained TFR around the S1 heart sound to allow convenient viewing of the S1 heart sound chirp.

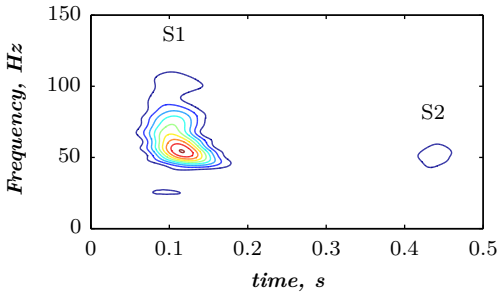


Figure III.13: SPWVD of the PCG signal of Figure III.10(a).

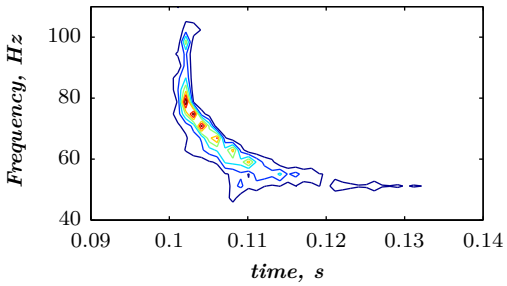


Figure III.14: RSPWVD of the S1 heart sound of the PCG signal of Figure III.10(a).

Since the recording is carried out at the tricuspid auscultation area, we get a weak S2 heart sound. The S1 heart sound content is clearly represented within the TFR of Figure III.14.

In order to better understand this chirp law, we move the microphone towards the mitral auscultation area to record another S1 heart sound as illustrated in Figure III.15. Then, the RSPWVD of Figure III.16 make the S1 heart sound more

clear. The chirp appearing in Figure III.14 starting from 100 $Hz$ and decreasing to 50 $Hz$ is still present within Figure III.16.

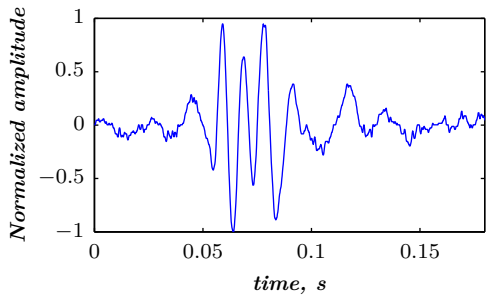


Figure III.15: Normal S1 heart sound recorded from the mitral auscultation area (CHUT).

An interesting energy region appears within Figure III.16 as the mitral activity below the arrow which is localised around 0.072 $s$. The TFR region around this arrow represent the overlapping between the two chirps of the mitral (M1) and tricuspid (T1) valves activities.

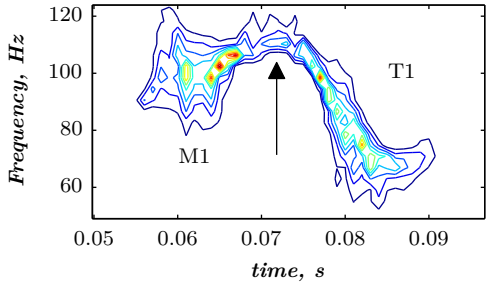


Figure III.16: RSPWVD of the S1 heart sound of Figure III.15.

The RSPWVD is a powerful tool which provides a concise time–frequency analysis of heart sounds. Indeed, Figures III.14 and III.16 highlight the modulated frequency chirp behaviour of heart sounds, and confirm the findings of Xu *et al.* [88, 89]. However, energies at the beginning and the end of the analysed heart sound cannot be well represented. This is due the amplitude attenuation issue to be resolved in next sections.

### III.3.3 Detection of the valvular split using the RSPWVD

The split within the S1 and S2 heart sounds emerged as an indicator of several valvular diseases alongside the Doppler echocardiography (DE). However, the DE is inaccurate in approximately 50% of patients of normal pulmonary artery pressure (PAP), 10–20% of patients with increased PAS, and 34–76% of patients with chronic obstructive pulmonary disease, a weak Doppler signal or a poor signal to noise ratio (SNR) [99]. Indeed, Fisher *et al.* [100] studied the accuracy of the DE in hemodynamic assessment of the pulmonary hypertension (PH). They demonstrated that DE can usually overestimate and underestimate the PAP in PH patients. This

can be partly explained by inaccuracies of the right atrial pressure estimation as well as poor Doppler imaging of the transtricuspid regurgitant blood flow. Moreover, Rich *et al.* [101] compared the Doppler echocardiography (DE) with the right sided heart catheterisation (RHC) as an invasive measure of the PAP in 160 patients with PH. They found out that the DE is inaccurate in estimating the PAP in 50.6 % of patients at a bias of 8.0 mmHg. Therefore, the DE–based estimation of the PAP is not reliable to diagnose the PH or to assess the efficacy of therapy.

In contrast, the split duration as well as the dominant frequency of P2 are increased in pulmonary hypertension and are considered as reliable parameters to estimate the PAP. Xu *et al.* [99] found that the duration between the onsets of the aortic (A2) and pulmonary (P2) components within the S2 heart sound (S2) allow accurate measurement of the PAP through advanced digital signal processing techniques. However, this split duration is limited (<100 ms) and still difficult to measure since these components are often overlapping and are of frequency modulated chirp behaviour [88, 89]. The separation of the valvular components of both S1 and S2 heart sounds remains a problematic issue. Indeed, several studies reported the complexity of analysing such transient signals formed by overlapping chirps [9, 102]. Xu *et al.* proposed a nonlinear transient chirp model to simulate A2 and P2 components of the S2 heart sound [88]. They also proposed a dechirping approach using the Wigner–Ville distribution (WVD) to estimate the instantaneous frequency (IF) of the aortic (A2) and the pulmonary (P2) components. However, they reported weak energies at the beginning and the end of each chirp component to recover the frequency modulated behaviour of heart sounds in the time–frequency plane. This is due to the weak amplitude of all valvular heart sound chirps at their onsets and their ends [88].

The A2–P2 valvular split can be originated under physiological or pathological conditions. In normal subjects, a physiological split of the S2 heart sound can occur during inspiration as a result of the delayed pulmonary pressure to raise over the right intraventricular pressure which closes the pulmonary valve. Cardiac pathologies such as the right bundle branch block and the pulmonary stenosis may induce a wide S2 split [103, 104].

The *developed* algorithm overcame amplitude attenuation by accurately detecting the valvular split within simulated and real S2 heart sounds [105]. Firstly, the onset and the end amplitude of each valvular component is recovered by an envelope recovery procedure developed within this work. Secondly, the IF of simulated heart sounds is reconstructed at a higher time–frequency resolution by the Reassigned smoothed Wigner–Ville distribution (RSPWVD). The time–frequency content is recovered at several valvular split durations (from 30 to 60 ms at a step of 10 ms). Subsequently, real S2 heart sounds of the LGB–IRCM cardiac valve database are processed to validate the algorithm in real conditions. Moreover, the algorithm can be applied to detect the valvular between M1 and T1 in S1 heart sounds.

### III.3.4 Valvular heart sound model

Tran *et al.* [106] developed a heart sound simulator by combining a set of equations to model several phonocardiogram behaviours. This model is formed by a linear chirp with an amplitude adjusted according to clinically recorded S1 and S2 heart sounds. Xu *et al.* [88, 89] extended this model to a narrow–band non–linear chirp signal with a fast decreasing IF over the time–frequency plane to model the valvular heart sound. This decreasing frequency behaviour is generated by the decaying aortic and pulmonary pressures after the end of systole and during the beginning of early diastole. The modulated frequency content of the valvular sound is of chirp nature rather than linear. Indeed, in previous works, we confirmed that heart sounds are narrow–band non–linear chirp signals [3, 91].

Xu *et al.* discussed the exponentially damped sinusoid model [107, 108], the matching pursuit method [109, 110], and the linear chirp model as modelling approaches of heart sounds. They found out that the transient nonlinear chirp signal they proposed is the suitable model for the analysis–synthesis of the valvular heart sounds.

We used the model proposed by Xu *et al.* [88, 89] to generate simulated valvular sounds to study the performance of the detection algorithm *developed* within this work. The valvular non–linear chirp model is defined by an amplitude and a phase functions according to (III.1) as follows:

$$v(t) = a(t)\sin\left(\varphi(t)\right) \tag{III.1}$$

where $a(t)$ and $\varphi(t)$ represent the IF and phase of the valvular sound, respectively.

The highest and the lowest frequencies of the chirp model differ from each valvular sound to another. However, the valvular model is valid for the overall valvular components of both the S1 and the S2 heart sounds. According to (III.1), Figure III.17 illustrates the A2 and P2 valvular sounds. The A2 chirp begin from 250 Hz and falls to 53 Hz at 60 ms whilst the P2 chirp goes from 200 to 50 Hz [88, 89, 111]. The A2 and P2 components last usually 30 up to 60 ms but less than 80 ms [89, 88]. The split duration between them rises during inspiration to reach 30 up to 80 ms, and decreases under 15 ms during expiration [112, 113].

According to the valvular model in (III.1), the S2 heart sound is given by;

$$S_2(t) = a_{A2}(t)\sin\left(\varphi_{A2}(t)\right) + a_{P2}(t-d_s)\sin\left(\varphi_{P2}(t-d_s)\right) \tag{III.2}$$

where $\Big(a_{A2}(t), \varphi_{A2}(t)\Big)$ and $\Big(a_{P2}(t), \varphi_{P2}(t)\Big)$ denote the amplitude and phase of the A2 and P2 valvular sounds respectively. The split duration interval denoted by $d_s$ separates the beginning of A2 and P2 components. The simulated valvular non–linear chirp component duration is set to 60 ms [88].

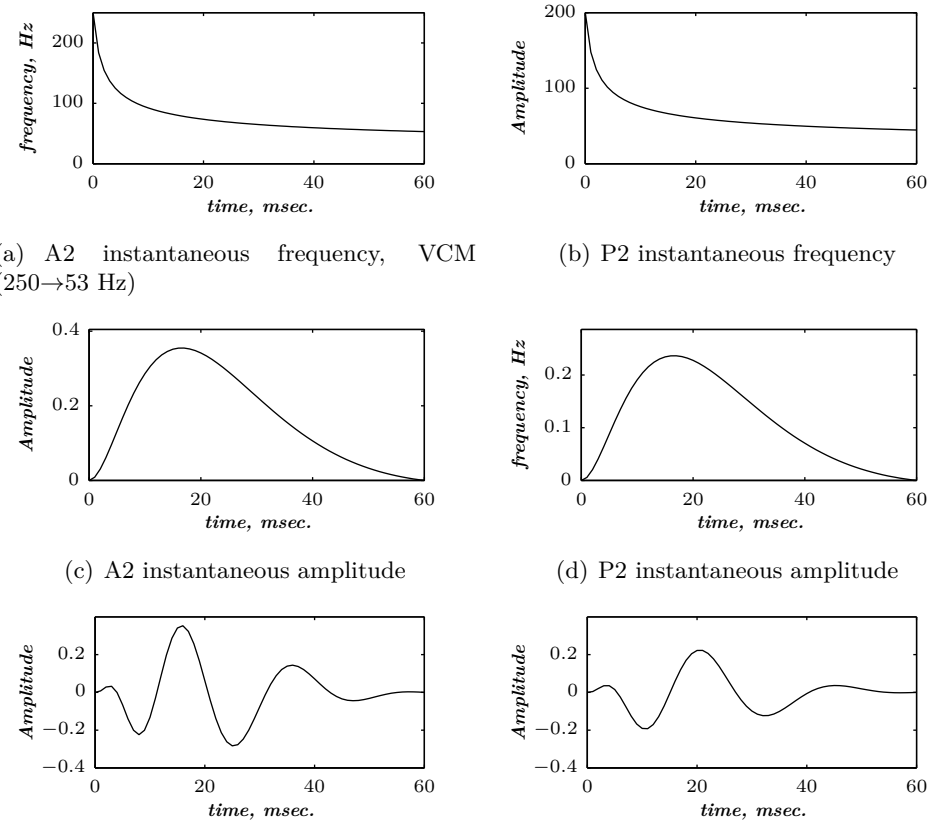


(a) A2 instantaneous frequency, VCM (250→53 Hz)

(b) P2 instantaneous frequency

(c) A2 instantaneous amplitude

(d) P2 instantaneous amplitude

(e) Simulated A2.

(f) Simulated P2.

Figure III.17: Heart sound modelling: (a) Instantaneous frequency and instantaneous amplitude (c) of A2 valvular component, (b) Instantaneous frequency and instantaneous amplitude (d) of P2 valvular component, simulated (e) A2 and (f) P2 valvular components.

### III.3.5 Detection algorithm of the A2–P2 valvular split

Xu *et al.* demonstrated that heart sounds are formed by overlapping chirp components which are generated by the closures of the intracardiac valves [88, 89]. Unfortunately, the restrictive weak amplitude at the onset and the end of each chirp component confined the time–frequency chirp shape of each component at its highest amplitude domain [88].

The *developed* algorithm sorts out this downside by recovering these weak amplitude areas through an envelope recovery of the analysed signal. This is the first step of the algorithm which paves the way to make up the full content of heart sounds in the time–frequency plane. The developed detection algorithm of the valvular split within heart sounds is summarised as follows;

1. Envelope recovery: the signal is consecutively multiplied with its complement

to 1 until the correlation between the latest consecutive signals exceeds 99.90%.

2. Calculation of the Reassigned–SPWVD of the signal.

3. Detecting frequencies of the RSPWVD coefficients with highest intensities over the time domain.

4. Processing the obtained time–frequency representation as unidimensional curve to detect the split inflection by localising the maximum and the minimum having the maximum amplitude difference.

We propose a detection approach of the A2–P2 valvular split based on the calculation of the Hilbert transform envelope of the S2 heart sound. This optional step is used for comparison purposes with the developed RSPWVD–based algorithm and is summarised as follows;

1. Calculation of the envelope of the signal by the Hilbert transform which is given by (III.3) [58];

$$\begin{aligned} H\{x(t)\} &= x(t) * \frac{1}{\pi t} \\ &= \frac{1}{\pi}\text{p.v.}\left\{\int \frac{x(\tau)}{t-\tau}\mathrm{d}\tau\right\} \end{aligned} \tag{III.3}$$

   where p.v. $\{.\}$ denotes the Cauchy principal value.

2. Detection of the split by localising the midway local minimum of the envelope at the higher amplitude.

The discrete instantaneous frequency (IF) is calculated as the inverse of the detected periods of heart sounds through the time domain. This detection is carried out by localising time–instants of zero–crossings of the analysed heart sounds. This discrete IF sequence enables to back up the discussion of the final IF detected from the RSPWVD.

### Detection of the A2–P2 valvular split in simulated heart sounds

The simulated data are generated by the valvular heart sound model presented in section III.3.4 [88, 89]. According to (III.2), Figure III.18(a) illustrates a simulated S2 heart sound with an A2–P2 split duration of 30 ms. The IF of the simulated S2 heart sound is illustrated in Figure III.18(b). The simulated S2 heart sounds at various valvular split durations (30, 40, 50 and 60 ms) are processed. Figure III.18(c) shows the IF of the simulated S2 heart sound of Figure III.18(a) with a A2–P2 split of 30 ms. This IF is the average of the IFs (Figure III.18(b)) of the A2 and P2 components which form the S2 heart sound (Figure III.18(a)).

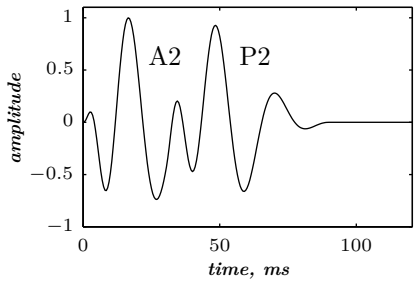


(a) Simulated S2 heart sound, A2–P2 valvular split: 30 ms

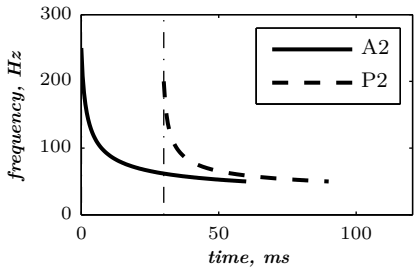


(b) Instantaneous frequency of the simulated A2 (duration: 60ms, frequency:250→53 Hz) and P2 (duration: 60 ms, frequency: 200→50 Hz) components of the S2 heart sound, A2–P2 valvular split: 30 ms

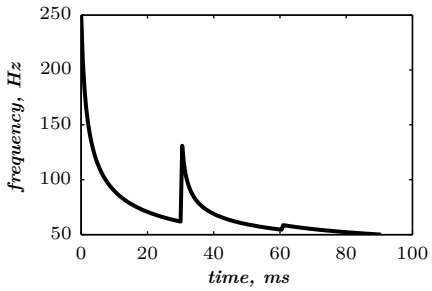


(c) Instantaneous frequency of the S2 heart sound, calculated from the IFs of the A2 and P2 valvular components of Figure III.18(b)

Figure III.18: Simulated S2 heart sound (duration: 90 ms, A2–P2 valvular split: 30 ms)

The discrete IF estimated by detecting the zero–crossings of S2 is illustrated in Figure III.19. Both IFs show the inflection related to the valvular split around 30 ms at a high correlation level. The A2–P2 split is represented as a rapid transient during the merging interval between the aortic and the pulmonary chirp components within the time–frequency plane. As depicted in Figure III.18(c), it should be noticed that the split occurs approximately between 50 and 150 Hz. The decreasing frequency of both the A2 and the P2 valvular components are adequately confirmed by the discrete IF illustrated in Figure III.19.

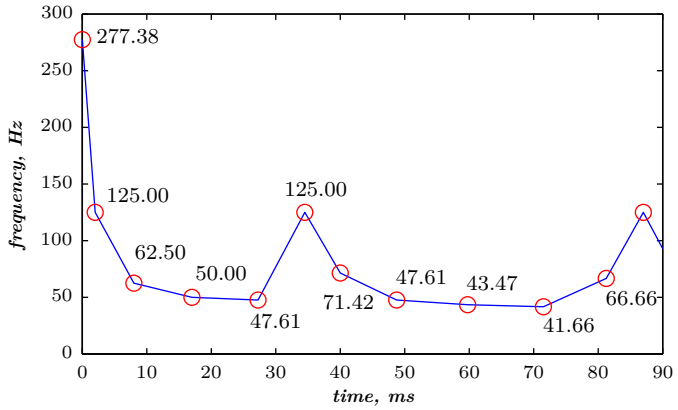


Figure III.19: Discrete IF of the envelope recovered S2 heart sound of Figure III.20

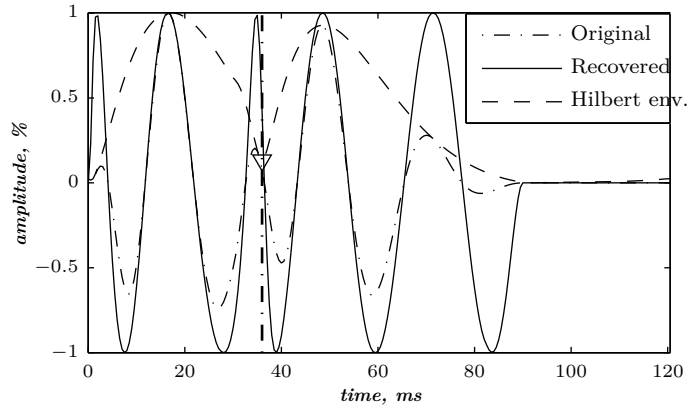


Figure III.20: Envelope recovered S2 heart sound (detected A2–P2 valvular split: 36 ms).

To deal with the amplitude weakness of the valvular sounds encountered by Xu *et al.* [88] during time–frequency analysis of heart sounds, we calculated another version of heart sounds which we call the envelope recovered heart sound as presented in section III.3.5. Figure III.20 illustrates the envelope recovered heart sound of Figure III.18(a). This adjusted sound benefits of the same amplitude for its entire time support.

The Hilbert envelope detection approach retraces the instantaneous power of this S2 heart sound and shows an amplitude variation which is related to the A2–P2 split. This split is localised at 36 ms from the onset of the A2 valvular component at an error of 6 ms from the original split (30 ms).

The recovery of the heart sound is carried out until reaching a cross–correlation between consecutive steps of 99.90 % as presented in section III.3.5. This procedure of the A2–P2 split detection algorithm is not CPU time consuming and still a vital step for the time–frequency analysis. It should be noticed that 8 iterations are sufficient to reach the desired cross–correlation rate for this simulated S2 heart sound.

As illustrated in Figure III.21, the WVD of the S2 heart sound of Figure III.18(a) is blurred by cross–terms. Moreover, the weakness of the A2 and P2 components at their onsets and their ends affects their respective time–frequency coefficients. Indeed, These components appears at their middle rather than the entire durations of each components.

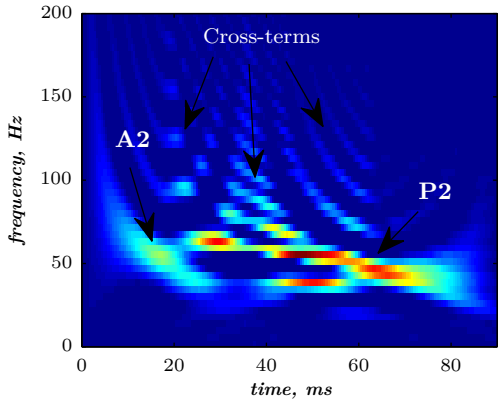


Figure III.21: WVD of the S2 heart sound of Figure III.18(a).

In contrast, the RSPWVD provides an reliable time–frequency representation which retraces perfectly the IF of the S2 heart sound. Indeed, as illustrated in Figure III.22, the RSPWVD of the envelope recovered S2 heart sound of Figure III.20 is highly correlated with the original IF of Figure III.18(c) as well as the discrete IF of Figure III.19. This reassigned distribution recovered the A2–P2 split around 30 ms and between 50 and 150 Hz as previously defined during the synthesis of the S2 heart sound (Figure III.18(a)).

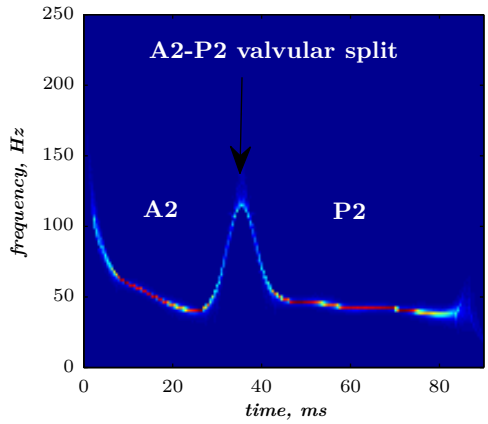


Figure III.22: RSPWVD of the S2 heart sound of Figure III.20.

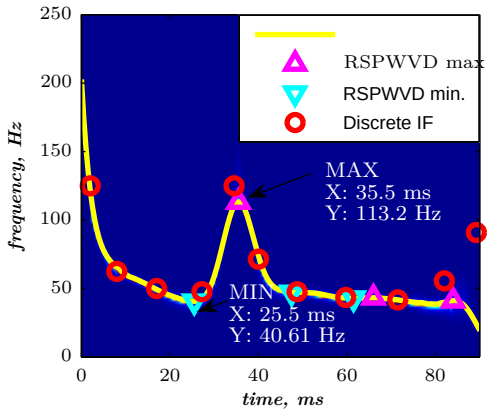


Figure III.23: Ridges (yellow line) of the RSPWVD of III.22 (detected A2–P2 valvular split: $\frac{25.5+35.5}{2} = 30.5$ ms).

In Figure III.23, the discrete IF of Figure III.19 is represented with local extrema of the inflection zone within the RSPWVD. It should be noticed that the obtained RSPWVD retraces perfectly this discrete IF in the effective duration of the analysed S2 heart sound. Moreover, we detected the maximum intensity coefficients of the RSPWVD of Figure III.23 to yield the IF of the analysed S2 heart sound. We also detected local maxima and minima of this curve to give an estimation of the A2–P2 valvular split by averaging time instants of the maximum and the minimum points at the inflection zone of the detected IF. According to this estimation approach, we found 30.5 ms as an A2–P2 valvular split in the RSPWVD of Figure III.23.

The RSPWVD detection method is based on the variation of the IF of the S2 heart sound within the time–frequency plane rather than following variations in the amplitude of the signal as carried out by the Hilbert envelope detection approach. Therefore, the RSPWVD–based A2–P2 detection is accurate and improves the detection in comparison to the Hilbert envelope approach.

As depicted in Table III.2, we extended the processing to various A2–P2 valvular split durations (30, 40, 50, and 60 ms). The A2–P2 split measurements summarised in Table III.2 confirms the ability of the RSPWVD–based method to detect the A2–P2 split. The RSPWVD of Figure III.24(c) and Figure III.25(c) continues to show the inflection behaviour at the A2–P2 split zone and provides 44 and 56.25 ms as measured values of the simulated split values of 40 and 60 ms.

### Detection of the A2–P2 valvular split in real S2 heart sounds of the LGB–IRCM cardiac valve database

Figure III.26 illustrates the PCG and ECG signals of a sample data file (10001.11) of the LGB–IRCM cardiac valve database. The PCG signal of this sample is recorded from the aortic auscultation area. The PCG signal is segmented in systole and diastole by detecting the peak of the R–wave and the end of the T–wave by an algorithm presented in [114] which uses both the amplitude and the curvature of

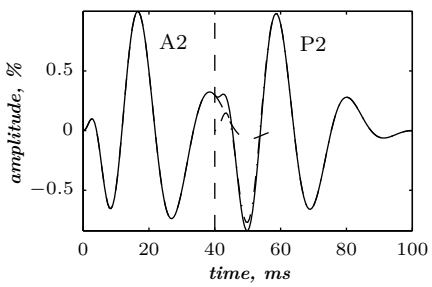


(a) Simulated S2 heart sound, A2–P2 valvular split: 40 ms

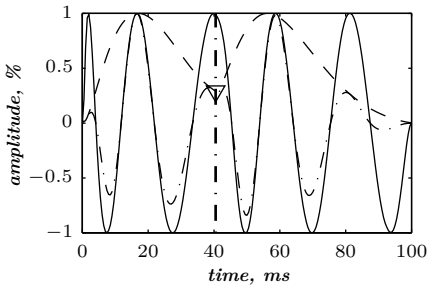


(b) Envelope recovered signal (solid line) of the S2 heart sound (dash–dot line) of Figure III.24(a) and its Hilbert transform envelope (dashed line)

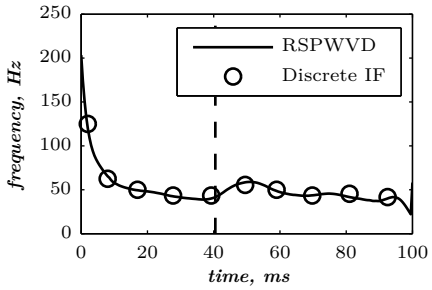


(c) RSPWVD of the envelope recovered S2 heart sound of (b)

Figure III.24: RSPWVD–based detection of the A2–P2 valvular split of the S2 heart sound (A2–P2 valvular split of 40 ms detected at 44 ms)

the ECG waves. This algorithm provides correct detection of the overall ECG–PCG signals of the LGB–IRCM cardiac valve database.

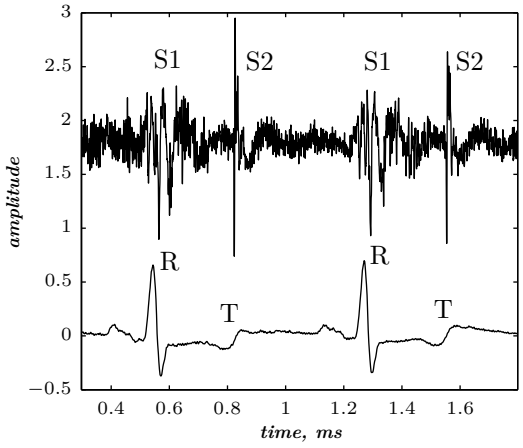


Figure III.26: Data file sample (10001.11) of the LGB–IRCM cardiac valve database: PCG and ECG signals over 2 cardiac cycles.

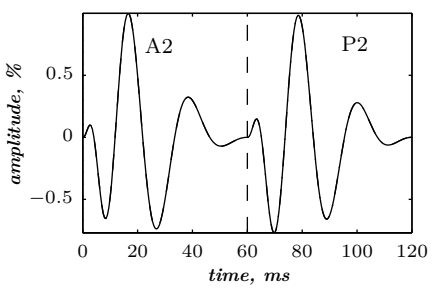


(a) Simulated S2 heart sound, A2–P2 valvular split: 60 ms

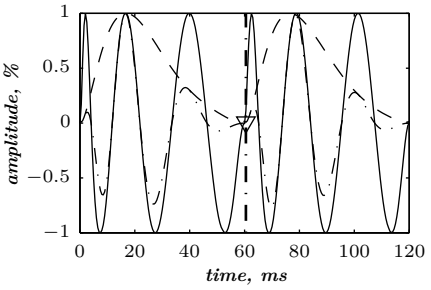


(b) Envelope recovered signal (solid line) of the S2 heart sound (dash–dot line) of Figure III.25(a) and its Hilbert transform envelope (dashed line)

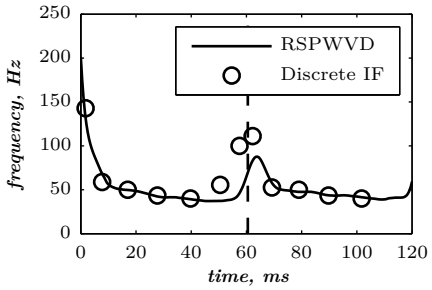


(c) RSPWVD of the envelope recovered S2 heart sound of (b)

Figure III.25: RSPWVD–based detection of the A2–P2 valvular split of the S2 heart sound (A2–P2 valvular split of 60 ms detected at 56.25 ms)

Figure III.27 illustrates the averaged S1 and S2 heart sounds of the PCG signal (LGB–IRCM data file: 10001.11 of Figure III.26). The main advantage behind averaging the PCG segments over the consecutive cardiac cycles is to fade the background noise to yield a smooth signal for the subsequent processing. The S2 heart sounds are adjusted according to their recurrent autocorrelation functions over the consecutive cardiac cycles. This adjustment resolves the jitter of the S2 heart sound within the diastole phase and keeps up the aortic and the pulmonary chirp components for the subsequent time–frequency analysis.

As depicted in Figure III.28(a) the S2 heart sound averaged in FigureIII.27(b) is formed by two chirps, namely the A2 and the P2 valvular components. The A2 chirp is of higher amplitude than that of the P2 component which confirms the recording carried out from the aortic auscultation area. The envelope recovered version of this S2 heart sound illustrated in FigureIII.28(b) obviously highlights the frequency modulated behaviour of the valvular sound.

The WVD of Figure III.29 of the averaged S2 heart sound of Figure III.28(a) is concentrated within the time support of the A2 valvular chirp which is of highest amplitude than that of the P2 component. The split behaviour we found in

Table III.2: The A2–P2 valvular split detected by the RSPWVD–based detection method.

| split (ms) | 30 | 40 | 50 | 60 |
|---|---|---|---|---|
| $A2–P2_{min}$ | 25.5 | 37 | 38.5 | 49 |
| $A2–P2_{max}$ | 35.5 | 51 | 52.5 | 63.5 |
| $A2–P2_{mean}$ | 30.5 | 44 | 45.5 | 56.25 |
| $A2–P2_{error}$ | +0.5 | +4 | +4.5 | -3.75 |

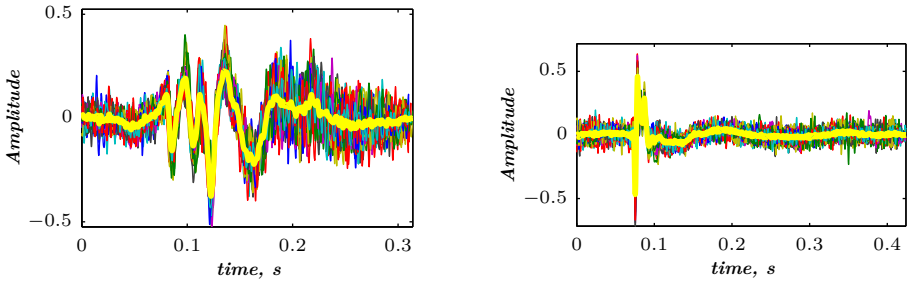


(a) Averaged & adjusted S1 (yellow line) over 40 systolic phases (coloured lines).

(b) Averaged & adjusted S2 (yellow line) over 40 diastolic phases (coloured lines).

Figure III.27: LGB–IRCM cardiac valve database (data file: 10001.11). Averaged & adjusted (a) S1 and (b) S2 heart sounds over 40 cardiac cycles.

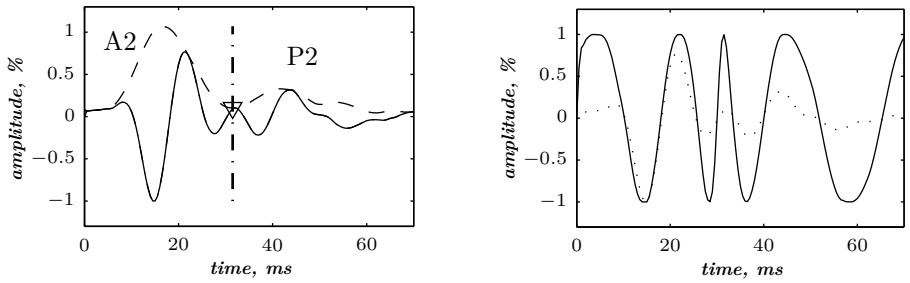


(a) Averaged S2 and its Hilbert transform envelope (dashed line)

(b) Envelope recovered S2 heart sound (solid line) of the S2 heart sound (dotted line) of Figure III.28(a)

Figure III.28: (a) Averaged S2 heart sound (over 40 cardiac cycles) and its (b) envelope recovered signal (LGB–IRCM cardiac valve database, data file: 10001.11).

section III.3.5 is not reproduced by the WVD. As demonstrated by Xu *et al.*, the weakness of the valvular sounds at their extremities restricts the energy bursts in the high amplitude time support of the analysed sounds within the time–frequency plane [88].

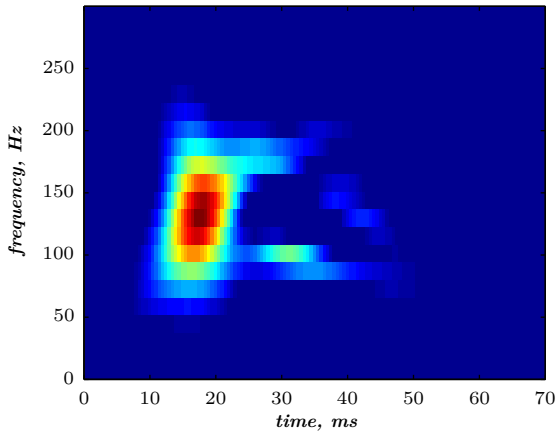


Figure III.29: WVD of the S2 heart sound of Figure III.28(b).

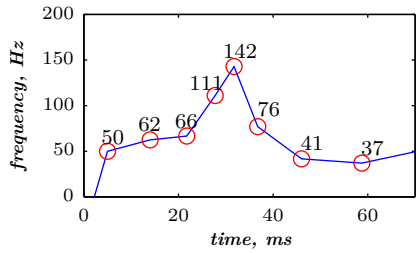


(a) Discrete IF of the envelope recovered S2 heart sound of Figure III.28(b)

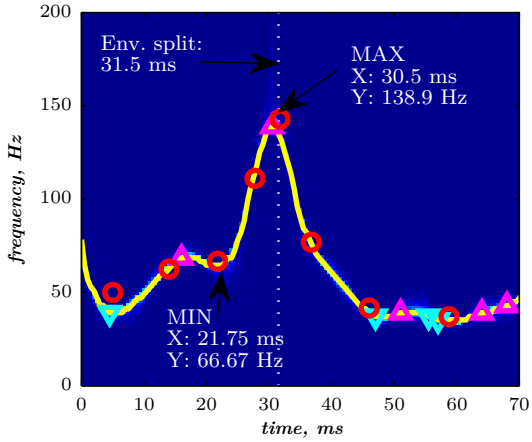


(b) RSPWVD of the envelope recovered S2 heart sound of Figure III.28(b) and the discrete IF of (a) (circles plot)

Figure III.30: (a) Discrete IF and (b) RSPWVD of the S2 heart sound of the 10001.11 data file of the LGB–IRCM cardiac valve database.

The RSPWVD of Figure III.30(b) adequately retraces the discrete IF of Fig-

ure III.30(a) which are calculated from the envelope recovered S2 heart sound of FigureIII.28(b). This RSPWVD resolved the A2–P2 valvular split of the real S2 heart sound at a high time and frequency resolutions. Indeed, the time–frequency representation illustrated in Figure III.30(b) yields a similar result in comparison to the simulations carried out in section III.3.5. The A2 and P2 valvular chirps are clearly reproduced at a high correlation with the simulated heart sounds as well as their split within the S2 heart sound. similarly, the valvular split in the real S2 heart sound is also localised between 50 and 150 Hz. As depicted in Figure III.30(b), if we take the average between the time instants of the maximum (30.5 ms) and the minimum (21.75 ms) frequencies during as an estimation of the A2–P2 valvular split, we obtain 26.125 ms which is confirmed by the discrete IF illustrated in Figure III.30(a).

### Heart sound dechirping algorithm

After noting the improvement established by the RSPWVD regarding the detection of the valvular split of S1 and S2, it is worthwhile to break down each sound into its forming valvular chirps. Therefore, the valvular heart sound model studied in section III.3.4 is put to use in order to dechirp S1 and S2 heart sounds into their elementary valvular components; *i.e.* S1 into M1 & T1, and S2 into A2 & P2.

According to results obtained in sections III.3.5 & III.3.5, S1 and S2 are formed by two overlapping frequency modulated decreasing hyperbolic chirps. To separate these valvular components, the RSPWVD of each heart sound is computed to detect the instantaneous frequency of S1 and S2. Subsequently, local extrema of the obtained instantaneous frequency are detected. A valvular chirp is then generated on the basis of the detected attack and decay frequencies of the first valvular chirp of each heart sound. An averaged duration of 60 ms is used to synthesise this dechirping valvular component. Thus, the synthesised valvular component is subtracted from the original heart sound to yield the second valvular chirp.

Various conclusive tests are carried out on simulated and real heart sounds to show the effectiveness of the **developed** dechirping technique despite phase cancellation between their forming valvular sounds.

### Dechirping simulated heart sounds

The RSPWVD illustrated in Figure III.23 is processed to detect the attack and decay frequencies of the first valvular chirp of the analysed S2 heart sound depicted in Figure III.18(a). By using the *developed* dechirping technique, the second component is separated from the whole S2 heart sound. Figure III.31 illustrates the dechirped A2 and P2 components.

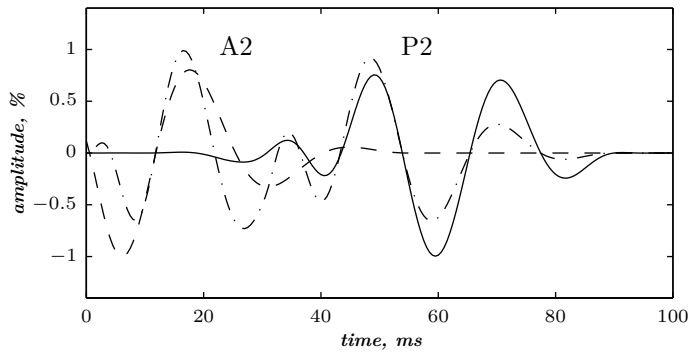


Figure III.31: Dechirped A2 (dashed line) and P2 (solid line) valvular chirps of S2 (dash–dot line) heart sound of Figure III.18(a).

As illustrated in Figure III.32, the RSPWVD of the separated P2 component retraces the same time–frequency content of the separated pulmonic valvular sound. The attack amplitude are weaker but gain intensity at the attack frequency of the separated chirp.

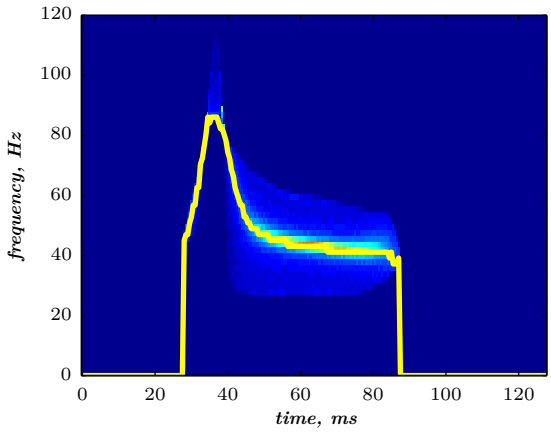


Figure III.32: RSPWVD of the separated P2 valvular chirp component of S2 of Figure III.18(a), and its instantaneous frequency (yellow line).

### Dechirping real heart sounds

Valvular sounds cancel each other out during transmission from the heart to the chest. Envelope–based detection methods are unsuitable for detecting valvular sounds because of phase cancellation between them. The *developed* algorithm recovers each valvular sound and confirms the obtained result through time–frequency representation of the separated sounds. Several real heart sounds of the LGB-IRCM database were processed by the *developed* dechirping technique. Data file 10009.11 has been selected to highlight the phase cancellation issue during separation.

As illustrated in Figures III.33(a)&III.33(c), the averaged S1 heart sound and its adjusted version do not show any noticeable improvement. However, the averaged

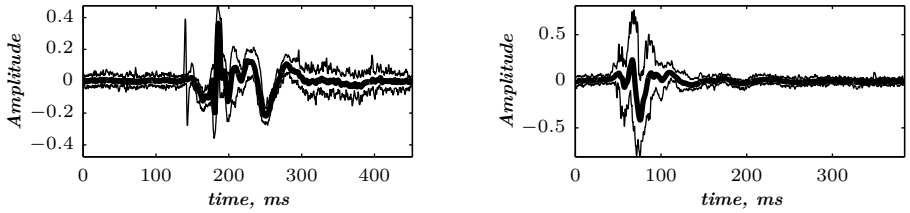


(a) Averaged S1




(b) Averaged S2

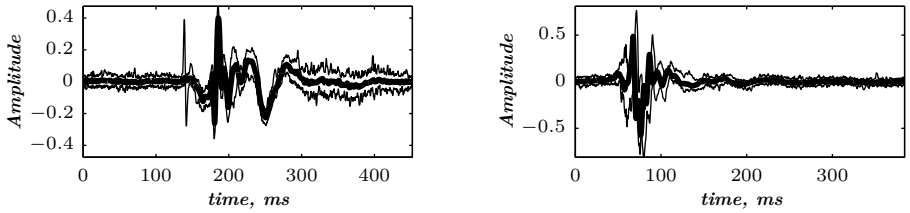


(c) Averaged & adjusted S1




(d) Averaged & adjusted S2

Figure III.33: (a)&(b) Non–adjusted and &(c)&(d) adjusted averaging of S1 and S2 heart sounds (LGB–IRCM cardiac valve database: 10078.11, aortic stenosis: light).

S2 heart sound and its adjusted version, illustrated in Figures III.33(b)&III.33(d), confirms again the impact of adjustment on the jitter behaviour of the S2 heart sound.

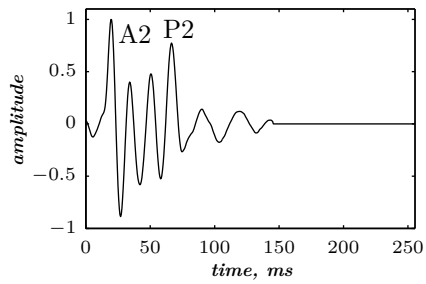


(a) Averaged & adjusted S2, LGB–IRCM datafile: 10009.11

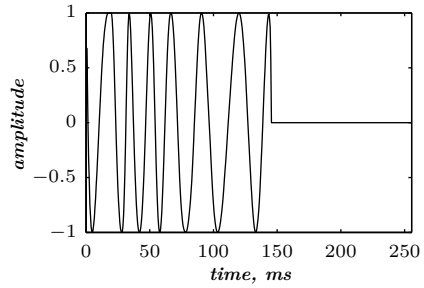


(b) Envelope recovered S2, LGB–IRCM datafile: 10009.11

Figure III.34: (a) Adjusted and (b) envelope recovered S2 heart sound (LGB–IRCM cardiac valve database: 10009.11).

The averaged and adjusted S2 heart sound of Figure III.33(d), also zoomed in Figure III.34(a) is considered for processing. Its envelope recovered version is illustrated in Figure III.34(b) (section III.3.5).

The time–frequency content detected by RSPWVD illustrated in Figure III.35(b) as expected reflects the inflection in relation to overlapping between valvular heart sounds A2 and P2. In Figure III.35(a), local minimum of the envelope is detected at 34 ms. However, this value cannot be considered as the exact valvular split between

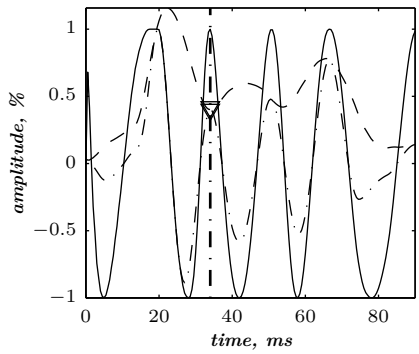


(a) Second heart sound of Figure III.34(a) (dash–dot line), its envelope (dashed line), and its envelope recovered version (solid line), LGB–IRCM datafile: 10009.11

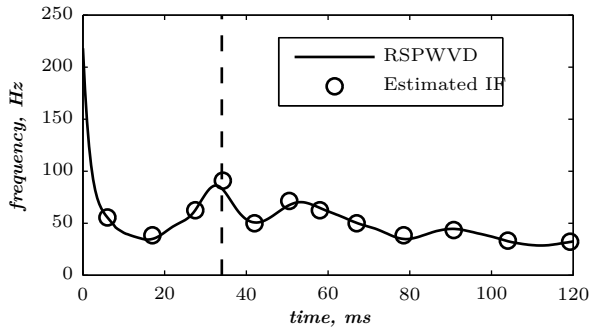


(b) RSPWVD of the envelope recovered S2 heart sound of Figure III.34(b)

Figure III.35: ((a)) Adjusted S2 heart sound of Figure III.34(a) and its (b) RSPWVD (LGB–IRCM cardiac valve database: 10009.11).

A2 and P2 since the inflection waverform lasts beyond 34 ms.

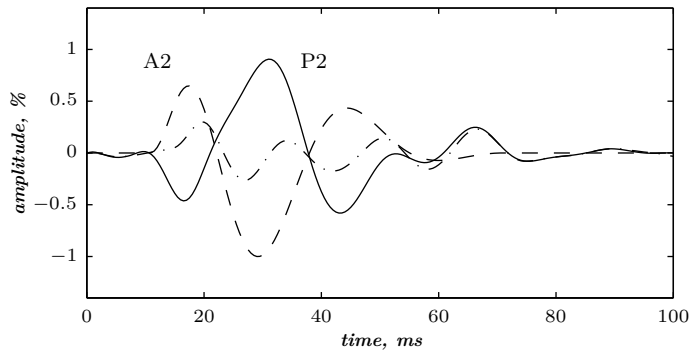


Figure III.36: Dechirped A2 (dashed line) and P2 (solid line) valvular sounds of the avereaged & adjusted S2 heart sound (dash–dot line) of the LGB–IRCM datafile: 10009.11.

By processing the RSPWVD of Figure III.35(b) by the *developed* dechirping algorithm, the A2 and P2 valvular sounds are detected and separated each one from the other. This finding can be very useful in estimating the status of each intracardiac valve by combining a biomechanical hemodynamic study with the valvular sounds detection algorithm within the time–frequency plane.

### III.3.6 Time–frequency detection of heart murmurs

Envelope detection methods in the time domain became unusable in severe or combined valvular pathologies. Therefore, heart murmurs were detected by averaging time–frequency representations of systole and diastole phases over the segmented cardiac cycles.

Murmurs within phonocardiographic signals are related to stenosis or regurgitation through abnormal valves during the cardiac cycle. Intensity of murmurs are related to the severity of the cardiovascular pathology. As previously shown in Figure III.27(b), murmurs are filtered during averaging PCG signals through cardiac cycles. In this section, a detection method of heart murmurs within the time–frequency plane is presented. For this purpose, the PCG&ECG data file 10078 which is recorded from a patient with a light aortic stenosis from the LGB–IRCM cardiac valve database is selected to study the behaviour of its systolic murmur.

Averaged but non–adjusted systole and diastole heart sounds of this record are illustrated in Figures III.37(a) & III.37(b). These phases are adjusted through cross–correlation to avoid loosing acoustic waves during averaging PCG cardiac cycles. The averaged and adjusted heart sounds through cross–correlation are depicted in Figures III.37(c) & III.37(d). The upper and lower envelopes represent the maximum amplitude values of the PCG signal over systole and diastole phases. The middle PCG signal represented within these non–adjusted and adjusted heart sounds is the average signal for each case.

By comparing S1 heart sounds in Figures III.37(a)&(c), and S2 heart sounds in Figures III.37(b) & III.37(d), it became obvious that adjusting heart sounds is

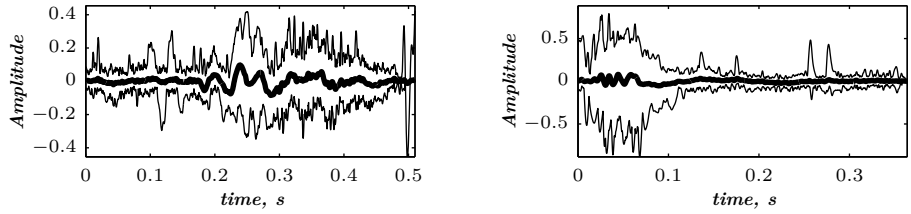


(a) Averaged S1 (b) Averaged S2

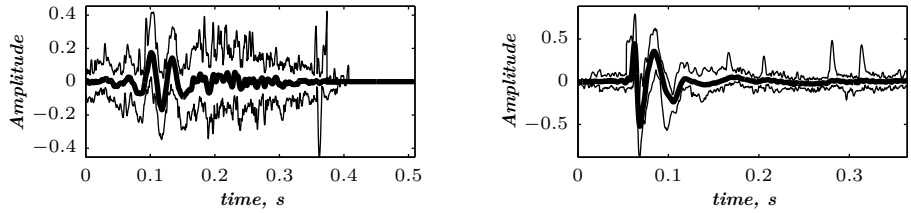


(c) Averaged & adjusted S1 (d) Averaged & adjusted S2

Figure III.37: Non–adjusted and adjusted averaging of S1 and S2 heart sounds, LGB–IRCM data file: 10078.11 (Aortic stenosis: light).

necessary to detect the recurrent waveforms through cardiac cycles. The systolic murmur resulting from blood flow going through the stenosed aortic valve is indeed filtered by averaging. This finding confirms the random nature of heart murmurs.

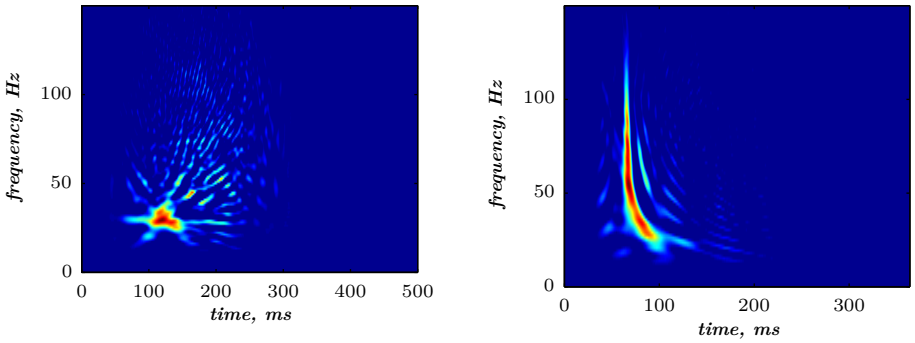


(a) WVD of the 1st systole phase (b) WVD of the $1^{st}$ diastole phase

Figure III.38: WVD of the 1st cardiac cycle of the 10078.11 data file (LGB–IRCM cardiac valve database)

The WVD is used to characterise the time–frequency content of the analysed signals. Figures III.38(a) & III.38(b) illustrates WVDs of systole and diastole phases of the first cardiac cycle considered as an example among the 35 segmented PCG representing each cardiac cycle of the 10078.11 data file. Both heart sounds and murmurs are represented in the time–frequency plane. The systolic heart murmur is fragmented over the systole phase in comparison to heart sounds. The S1 heart

sound is concentrated below 50Hz. The S2 heart sound covers a wide area within the time–frequency plane occurring as a chirp–like component.

Figure III.39(a) & III.39(a) illustrate WVDs of the averaged systole and diastole phases of the analysed PCG signal within data file 10078.11. No significant energy is observed neither in systole nor in diastole time–frequency representations. The S1 and S2 heart sounds emerged over the averaged cycles to a satisfactory energy level in the time–frequency plane in comparison to the filtered heart murmurs.

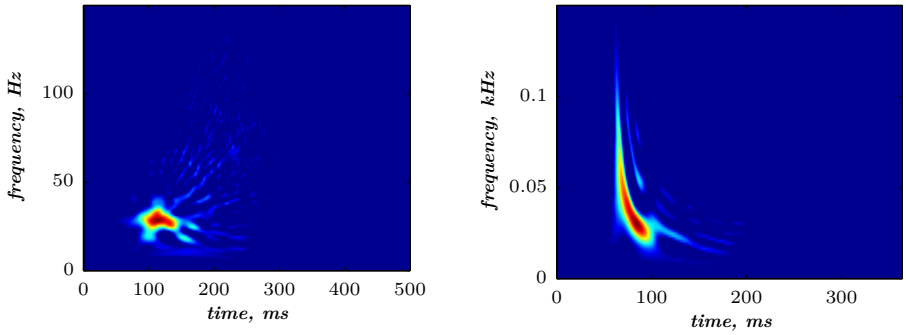


(a) Averaged WVD of systole phases (b) [Averaged WVD of diastole phases

Figure III.39: Averaged WVD of adjusted systole and diastole phases over 35 cardiac cycles (LGB–IRCM cardiac valve database: 10078.11)

Therefore, a technique has been **developed** to detect heart murmurs within the time–frequency plane. Firstly, the WVD of the adjusted and averaged PCG signal is computed. Secondly, the WVD of the PCG signal of each cardiac cycle is computed. Subsequently, the WVD of the averaged PCG signal is subtracted from the WVD of each segmented PCG signal to get a time–frequency representation of the heart murmur.

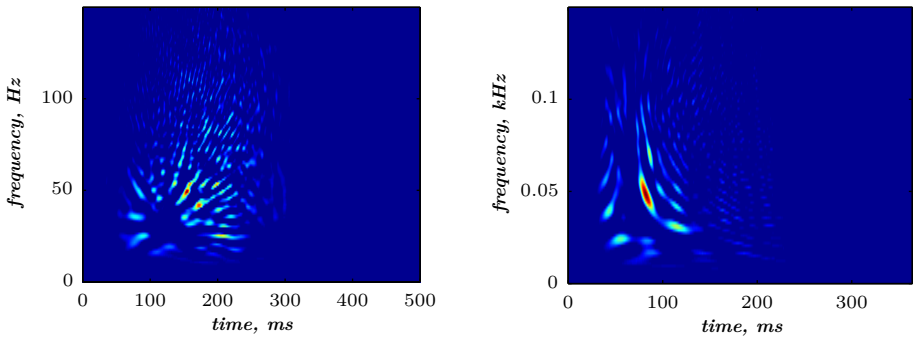


(a) WVD of averaged S1 (b) WVD of averaged S2

Figure III.40: WVD of adjusted averaging of S1 and S2 heart sounds (LGB–IRCM cardiac valve database: 10078.11).

Indeed, as illustrated in Figure III.40(a) & III.40(b), the *developed* technique yields a time–frequency detection of heart murmurs. Therefore, averaging systole and diastole phases within segmented PCG signals is invaluable during analysis.

### III.3.7 Murmurs detection according to severity

Phonocardiographic signals are usually used to maintain bioprosthesis and mechanical valves. Abnormal hemodynamics occur when bioprosthesis deteriorate after a long functioning period. Therefore, regular examination and analysis of PCG signals is a reliable tool to prevent such damage that can be fatal. Thus, detection of resonant modes within PCG signals reveals abnormal functioning and helps physicians to prevent serious impact on the health of the patient. The corresponding PCG signal obviously records abnormal sounds generated by the deteriorated prosthetic valves.

Aortic stenosis is considered to study the pathology severity within the time–frequency plane, since it is the usual pathology within the LGB–IRCM cardiac valve database. Three severity levels; light, mild, and severe, are studied through the time–frequency content of their corresponding PCG signals within data files: 10078 (St–Jude bioprosthesis), 20008 (Carpentier–Edwards bioprosthesis), and 10019 (non–common bioprosthesis type) of the LGB–IRCM cardiac valve database, respectively.

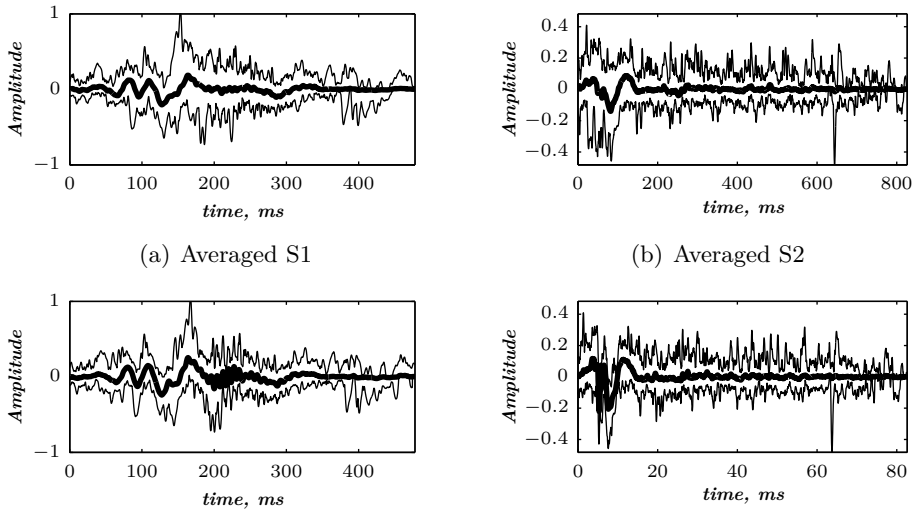


(a) Averaged S1

(b) Averaged S2

(c) Averaged & adjusted S1

(d) Averaged & adjusted S2

Figure III.41: Non–adjusted and adjusted averaging of S1 and S2 heart sounds, LGB–IRCM data file: 20008.11 (Aortic stenosis: mild).

As illustrated in Figure III.37(d), adjustment of systole and diastole phases carried out on PCG signals of the 10078.11 data file of the LGB–IRCM cardiac valve database is confirmed to be necessary before any processing. Successive cardiac cycles are represented as an envelope covering the averaged sounds to assess the

amount of background noise. Similarly, the non–adjusted and adjusted cardiac cycles of 20008.11 and 10019.11 data files are represented in Figures III.41&III.42, respectively. More clinical details about these data files can be found in the appendix in section **??**.

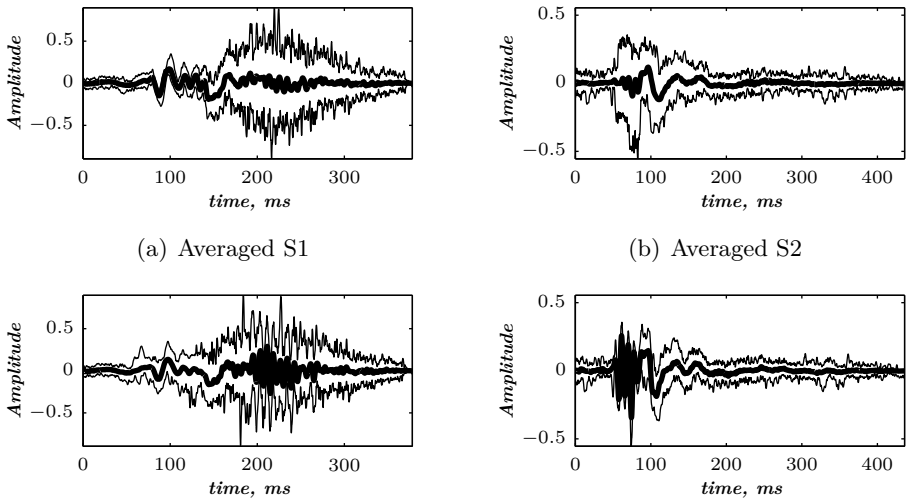


(a) Averaged S1

(b) Averaged S2

(c) Averaged & adjusted S1

(d) Averaged & adjusted S2

Figure III.42: Non–adjusted and adjusted averaging of S1 and S2 heart sounds, LGB–IRCM data file: 1001911.11 (Aortic stenosis: severe).

Expanded representations of these three PCG signals are illustrated in Figure III.43. Indeed, the systolic murmur resulting from the aortic stenosis follows the pathology severity both in amplitude and duration. This resonant sound

The SPWVDs of the adjusted and averaged aortic stenosis PCG signals at the three severity levels are illustrated in Figure III.44. The time–frequency distribution in Figure III.44(a) represents the S1 heart sound as an energy burst below 100 Hz. According to the obtained time–frequency distribution, the systolic murmur is light and is not significant in comparison to the S1 heart sound.

The mild and severe aortic stenosis of 20008.11 and 10019.11 PCG signals illustrated in Figures III.44(b) & III.44(c) respectively reveals a resonant mode at exactly 250 Hz. The energy bursts confirm the mild and severe nature of 20008.11 and 10019.11 despite their different bioprosthesis type. Therefore, the detected frequency within the time–frequency plane characterises the resonant mode of the deteriorated bioprosthesic valve for aortic stenosis. It should be noticed that the cross–correlation adjustment of systole and diastole phases play a major part in detecting resonant modes of bioprosthesic valves for maintenance purposes.

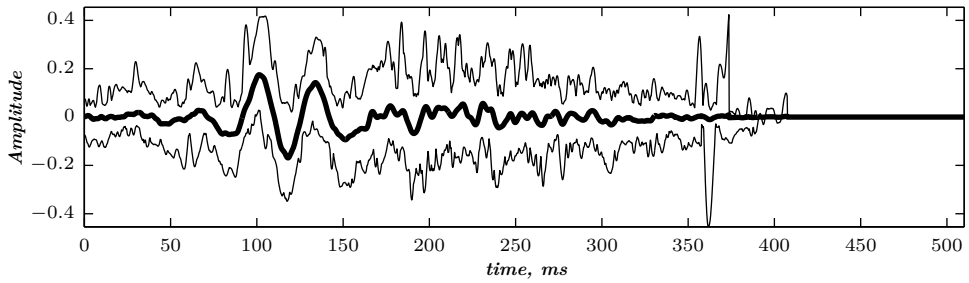


(a) Adjusted systole: 10078.11: light AS

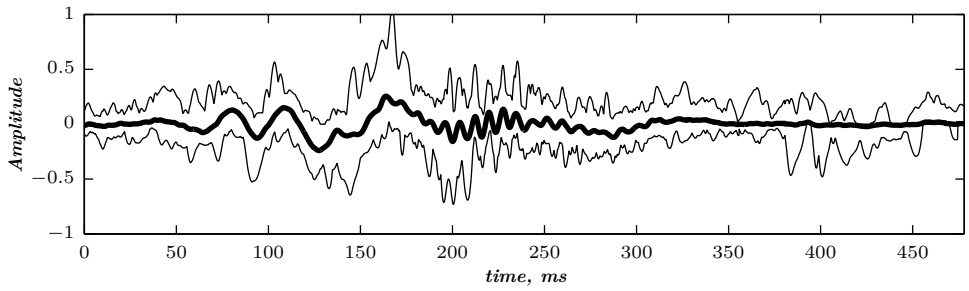


(b) Adjusted systole: 20008.11: mild AS

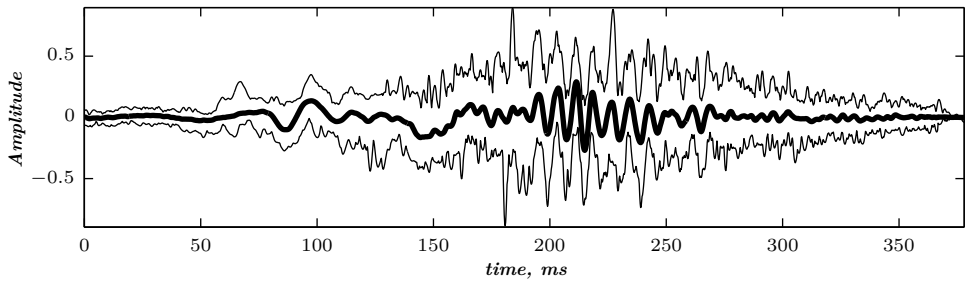


(c) Adjusted systole: 10019.11: severe AS

Figure III.43: Adjusted & averaged systole phases of (a) light (data file: 10078.11), (b) mild (data file: 20008.11), and (c) severe (data file: 10019.11) aortic stenosis PCG signals

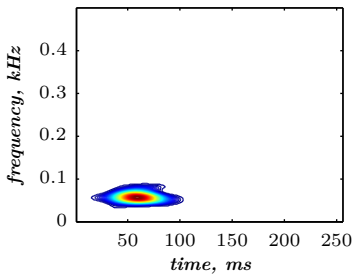


(a) SPWVD: 10078.11: light AS

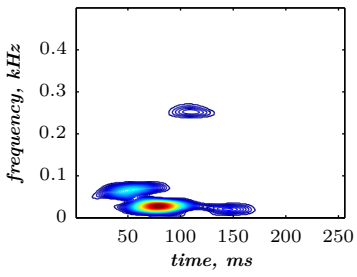


(b) SPWVD: 20008.11: mild AS

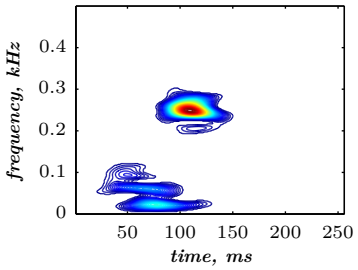


(c) SPWVD: 10019.11: severe AS

Figure III.44: SPWVDs of (a) light (data file: 10078.11), (b) mild (data file: 20008.11), and (c) severe (data file: 10019.11) aortic stenosis PCG signals

## III.4 Wavelet analysis applied to PCG signals

The wavelet transform can effectively analyse non–stationary time series over the frequency domain [115]. Wavelet analysis is then one of the useful tools allowing two-dimensional representation of signals. Indeed, by introducing a scale parameter of a dilated and compressed wavelet used as analysing function, the wavelet transform generates a Time-Scale Representation (TSR) of signals. Moreover, this TSR can be extended to the time–frequency plane by estimating the central frequency of the mother wavelet [116].

### III.4.1 Continuous wavelet transform

#### The valvular chirplet model (VCM)

Basic models of S1 and S2 heart sounds can be categorised into three types, namely; the exponentially damped sinusoidal model [117, 107, 108, 118, 119], matching pursuit method [109, 110], and linear chirp simulation method [106].

The exponentially damped sinusoidal model takes into account the internal cardiac hemodynamics. This model simulate heart sound through decaying tonal components at resonant frequencies of the heart as well as the heart–thorax system

(section I.4.3). However, this model requires four to twenty components to reproduce S1 and S2 heart sounds. Moreover, this model fails to retrace the transient chirp nature of S1 and S2 heart sounds. The serious drawback of the exponentially damped sinusoidal model is that separation of valvular components (M1 & T1 for S1, or A2 & P2 for S2), is not possible since the overall simulated sinusoidal components begin at the same time instant at the onset of each heart sound. The matching pursuit method models heart sounds as a sum of Gaussian sinusoids defined within the time–frequency plane. However, this model requires an important number of components for simulation. Moreover, this method cannot model transient chirps adequately. The linear chirp simulation model simulates each heart sound as a unique linear chirp which fails to represent vibrations within heart sounds. The chirp model proposed by Xu *et al.* [88, 89] outperforms these simulation methods, and reproduces the true content of S1 and S2 heart sounds by representing the valvular closure as a modulated frequency chirp.

Based on the Laplace's law, Aggio *et al.* [120] and Longhini *et al.* [121] shown that the instantaneous frequency of P2 (second component of the S2 heart sound) is proportional to the Pulmonary Artery Pressure (PAP). Bartels and Harder [122] demonstrates that the time–frequency analysis of S2 can yield an estimation of the arterial pressure. Therefore, A2 and P2 components are considered as decreasing frequency modulated chirps with an instantaneous frequency proportional to the decreasing arterial and pulmonary pressures respectively.

Valvular components forming S1 and S2, namely M1 and T1 for S1, and A2 and P2 for S2, are of hyperbolic modulated instantaneous frequency. Such a morphological behaviour of the heart sound component has been modelled by *Xu et al.* [89, 88] using a non–linear transient chirp signal. This model, which we name the Valvular Chirplet Model (VCM), as given in (III.4);

$$VCM(t) = A(t)\sin\varphi(t) \tag{III.4}$$

Where $A(t)$ and $\varphi(t)$ denotes respectively the amplitude and the phase of the VCM.

The simulated valvular component duration is limited to 60 ms, since the duration of aortic and pulmonary valvular component lasts generally less than 50 ms [88] (Xu et al., 2000).

The amplitude $A(t)$ of the VCM is then defined by;

$$A(t) = (1 - e^{-\frac{t}{8}})e^{-\frac{t}{16}}\sin\frac{\pi t}{60} \tag{III.5}$$

The attack and decay slope are defined by the first and the second terms of equationIII.5 respectively. The last term limits the duration to 60 ms (Figure III.17).

The phase $\varphi$ of the VCM is given by;

$$\varphi(t) = 2\pi(24.3t + 451.4\sqrt{t}) \tag{III.6}$$

The VCM consists of a hyperbolic frequency modulated chirp of limited duration. The chirplet amplitude is zero at t = 0 s and 250 Hz frequency which decreases to 53 Hz as illustrated in Figure III.17(a).

Wavelet analysis relies on stretching and compressing the mother wavelet when sweeping the scale domain. Thus, it is suitable to track down the chirplet content by means of the VCM which is acceptedly typical for heart sounds time–scale analysis.

**The developed VCM adapted wavelet** Wavelet analysis can be viewed as correlation between the signal and the mother wavelet which is shifted at position $b$ and dilated by scale $a$. Indeed, the coefficients of the wavelet transform reflect the similarity between the wavelet and the swept signal portions through the scale domain. To lift up the heart sounds energy within the time–frequency plane, it is obvious to look for a mother wavelet that can substantiate the valvular component within the TFR. The heart sound chirplet model oscillates like a wavelet and should be a good candidate for time–scale analysis of heart sounds. The unique condition about the chirplet model, to be a mother wavelet, is that its average should be zero. This is the admissibility condition for the chirplet to be viewed as a wavelet, as follows;

$$\int_{-\infty}^{+\infty} \psi(t)dt = 0 \tag{III.7}$$

This admissibility condition ensures to the signal to be well recovered after inversion of the wavelet transform. Equation III.7 can be viewed as zero–order moment condition. Another suitable property for the mother wavelet is regularity which consists of localisation within the frequency domain [123]. Indeed, III.45 shows the spectrum of the chirplet model which is well localised within the frequency domain. This spectrum is the Power Spectral Density (PSD) estimated by means of periodogram method [124, 125].

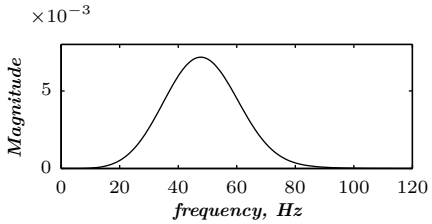


Figure III.45: Welch PSD estimate of the Normalised VCM.

The mother wavelet can have a number of vanishing moments as follows;

$$M_p = \int_{-\infty}^{+\infty} t^p \psi(t)dt = 0 \text{ for } p = 0, 1, 2, \ldots, n \tag{III.8}$$

That means that the $(n+1)$ derivatives of the mother wavelet spectrum are equal to zero at the frequency zero.

The analysis is carried out under a MATLAB environment by means of its Wavelet toolbox which allows us to build an admissible wavelet from a given pattern [126]. The pattern we use herein is the VCM which proves its invaluableness through the several tests we accomplished. The generated adapted wavelet is of norm equal to 1.

Figure III.46 gathers polynomial approximations of adapted wavelet at several order (order: 3, 6, 10, 15, 16, and 20). Using this fitting approach, admissible wavelet is constructed to fit the VCM for later detection by using the CWT. According to several values of the fitting polynomial order, Figure III.47 highlights the cross–correlation between the adapted wavelet and the VCM.

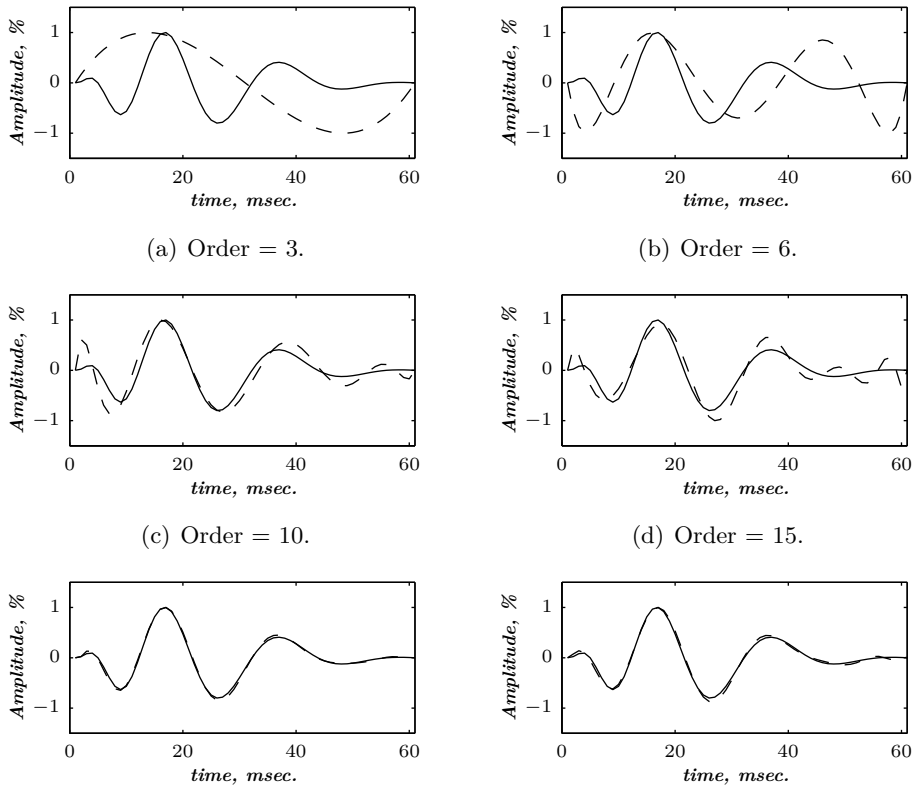


(a) Order = 3. (b) Order = 6.

(c) Order = 10. (d) Order = 15.

(e) Order = 16. (f) Order = 20.

Figure III.46: The VCM (solid line) and its adapted wavelet (dashed line): (a) Segmented systole phases, (b) Adjusted systole phases, (d) Segmented diastole phases, (f) Adjusted diastole phases.

Figure III.46 shows that reaching 15 as polynomial order lead to 98.59% as cross–correlation between the adapted wavelet and the VCM. For 35 as polynomial order, we get 99.88% as correlation. The adapted wavelet is more correlated to the VCM as the polynomial order increases. The constraints to be respected consist of ensuring almost zero integral, continuity at the beginning and the end of the adapted wavelet and a square norm equal to 1.

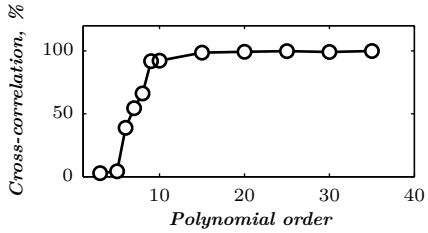


Figure III.47: Cross—correlation between the adapted wavelet and the VCM.

Therefore, we can now use the VCM within wavelet analysis since it can be modelled as an admissible mother wavelet. This model oscillates like a wavelet and ensure to heart sounds to be well analysed. In this study, we use the Morlet wavelet are a crude wavelet and the Discrete Meyer wavelet, which is a discrete improvement of the Meyer wavelet, to get a discussion area about the qualities of the **developed VCM adapted wavelet**.

**The Morlet wavelet** The Morlet wavelet is given by;

$$\psi(t) = e^{-\frac{t^2}{2}} \cos 5t \tag{III.9}$$

This is a crude wavelet with $[-4, 4]$ as theoretical effective support. However, a wider effective support can give more accurate results.

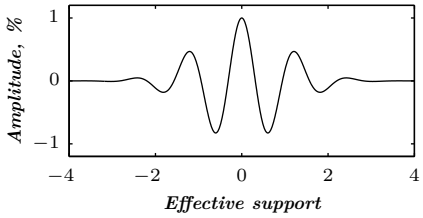


Figure III.48: The Morlet wavelet.

As cited in equation III.9, the frequency content of the Morlet wavelet is constant. The VCM, which is of frequency modulated nature, should give better result than the Morlet wavelet for heart sounds analysis.

**The Discrete Meyer wavelet** The Meyer wavelet [127] is symmetrical, ensures orthogonal and biorthogonal analysis and is infinitely derivable. However, it is not compactly supported, but decreases quickly towards 0 when t tends towards infinity. The FIR based approximation of the Meyer wavelet generates a pseudo–wavelet named the Discrete Meyer wavelet [116]. This approach allows fast wavelet coefficients calculation using the Discrete Wavelet Transform (DWT) which is not possible with the original Meyer wavelet. The discrete Meyer wavelet and its scaling function are respectively illustrated in Figure III.49. The Discrete Meyer wavelet is then considered for heart sounds analysis.

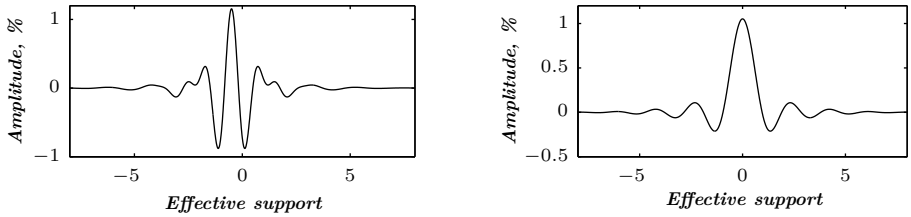


(a) Discrete Meyer wavelet. (b) Discrete Meyer Scaling function.

Figure III.49: Meyer: (a) Meyer wavelet, (b) Meyer scaling wavelet.

**Wavelet analysis of S1 and S2** The current study is carried out using PCG signals recorded by the *developed* data acquisition system (Figure III.1) within the CHUT[8]. Typical S1 and S2 heart sounds are selected and are considered separately for analysis as illustrated in Figure III.50.

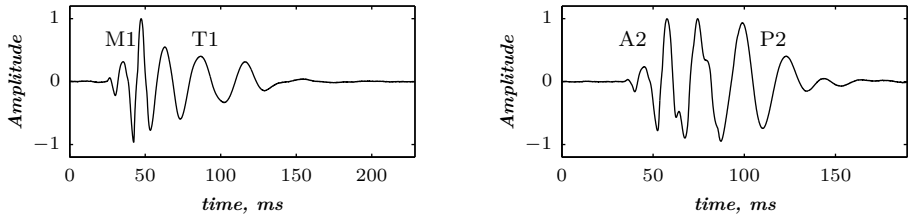


(a) S1 heart sound. (b) S2 heart sound.

Figure III.50: (a) S1 and (b) S2 heart sounds of a normal subject.

The S1 heart sound illustrated in III.50 shows clearly the frequency modulated behaviour of its M1 and T1 valvular components. The M1 component is more prominent within this S1 heart sound than T1. We can notice that oscillations within this S1 heart sound are of decreasing frequency and thus can obviously be considered as a chirp.

After the systole period appears the S2 heart sound (Figure III.50(b)) which is formed by the A2 and P2 valvular components. This heart sound is recorded after the S1 heart sound of Figure III.50(a) within the same phonocardiogram signal. The axis limits of both S1 and S2 heart sounds are conserved through the overall TFRs to have the ability to study the interconnection between the time–frequency energy bursts and their original time appearing instants.

The wavelet transform is a TSR ; however, a time–frequency representation can be generated from this TSR by estimating the central frequency of the mother wavelet throughout the scale dimension [116]. Thus, a time–frequency representation is provided by rearranging the time–scale coefficients according to the frequency vector estimate. To evaluate the effectiveness of the VCM as a mother wavelet candidate, we will use two mother wavelets, namely; the Morlet wavelet, which is a crude one,

[8]Centre hospitalier universitaire de Tlemcen

and the Discrete Meyer Wavelet, which is a discrete improvement of the original Meyer wavelet. These mother wavelets, which are used as opponent approaches, allow highlighting the ability of the VCM to be an analysing wavelet for heart sounds study. To allow rational comparison between the studied wavelets, common scales domain from 1 to 32 has been used for all wavelets. The TFRs are scaled by using a 'jet' colormap going from blue to red colours. We begin by analysing the first (S1) and second (S2) heart sounds using the Morlet wavelet and the discrete Meyer wavelet as basic methods. We accomplish than a time–scale analysis using the VCM (section III.3.4).

In a view to better understand the TFRs we calculated, we introduce the square energy envelogram of each heart sound. Figure III.51 shows the energy distribution in accordance to time domain of S1 and S2 heart sounds.

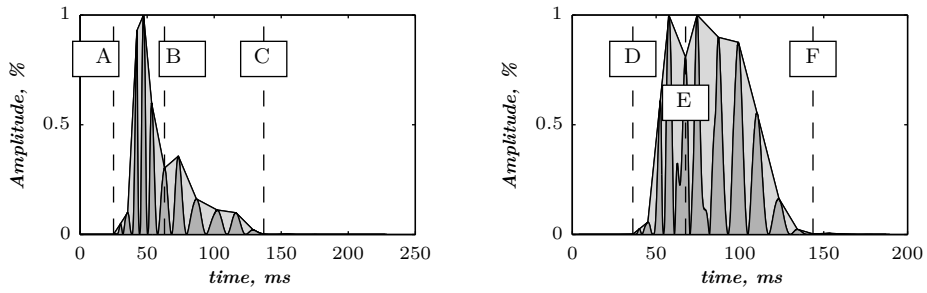


(a) (a) (b) (b)

Figure III.51: Square energy envelograms of (a) S1, and (b) S2 heart sounds.

Each heart sound envelogram include two bursts. By detecting local maxima within the obtained envelograms, we can segment each heart sound temporal energy as annotated by; A, B and C for the S1 heart sound, and by D, E and F for the S2 heart sound which allow us to delimit these energy bursts.

We can draw out a preliminary analysis of S1 and S2 heart sounds from the square energy envelograms of Figure III.51. This is a temporal analysis which allows appreciating the energy evolution through the time domain. We denote by; AB the duration between the lines A and B , BC the duration between the lines B and C in Fig III.51(a), and so on for durations DE and EF in Figure III.51(b) for the S2 heart sound. Both S1 and S2 contain two temporal energy bursts of different morphology. These segments are in relation with valvular activities; M1 and T1 for S1 and A2 and P2 for S2. Table III.3 shows a summary of S1 and S2 heart sounds and their segments durations. We denote segments AB and DE as 'First bursts' in since they appear first within square energy envelograms of Figure III.51. Subsequently, segments BC and EF are denoted as 'Second bursts' in Table III.4.

Eyster [128] shown that the average duration of the S1 heart sound is about 131 ms and that of the S2 heart sound is around 128 ms. However, Amit *et al.* [129] shown that heart sound can be modulated by the respiration activity and may often present variability in terms of duration. Indeed, as mentioned in Table III.3, the S1

| Heart sound | Duration (ms) | 1st burst (ms) | 2nd burst (ms) |
|---|---|---|---|
| S1 | 111.51 | 36.38 | 75.13 |
| S2 | 107.48 | 26.76 | 80.72 |

Table III.3: Heart Sounds Segments Durations.

| Heart sound | 1st burst | 2nd burst |
|---|---|---|
| S1 | 61.28 | 38.72 |
| S2 | 18.39 | 81.61 |

Table III.4: Temporal energy percentages within square energy envelograms.

heart sound lasts slightly longer than the S2 heart sound. This is due to the split phenomenon that can affect both S1 and S2 heart sounds.

Table III.4 shows the contribution of each energy segment (AB and BC for S1, DE and EF for S2) as percentage of the overall temporal energy.

The first reading we can draw out from Table III.4 is that the main energy of S1 heart sound is concentrated within the first burst at 61.28 % whereas the S2 heart sound energy is concentrated within the second burst at 81.61 %.

Spectral analysis is another helpful discussion tool we used which allows elucidating the calculated TFRs. The periodogram PSD estimates of each heart sound are shown in Figure III.52. The local minima of each PSD are localised and denoted by a 'v' letter shaped triangles.

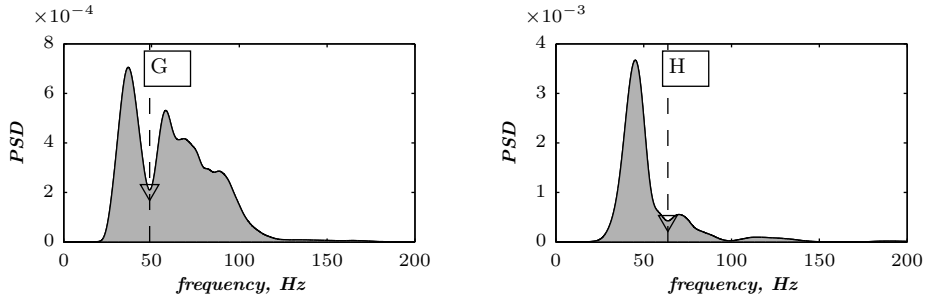


(a) PSD of S1

(b) PSD of S2

Figure III.52: Periodogram PSDs of (a) S1 (G: 48.25 Hz), and (b) S2 heart sounds (H: 63.25 Hz).

As for the time domain, the split of the power spectrum is localised and denoted by 'G' and 'H' lines for PSDs estimates of S1 and S2 respectively. In Figure III.52(a), two energy regions are well localised and are graphically separated by the line denoted by 'G' at 48.45 Hz. A similar shape is observed in Figure III.52(b). The line denoted by 'H' at 63.25 Hz delimits the two energy bursts of S2.

We quantify the contribution of each spectral energy burst as a percentage calculated over the total energy through the frequency domain. Table III.5 shows the

| Heart sound | 1st burst | 2nd burst |
|---|---|---|
| S1 | 35.18 | 64.82 |
| S2 | 81.04 | 18.96 |

Table III.5: Spectral energy percentages within S1 and S2 PSDs.

distribution of the spectral energy in accordance to each segment. Regions localised below and above lines 'G' and 'H' for S1 and S2 heart sounds power spectra are denoted as 'First burst' and 'Second burst' respectively.

We notice that the main energy of the S1 heart sound is concentrated above the 'G' line frequency (48.25 Hz), whereas the S2 heart sound spectral energy is below the 'H' line frequency (63.25 Hz).

By recalling results shown in Table III.4, we can deduce that there is an energy twist between the time and the frequency domains. Indeed, the first temporal burst of the S1 heart sound shows 61.28 % and its second burst within the frequency domain is of 64.82 % of energy. Moreover, the second temporal burst is of 38.72 % which is close to the first frequency burst of 35.18 %. We can understand this preliminary finding by the chirp nature of heart sounds. The energy of a heart sound over the time–frequency plane follows a hyperbolic frequency modulated behaviour. Two bursts appears for both S1 and S2 heart sounds because they are both formed by two valvular components, namely M1 and T1 for S1, and A2 and P2 for S2. This energy twist is also verified for the S2 heart sound. Indeed, we observe that the temporal energy percentages are around 18 and 81 % for the first and second bursts (Table III.4). These values are inverted for the frequency domain (Table III.5).

Taking into consideration this time and frequency partition carried out for both the S1 and S2 heart sounds which paves the way to the time–frequency analysis, we can then discuss more accurately the obtained TFRs. Figure III.53, Figure III.54, and Figure III.55, show TFRs of the S1 heart sound calculated from 1 to 32 as scales domain by means of the Morlet wavelet, discrete Meyer wavelet and VCM adapted wavelet respectively. The S2 heart sound analysis is presented in Figure III.56, Figure III.57, and Figure III.58.

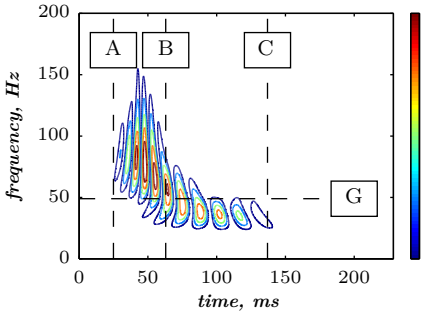


Figure III.53: Scalogram of the S1 heart sound using the Morlet wavelet.

The AB region within the TFR denotes the energy region delimited by the temporal lines A and B. The AB(f<G) region denotes energy between the lines A and

B as temporal delimiters for frequencies less than the G frequency (48.45 Hz) and the AB(f>G) for frequencies greater than the G frequency, and so on.

Taking into account the square energy envelogram of Figure III.51(a), the high energy burst appearing in the AB region is recognised as red contours on the TFR of Figure III.53. This is confirmed by the power spectrum of Figure III.52(a) since the energy in the frequency domain is distributed as a narrow burst before the G line and as a spread burst after this same delimiting line. Within the TFR of Figure III.53, the AB energy in concentrated above the G frequency and the BC region is localised below this same frequency.

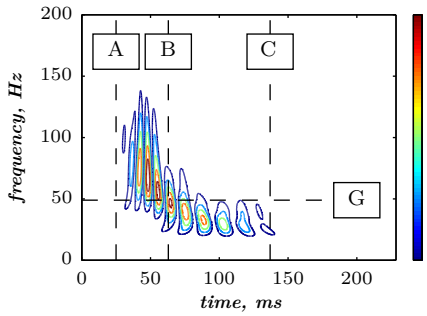


Figure III.54: Scalogram of the S1 heart sound using dmeyer wavelet.

The main contribution of the TFR is the interrelationship made between the time and the frequency domains to better understand the energy distribution of the analysed signal. Indeed, we can observe in Figure III.53, Figure III.54 and Figure III.55 that the AB narrow temporal burst appearing in Figure III.51(a) corresponds to a spread TFR energy region in the frequency domain as shown in Figure III.53. Furthermore, the BC energy which is of relatively reduced magnitude in comparison with the AB temporal burst.

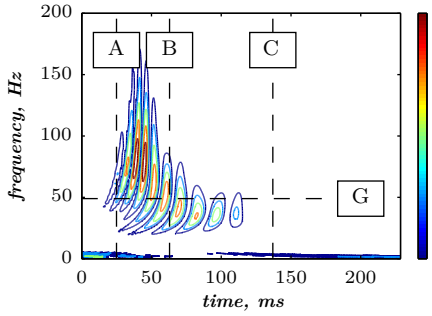


Figure III.55: Scalogram of the S1 heart sound using the VCM adapted wavelet.

The chirp shape within the overall TFRs calculated for the S1 and the S2 heart sound reflects the frequency modulated nature of heart sounds. The TFRs calculated by means of the VCM as mother wavelet blow up energised regions. Indeed, the region AB(f>G) reaches values around 225 Hz. The centre of bursts of higher magnitude denoted by red colour indicates the instantaneous frequency that can express the time–frequency behaviour of the analysed heart sound. It is obvious by comparing the TFR calculated by the VCM (Figure III.55) to those of the Morlet wavelet (Figure III.53) and the discrete Meyer wavelet (Figure III.54) that the VCM

is suitable for heart sound analysis since the obtained TFR evidently represents the frequency modulated components of the S1 heart sound. Similarly, the TFRs of Figure III.56, Figure III.57 and Figure III.58 illustrate the analysis results of the S2 heart sound using the Morlet wavelet, discrete Meyer wavelet and VCM wavelet respectively.

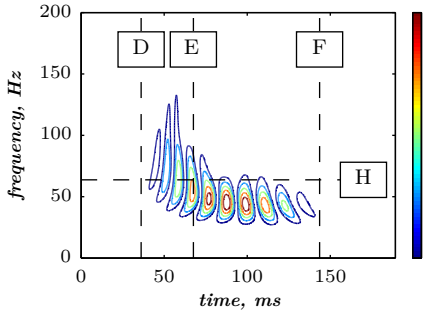


Figure III.56: Scalogram of the S2 heart sound using the Morlet wavelet.

The TFR of Figure III.58 shows the energy content of TFRs of Figure III.56 and Figure III.57, which are almost similar, on top of that is revealing energy bursts which are not detectable by the Morlet and the discrete Meyer wavelets. Indeed, the DE time–frequency region within Figure III.58 is more representative of the S2 heart sound energy. We can obviously remark that the TFR of Figure III.58 calculated by the VCM wavelet gives the best result. Indeed, the resulting TFR is well representative of the square energy envelogram of Figure III.51(b) and the power spectrum of Figure III.52(b).

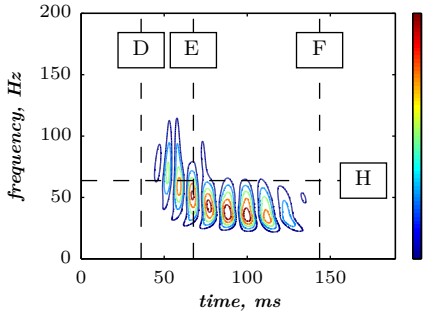


Figure III.57: Scalogram of the S2 heart sound using the discrete Meyer wavelet.

We introduce an energy percentage calculation within the time–frequency plane to clarify the impact of the *developed* VCM adapted wavelet.

| Frequency | AB | BC |
|---|---|---|
| f > G | 15.28 | 08.72 |
| f < G | 11.24 | 49.29 |

Table III.6: Energy distribution of S1 (Morlet wavelet).

| Frequency | AB | BC |
|---|---|---|
| f > G | 13.50 | 07.78 |
| f < G | 11.07 | 52.49 |

Table III.7: Energy distribution of S1 (Discrete Meyer wavelet).

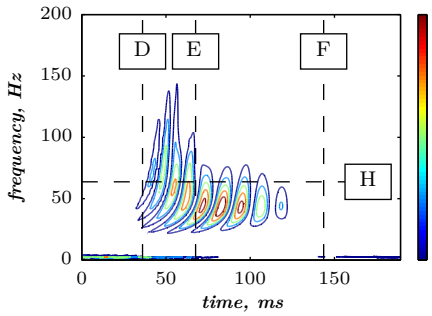


Figure III.58: Scalogram of the S2 heart sound using the VCM adapted wavelet.

Energy percentages are calculated over the time–frequency plane for both S1 and S2 heart sounds. This approach is applied for the Morlet wavelet, discrete Meyer wavelet and VCM adapted wavelet.

Table III.6 and Table III.7 show extremities of the chirp behaviour of heart sounds as 15.28% and 49.29% of the overall energy. Indeed, this can be confirmed by TFRs of Figure III.53 and Figure III.54 which presents and AB(f<G) region relatively of reduced energy.

By analysing Table III.8, we can obviously notice the chirp behaviour going from high frequency domain, passing by the AB(f<G) region with a boosted TFR coefficients, and decreasing to the BC(f<G) energy region. Going from 15.93%, passing by 24.18% and decreasing in frequency to 40.08%, the chirplet based TFR boosts the AB(f<G) region which is of reduced values of approximately 11% of the total energy for the Morlet and the discrete Meyer wavelets.

This analysis can be extended to the second heart sound. Table III.9 and Table III.10 show the chirp behaviour through the bold text values percentages of the TFR total energy.

| Frequency | AB | BC |
|---|---|---|
| f > G | 15.93 | 07.36 |
| f < G | 24.18 | 40.08 |

Table III.8: Energy distribution of S1 (VCM Adapted Wavelet).

| Frequency | DE | EF |
|---|---|---|
| f > H | 05.33 | 05.52 |
| f < H | 08.26 | 67.54 |

Table III.9: Energy distribution of S2 (Morlet wavelet).

| Frequency | DE | EF |
|---|---|---|
| f > H | 03.99 | 04.12 |
| f < H | 08.05 | 70.87 |

Table III.10: Energy distribution of S2 (discrete Meyer wavelet).

The Morlet wavelet and the discrete Meyer wavelet can therefore regenerate the chirp shape within the time–frequency plane.

Comparing results of Table III.9 and Table III.10 with those of Table III.11 allow to recognise the aptitude of the VCM adapted wavelet to well represent heart sounds within the time–frequency plane. Indeed, the DE(f < H) energy region, which was of poor percentage over Table III.9 and Table III.10, is more representative of the heart sound content at 23.71% of the TFR total energy (Table III.11).

Table III.12 gathers energy percentages in relation with the chirp shape within heart sounds. The sum of the following energies: AB(f > G), AB(f < G) and BC(f < G) is calculated for each mother wavelet. This 'L' letter shape within Table III.6–III.11 is correlated with the chirp content of heart sounds. Indeed, Table III.12 shows that the VCM adapted wavelet is suitable for detecting the chirp behaviour within both S1 and S2 at higher energy percentages in comparison to Morlet and discrete Meyer wavelets. **Therefore, the VCM adapted wavelet can be considered as an ad–hoc wavelet for analysing phonocardiographic signals.**

### III.4.2 Wavelet packets

Heart murmurs are signs of valvular malfunction and are categorised as systolic and diastolic murmurs. Generally, these murmurs families are both affecting the four intracardiac valves in terms of stenosis or insufficiency. Therefore, there are multitude of malfunction configurations for each single valve which can be combinations of stenosis and insufficiency. This makes heart murmurs very complex to detect and analyse. In a previous work, a temporal analysis of heart sounds and murmurs allows us to separate systole and diastole phases within a cardiac cycle [10]. Liang *et al.* [11] proposed an algorithm based on the normalised average Shannon energy of

| Frequency | DE | EF |
|---|---|---|
| f > H | 04.83 | 05.43 |
| f < H | 23.71 | 55.55 |

Table III.11: Energy distribution of S2 (VCM adapted wavelet).

| Heart sound | Morlet | dMeyer | VCM |
|---|---|---|---|
| S1 | 75.81 | 77.06 | 80.19 |
| S2 | 81.13 | 82.91 | 84.09 |

Table III.12: Chirplet energy percentages within TFR calculated by Morlet wavelet, discrete Meyer wavelet, and VCM adapted wavelet.

the PCG signal to detect systolic and diastolic heart sounds and murmurs. Spectral analysis methods can be combined with such time domain analysis to assess the valvular pathology severity. Clarke *et al.* [12] studied the spectral content of the first heart sound and concluded that its spectral energy can be used to detect myocardial ischemia. Stein *et al.* [13] found that the aortic component of the second heart sound can be investigated as a characterization parameter of the aortic valve status. They reported that a stiffened valve generates a higher than normal frequency of the A2 component. Therefore, both temporal and spectral approaches should be combined to study the physiological information within heart sounds and murmurs. Thus, these short–duration acoustic waveforms which occupies different frequency subbands inside the PCG power spectrum can be adequately analysed by means of multiresolution methods as the wavelet packets decomposition.

The Fourier theory can give a frequency overview of a signal through power spectral density (PSD) which can be estimated as a periodogram or even more a modified periodogram known as Welch's periodogram [130, 124, 79]. Only a frequency dependent energy estimation can be provided by Fourier–based PSD estimation methods. However, Gabor transform and its obvious extension which is the short–time Fourier transform (STFT) enables a time–related frequency analysis. This can be achieved by segmenting a given signal into elementary portions to be analysed by the discrete Fourier transform (DFT). Each spectrum is assigned to the middle instant of the weighting window to create a time dimension within the STFT representation. The main restraint facing the STFT to represent signals is its poor joint time–frequency localisation within the time–frequency plane. Wavelets are then the bright solution to this well known digital signal processing issue towards representing transients within biomedical signals. Indeed, wavelet transform, which is based on a scale parameter rather than frequency, can prominently outstand in representing the complex content of PCG signals and outperform all Fourier–based methods.

Through wavelet packets, normal and abnormal PCG signals are analysed globally without any temporal segmentation step required. The analysis method is mainly based on energy subbands provided by the wavelet packets decomposition (WPD).

A number of cardiac disorders of the CHUT database were studied. We used the wavelet packets decomposition to characterise the contribution of every energy subband within a PCG signal. The bandwidth of each PCG signal is decomposed into 8 frequency subbands which corresponds to 3 decomposition levels as depicted in Table II.2 . Moreover, a downsampling step is necessary to enable analysis of heart sounds and murmurs within their regular spectral bandwidth. The downsampling

is achieved at 600 Hz. Therefore, according to the Nyquist sampling rate condition, we can view spectral content up to half the sampling rate which corresponds to 300 Hz. With a PC equipped by an Intel Core 2 Duo CPU operating at 2.20 GHz, we achieved an extreme calculation time performance.

### Subband energy ratio calculation

Each energy subband is quantified by its wavelet packets' normalised subband energy (WPNSE), which is the contribution of every frequency subband in a given PCG signal to its global energy, according the following algorithmic steps;

- Calculate the wavelet packets' coefficients at level $N = 3$ which yields $2^N = 8$ subbands. We choose this value as a trade–off between a good CPU time performance and an acceptable frequency subbands separation among the analysed PCG signals.
- Calculate the WPNSE for each frequency subband at level $N$.
- Determine the energy subband at higher energy coefficient through the eight ($2^N$) frequency subbands.

In order to elaborate a coherent study among the analysed PCG signals, we select a unique mother wavelet for the overall analysed PCG signals to represent the energy ratio which is calculated for all wavelet packets. The choice of the mother wavelet is still controversy in analysing biomedical signals. Rafiee *et al.* [131] studied Daubechies 44 (db44) as a common mother wavelet for biomedical signal processing and concluded that it can be selected over all existing wavelet as optimum one for analysing any kind of biomedical signals.

### Wavelet packets PCG Analyser

We gather all wavelet packets analysis approaches within a Graphical User Interface (GUI) which has been **developed** within MATLAB environment. This interface, allows quick and accessible digital signal processing of the Phonocardiogram. The data files stored under '.PCG' format, which have been recorded by means of the *PCG Recorder*, are processed by the *Wavelet packets PCG Analyser*. Energies calculated over the elementary wavelet packets are presented numerically and graphically to ensure visual assessment of the PCG energy distribution over frequency domain.

The GUI illustrated in Figure III.59 is *developed* within MATLAB environment benefits of functionalities of the Wavelet Toolbox of MATLAB environment.

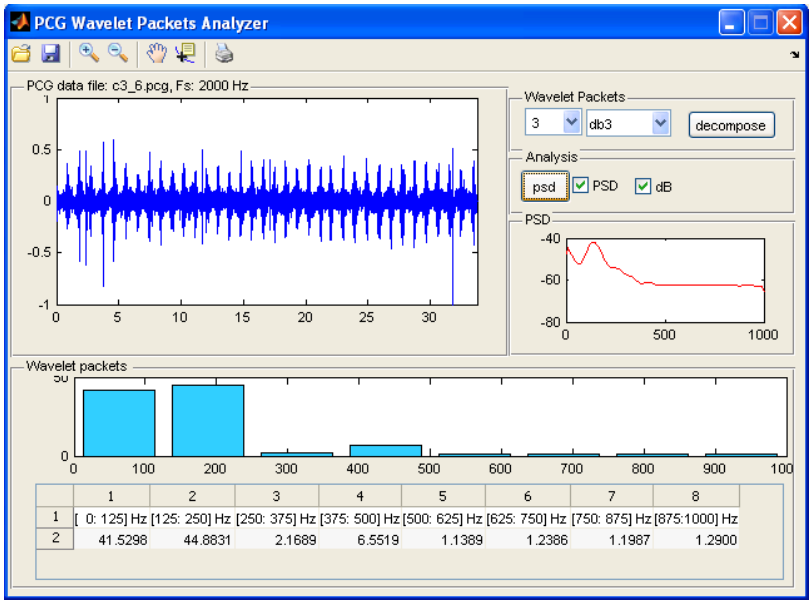


Figure III.59: Graphical User Interface (GUI) of the *Wavelet packets PCG Analyser*.

### Wavelet packets energy subband decomposition of PCG signals

The analysis results of PCG signals recorded at the CHUT of six pathologies are presented, namely; the aortic regurgitation, aortic stenosis, mitral regurgitation, mitral stenosis, pericardial friction rub, ventricular septal defect, as well as a normal subject for comparison as presented in Table III.13. According to Figure III.60, which illustrates normal, aortic stenosis and mitral stenosis PCG signals and their corresponding wavelet packets normalised subband energies (WPNSEs), each pathology can be easily differentiated from the other. Results presented in Figure III.60 are selected from Table III.13.

| PCG signal | Energy Subbands, up to 300 Hz | | | | | | | |
|---|---|---|---|---|---|---|---|---|
| | $1^{st}$ | $2^{nd}$ | $3^{rd}$ | $4^{th}$ | $5^{th}$ | $6^{th}$ | $7^{th}$ | $8^{th}$ |
| | [0:37.5] | [37.5:75] | [75:112.5] | [112.5:150] | [150:187.5] | [187.5:225] | [225:262.5] | [262.5:300] |
| Normal | 45.9220 | 34.8272 | 4.1075 | 10.7438 | 0.9315 | 2.1730 | 0.1612 | 1.1338 |
| Aortic regurgitation | 0.5598 | 13.9844 | 1.6587 | 66.7207 | 0.1605 | 6.5169 | 0.7613 | 9.6377 |
| Aortic stenosis | 2.2538 | 1.5484 | 42.7596 | 5.8671 | 1.8130 | 1.7398 | 36.5988 | 7.4194 |
| Mitral regurgitation | 1.0227 | 40.6910 | 1.2897 | 35.9106 | 1.1113 | 7.2920 | 0.4506 | 12.2321 |
| Mitral stenosis | 24.9496 | 33.6299 | 9.7248 | 19.4161 | 1.1547 | 3.1172 | 3.6108 | 4.3969 |
| Pericardial friction rub | 1.5258 | 21.5719 | 3.0718 | 50.3838 | 0.7086 | 7.3431 | 2.9471 | 12.4480 |
| Ventricular septal defect | 1.8692 | 30.1653 | 7.0658 | 23.7051 | 1.8116 | 9.3035 | 12.1271 | 13.9524 |

Table III.13: Wavelet packets' energy subbands decomposition of normal and abnormal PCG signals, Fs=600 Hz.

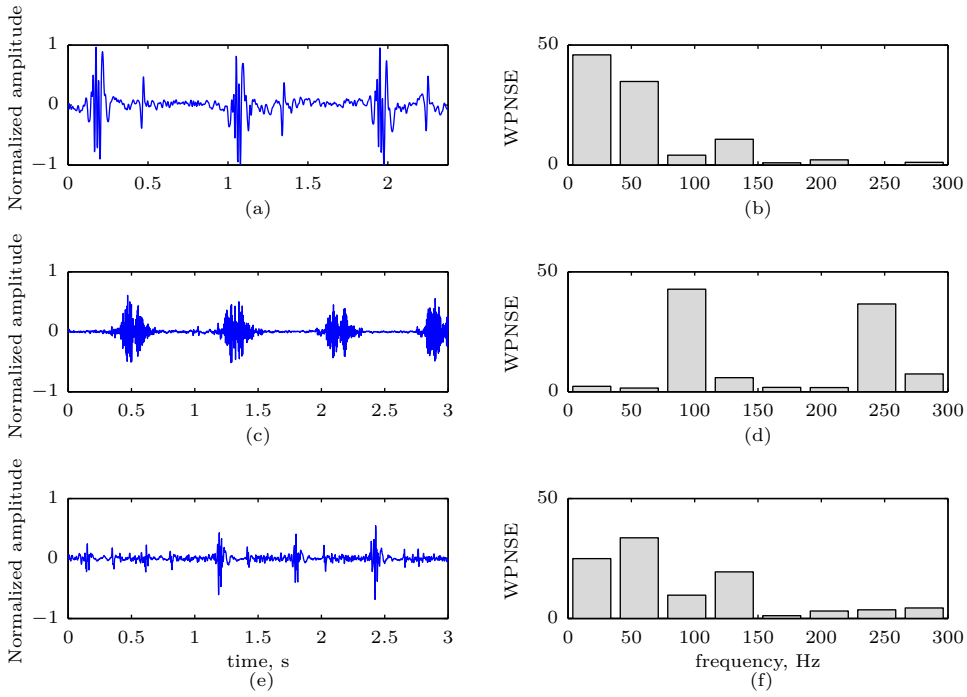


Figure III.60: (a) Normal, (c) aortic stenosis and (e) mitral stenosis PCG signals and their corresponding WPNSEs (b), (d) and (f), (Numerical results from Table III.13).

The energy of the normal PCG signal is mainly localised at the first bandwidth up to 37.5 Hz which corresponds to $\frac{F_s}{16}$ at approximately 45 % of its global energy.

According to Table III.13, we can notice that this bandwidth is not significant for the overall pathologies. However, the mitral stenosis contains about 24 % within this same bandwidth.

The S1 and S2 heart sounds are considerably attenuated in aortic stenosis sounds and therefore should not appear in the WP energy representation. Indeed, Figures III.60(c) & (d) shows clearly the low energy of the S1 and S2 heart sounds at the first subband ($[0 : 37.5]$ Hz). The aortic stenosis is then localised on the third ($[75 : 112.5]$ Hz) and the seventh ($[225 : 262.5]$ Hz) energy subband at about 42 % and 36 % of its global energy. The other subbands are not significant. As illustrated in Figures III.60 (e)&(f), the mitral stenosis show a content clearly different from that of the normal subject. Indeed, The first energy subband is diminished in comparison to that of the normal PCG signal. We notice that there is no significant change in its second subband energy when compared to the normal subject. However, the fourth energy subband is slightly increased in comparison with that of the normal subject.

According to Table III.13, the contrast between all abnormal PCG signals as well the normal subject is obvious. Indeed, there is no correlated signals in terms of the obtained energy subbands. Therefore, the WPNSE coefficient can be considered as a reliable discrimination parameter between these cardiac disorders.

## III.5 Conclusion

Phonoardiographic signals emanating from the CHUT[9] and the LGB–IRCM[10] cardiac valve database. The CHUT's PCG signals were recorded by the *PCG Recorder* system *developed* within this work.

Phonocardiographic signals recorded at the CHUT were analysed by the Smoothed–pseudo Wigner–Ville distribution. The obtained results were quantified according to each high energy time–frequency area. Heart sounds and murmurs were also quantified according to the auscultation area.

Preprocessing is carried out on PCG signals of the LGB–IRCM cardiac valve database by segmenting PCG signal in systole and diastole. Segmentation is based on detecting the R–peak and the end of the T–wave of the simultaneously recorded ECG signal as markers of systole and diastole phases. The jitter issue of the second heart sound is solved by adjusting the overall diastole phases within a phonocardiographic signal in the time domain. Subsequently, a *developed* envelope recovery algorithm saves information at the onset and end of heart sounds during time–frequency analysis.

The Reassigned smoothed–pseudo Wigner–Ville distribution has been selected over several time–frequency methods on account of its reliable features to adequately represent the content of phonocardiographic signals. The Reassigned smoothed–pseudo Wigner–Ville distribution of heart sounds was computed for each averaged

[9]Centre hospitalier universitaire de Tlemcen

[10]Laboratoire de Génie biomédical–Institut de recherches cliniques de Montréal, Quebec, Canada.

and adjusted heart sound. Thus, valvular sounds are detected as decreasing modulated frequency chirp–like component. Their attack and decay frequencies were detected within the time–frequency plane to dechirp them despite phase cancellation during their transmission from the heart to the chest.

Time–scale analysis of phonocardiographic signals carried out through Continuous wavelet transform as complementary multiresolution analysis tool. Among the huge number of mother wavelet that can be used during analysis, an adapted wavelet has been *developed* from a valvular component model. The analysis has been compared to Morlet and discrete Meyer wavelets to highlight the improvement in the obtained results.

A detection technique of heart murmurs was developed and validated on real phonocardiographic signals of the LGB–IRCM cardiac valve database. Moreover, the Smoothed pseudo Wigner–Ville distribution was computed for PCG signals under bioprosthetic valve anomaly. It has been shown that the pathology severity (light, mild, and severe) affect the time–frequency content of the corresponding PCG signals. Therefore, the time–frequency content of PCG signal became a reliable tool to detect resonant modes in relation with abnormal functioning of prosthetic valves for maintenance purposes.

In order to get a global analysis of heart sounds and murmurs within phonocardiographic signals, wavelet packets were investigated to represent its forming frequency bandwidths. Eight frequency bandwidths spread out up to 300Hz were sufficient to characterise the content of normal and abnormal phonocardiographic signals.

The analysis achieved within this chapter contributes to confirm the multidegree of freedom theory presented in section I.4.5, which stipulates that heart sounds are mainly originated by pressure fluctuations around the valves leaflets, and are mainly formed by chirps.

# Conclusion

Time–frequency analysis has been applied firstly on simulated phonocardiographic signals, and secondly on real data emanating from both CHUT[11], and from the LGB–IRCM[12] cardiac valve database recorded in the Institut de recherches cliniques de Montréal and the Montreal General Jewish Hospital in Montreal (Quebec, Canada). Recording of the CHUT's data has been performed by a data acquisition system, named *PCG Recorder*, developed by the author during this work. The recorded phonocardiographic signals are of high quality, and were acquired upon the chest of the patient from the four auscultation areas; namely aortic, pulmonary, mitral ,and tricuspid areas. Clinical information about each patient admitted in the Cardiology department of the Teaching hospital of Tlemcen were appended as metadata to the corresponding datafile.

Phonocardiographic signals emanating from the IRCM are segmented in systole and diastole phases by detecting the R–peak and the end of the T–wave of the simultaneously recorded ECG signal. A cross–correlation adjustment has been carried out to avoid jitter of the heart sound which causes attenuation of its forming components during averaging.

The frequency content within heart sounds is altered as a result of an intracardiac abnormality. An aortic stenosis PCG signal is considered for analysis by the Smoothed pseudo Wigner–Ville distribution to show the difference between normal and abnormal PCG signals. Moreover, four auscultation areas has been considered for the PCG recording.

This frequency alternating aspect of normal heart sounds cannot be detected for aortic stenosis heart sounds, as for several cardiovascular pathologies, because of the weakness of S1 and S2 heart sounds in comparison to the strong systolic ejection murmur. However, modulations laws around 150 and 180 Hz related to the stricture of the aortic orifice are well characterised. Moreover, the tricuspid auscultation area has been considered as the region upon the chest to be more able to retrieve S1 and S2 heart sounds with comparable intensities. Indeed, aortic stenosis heart sounds when acquired from this auscultation area contain S1 and S2 heart sounds with similar shapes to the normal case, but at lower frequencies. The acquisition and analysis system developed within this work allow to physicians to overcome the human hearing limitation by time–frequency characterization of heart sounds.

[11] Centre hospitalier universitaire de Tlemcen, Algeria.

[12] Laboratoire de Génie biomédical–Institut de recherches cliniques de Montréal, Quebec, Canada.

The SPWVD provides high time and frequency resolution within the time–frequency plane. Auscultation areas; namely the aortic, tricuspid, mitral and pulmonic, are taken into account to lead to a pragmatic interpretation by attributing each spectral activity to its originating cardiac valve or cavity. The time–frequency analysis carried out by means of the SPWVD upon normal and aortic stenosis heart sounds allow us to retrieve features of each case. For normal heart sounds, an alternating functioning of heart valves is unravelled. Indeed, the frequency content of the S1 and S2 heart sounds throughout the PCG signal alters with regard to valves sharing the same cardiac cavity. Aortic stenosis heart sounds were involved in our study in a view to confirm their pathological nature towards the normal heart sounds findings. Indeed, the weaken S1 and S2 heart sounds and the strong systolic ejection murmur which dominates the overall systole confirm our hypotheses. Thus, modulations laws related to the systolic ejection of blood through the stenosed orifice were characterised by means of the reliable SPWVD approach. A third heart sound (S3) which is an indicator of the presence of systolic dysfunction and elevated filling pressure for aortic stenosis lesion was also characterised.

The Reassigned Smoothed Pseudo Wigner–Ville Distribution (RSPWVD) has been used to analyse heart sounds as a modified method to the classical Wigner–Ville Distribution (WVD). It was found out that the RSPWVD improves considerably the resolution in comparison to the WVD and the SPWVD methods. The Reassignment mixed to the smoothing achieved both in time and frequency domains by the SPWVD brings a new quality to time–frequency analysis. Indeed, a chirp–like representation of S1 was obtained. Since the recording was done upon the tricuspid auscultation area, then the S1 heart sound is of larger energy than that of the S2 heart sound. It was observed that the tricuspid (T1) valvular component has a chirp nature with a frequency decreasing from 100 $Hz$ to 50 $Hz$. The beginning frequency should be larger that 100 $Hz$ since the attack of the chirp envelope is reduced at the onset of the S1 heart sound. By moving the stethoscope head to the mitral auscultation area, the mitral activity is recorded as a chirp which overlap with the tricuspid one. The modulated law of the mitral valvular activity is clarified within the time–frequency plane through the RSPWVD, which is a powerful tool for heart sounds analysis allowing to understand their chirp nature at a better time and frequency resolutions in comparison to other time–frequency methods.

A detection algorithm of the valvular split of S1 and S2 was developed on the basis of processing their corresponding RSPWVDs. The Reassignment mixed to the smoothing achieved both in time and frequency domains by the SPWVD provides a higher readability to the obtained RSPWVD. The proposed preprocessing envelope recovery procedure adapts the analysed heart sounds to the WVD which is optimal for analysing frequency modulated chirps. The performance of the algorithm is confirmed on simulated heart sounds at various split durations (30, 40, 50 and 60 ms). The A2–P2 valvular split is localised at the frequency inflection in the obtained RSPWVD. The developed algorithm is then validated on real heart sounds of the LGB–IRCM cardiac valve database and retraces the inflection of the A2–P2 valvular split of the S2 heart sound within the time–frequency plane. The discrete IF is estimated for both simulated and real data to confirm the results obtained through

the RSPWVD. Therefore, the proposed algorithm deals adequately with detecting the A2–P2 valvular split and confirms the chirp behaviour of heart sounds. Thus, it has been demonstrated through the developed algorithm that the valvular split can be accurately detected through the RSPWVD of heart sounds. Moreover, a dechirping algorithm was developed to separate the forming valvular chirps of each heart sound. Validation of the developed dechirping algorithm was also performed on simulated and real PCG signals of the LGB–IRCM cardiac valve database.

Time–scale analysis investigates the modulated frequency content of Heart sounds. The Valvular chirplet model adapted wavelet formed by the valvular chirplet model (VCM) was confirmed to be a reliable tool for heart sound analysis since it yields a better TFR in comparison to that obtained by means of Morlet wavelet as well as the discrete Meyer wavelet as opponent approaches. By reaching 98.59% of cross–correlation between the adapted wavelet and the original chirplet for 15 as fitting polynomial order, this order was considered to compute the VCM adapted wavelet used in analysis. Time–frequency representations are generated from the time–scale representations by estimating the central frequency of the mother wavelet. The VCM adapted wavelet related time–frequency representations achieve a better analysis towards heart sounds. Indeed, a quantitative study of the obtained time frequency representations confirms that the time–frequency plane is well represented by the VCM than the Morlet wavelet or discrete Meyer wavelet. Furthermore, the VCM adapted wavelet represents adequately more than 80% of the analysed S1 and S2 heart sounds energy which is in direct relation with their frequency modulated components. The Morlet wavelet and the discrete Meyer wavelet yields reduced energy percentages in comparison to those obtained by the VCM adapted wavelet. Therefore, the VCM adapted wavelet is more suitable for heart sounds characterisation within the time–frequency plane.

Heart murmurs were detected directly within the time–frequency plane. The developed technique was performed on real PCG signals of the LGB–IRCM cardiac valve database. The obtained results confirm the random behaviour of heart murmurs which are considerably reduced after averaging PCG signals over cardiac cycles. However, adjusted systole phases of PCG signals of patients with bioprosthetic valves placed in the aortic orifice are analysed by the Smoothed pseudo Wigner–Ville distribution to detect their systolic murmur. The obtained results highlight a resonant mode at 250 Hz within the adjuted systole phase which is accentuated according to the pathology severity (light, mild, and severe). energy of the detected resonant mode within the time–frequency plane can serve to assess the pathology severity as a reliable detection parameter.

A detection technique of heart murmurs was developed and validated on real phonocardiographic signals of the LGB–IRCM cardiac valve database. Moreover, the Smoothed pseudo Wigner–Ville distribution was computed for PCG signals under bioprosthetic valve anomaly. It has been shown that the pathology severity (light, mild, and severe) affect the time–frequency content of the corresponding PCG signals. Therefore, the time–frequency content of PCG signal became a reliable tool to detect resonant modes in relation with abnormal functioning of prosthetic valves

for maintenance purposes.

A global analysis is achieved through wavelet packets to quantify heart murmurs. The decomposition carried out by wavelet packets provides a reliable analysis of PCG signals. Indeed, after analysing both normal and abnormal PCG signals, we can clearly conclude that heart murmurs can be adequately quantified by means of wavelet packets without any temporal segmentation. The six cardiac disorders studied in section III.4.2, namely the aortic regurgitation, aortic stenosis, mitral regurgitation, mitral stenosis, pericardial friction rub, and ventricular septal defect as well as a normal PCG signal were accurately quantified. In fact, the obtained results show that the proposed wavelet packets normalised subband energy (WPNSE) parameter revealed a reliable discrimination between the overall studied pathologies. Thus, eight energy subbands up to 300 Hz were sufficient to highlight the contrast between the contribution of each pathology to its corresponding PCG signal.

The present work is an innovative contribution in resolving some main issues during phonocardiographic signal analysis; namely amplitude attenuation and phase cancellation. Moreover, murmurs were detected directly within the time–frequency plane. Additionally, an adapted wavelet was developed to represent the energy of the PCG signals within the time–frequency plane. Thus, the developed processing algorithms resolving these issues are innovative and are useful in further processing of phonocardiographic signals, which still an invaluable tool within medical diagnosis.

# Bibliography


[1] L. Werner, B. Pitts, D. Gilsdorf, and L. S. Bickley, *HeartSounds [electronic resource] : basic cardiac auscultation.* [Philadelphia, PA]: Lippincott Williams & Wilkins, 2003.

[2] A. Djebbari and F. Bereksi-Reguig, "Acquisition and time–frequency analysis of the phonocardiogram signal," in *Conférence Internationale sur les Systèmes de Télécommunications, d'Electronique Médicale et d'Automatique (CISTEMA'2003).* University of Tlemcen, Algeria, 2003.

[3] ——, "A new chirpŰbased wavelet for heart sounds timeŰfrequency analysis," *International Journal on Communications Antenna and Propagation (IRECAP)*, vol. 1, no. 1, pp. 92–102, February 2011.

[4] L. Durand and R. Guardo, "A model of the heart-thorax acoustic system," *Applications of computers in medicine*, pp. 29–41, 1982.

[5] L. Durand and P. Pibarot, "Digital signal processing of the Phonocardiogram: Review of the most recent advancements," *Critical Reviews in Biomedical Engineering*, vol. 23, no. 3-4, p. 163, 1995.

[6] L. Durand, "Comparison of pattern recognition methods for computer-assisted classification of spectra of heart sounds in patients with a porcine bioprosthetic valve implanted in the mitral position," *IEEE Transactions on Biomedical Engineering*, vol. 37, no. 12, pp. 1121–1129, 1990.

[7] A. Djebbari and F. Bereksi-Reguig, "Systolic blood ejection spectral characterization within aortic stenosis heart sounds," in *The International Conference on Complex Systems (CISC'2004).* University of Jijel, Algeria, 2004.

[8] ——, "Parametric spectral analysis of normal and abnormal heart sounds," in *International Conference on Electrical/Electronics Engineering Communication & Physical Systems (ELECOM'04).* University of Saida, 2004.

[9] J. Wood and D. Barry, "Quantification of first heart sound frequency dynamics across the human chest wall," *Medical and Biological Engineering and Computing*, vol. 32, pp. 71–78, 1994.

[10] A. Djebbari and F. Bereksi-Reguig, "Séparation de la systole et la diastole par des approches énergétiques et temporelles," in *Séminaire National sur l'Automatique et les Signaux (SNAS'99).* University Badji Mokhtar, Annaba, Algeria, 1999.

[11] H. Liang, S. Lukkarinen, and I. Hartimo, "Heart sound segmentation algorithm based on heart sound envelogram," in *Computers in Cardiology 1997.* IEEE, 1997, pp. 105–108.

[12] W. Clarke, S. Austin, P. Shah, P. Griffin, J. Dove, J. McCullough, and B. Schreiner, "Spectral energy of the first heart sound in acute myocardial ischemia. A correlation with electrocardiographic, hemodynamic, and wall motion abnormalities," *Circulation*, vol. 57, no. 3, p. 593, 1978.

[13] P. Stein, H. Sabbah, J. Lakier, S. Kemp, and D. Magilligan Jr, "Frequency spectra of the first heart sound and of the aortic component of the second heart sound in patients with degenerated porcine bioprosthetic valves," *The American Journal of Cardiology*, vol. 53, no. 4, pp. 557–561, 1984.

[14] S. Choi, Y. Shin, and H. Park, "Selection of wavelet packet measures for insufficiency murmur identification," *Expert Systems with Applications*, vol. 38, no. 4, pp. 4264–4271, 2011.

[15] B. Al-Naami, J. Chebil, and J. Torry, "Identification of aortic stenosis disease using discrete wavelet packet analysis," in *Computers in Cardiology, 2005.* IEEE, 2005, pp. 667–670.

[16] H. Liang and I. Nartimo, "A feature extraction algorithm based on wavelet packet decomposition for heart sound signals," in *Time-Frequency and Time-Scale Analysis, 1998. Proceedings of the IEEE-SP International Symposium on.* IEEE, 1998, pp. 93–96.

[17] M. R. Otelio S. and D. S. Romaine, *The Encyclopedia of the Heart and Heart Disease*, 1st ed. Facts on File, Jan. 2005.

[18] L. Durand and R. Guardo, "A model of the heart-thorax acoustic system," *Applications of computers in medicine*, pp. 29–41, 1982.

[19] P. Iaizzo, *Handbook of cardiac anatomy, physiology, and devices.* Humana Pr Inc, 2009.

[20] J. Enderle, J. Bronzino, and S. Blanchard, *Introduction to biomedical engineering.* Academic Press, 2005.

[21] R. E. Klabunde, *Cardiovascular physiology concepts.* Lippincott Williams & Wilkins, 2005.

[22] F. Smith, B. Keene, and L. Tilley, *Rapid Interpretation of Heart Sounds, Murmurs, Arrhythmias, and Lung Sounds: A Guide to Cardiac Auscultation in Dogs and Cats.* Elsevier. 2nd Edition. St Louis, 2007.

[23] J. Butterworth, *Cardiac auscultation, including audiovisual principles.* Grune and Stratton, 1960.

[24] K. Holldack and K. Gahl, *Auscultation et percussion: inspection et palpation.* Vigot, 1995.

[25] G. S. Bause, "Laënnec's 1819 stethoscope," *Anesthesiology*, vol. 112, no. 1, p. 18, Jan. 2010.

[26] L. Durand, J. Genest, and R. Guardo, "Modeling of the transfer function of the Heart-Thorax acoustic system in dogs," *IEEE Transactions on Biomedical Engineering*, vol. BME-32, no. 8, pp. 592–601, Aug. 1985.

[27] V. A. McKusick, "Cardiovascular sound in health and disease," *The American Journal of the Medical Sciences*, vol. 238, no. 1, p. 128, 1959.

[28] W. Dock, "Mode of production of the first heart sound," *Archives of Internal Medicine*, vol. 51, no. 5, p. 737, 1933.

[29] A. Leatham, *Auscultation of the Heart and Phonocardiography.* Churchill Livingstone, 1975.

[30] M. E. Tavel, *Clinical phonocardiography and external pulse recording.* Year Book Medical Publishers, 1985.

[31] P. D. Stein and A. Physical, "Physiological basis for the interpretation of cardiac auscultation: Evaluation based primarily on the second sound and ejection murmurs," *Futura, Mount Kisco, NY*, pp. 1–16, 1981.

[32] R. S. ROSS and J. M. CRILEY, "Cineangiocardiographic studies of the origin of cardiovascular physical signs," *Circulation*, vol. 30, no. 2, p. 255, 1964.

[33] W. Waider and E. Craige, "First heart sound and ejection sounds: Echocardiographic and phonocardiographic correlation with valvular events," *The American Journal of Cardiology*, vol. 35, no. 3, pp. 346–356, Mar. 1975. [Online]. Available: http://www.sciencedirect.com/science/article/pii/0002914975900260

[34] R. Rushmer, *Cardiovascular dynamics.* Saunders (Philadelphia), 1976, vol. 4.

[35] A. Luisada, "Changing views on the mechanism of the first and second heart sounds," *American Heart Journal*, vol. 88, no. 4, pp. 503–514, Oct. 1974. [Online]. Available: zotero://attachment/329/

[36] A. A. Luisada, B. Coleman, D. Wallick, and P. K. Bhat, "On the function of the aortic valve and the mechanism of the first and second sounds," *Japanese Heart Journal*, vol. 18, no. 1, pp. 81–91, Jan. 1977, PMID: 846050. [Online]. Available: http://www.ncbi.nlm.nih.gov/pubmed/846050

[37] A. A. Luisada, D. M. MacCanon, B. Coleman, and L. P. Feigen, "New studies on the first heart sound," *The American Journal of Cardiology*, vol. 28, no. 2, pp. 140–149, Aug. 1971. [Online]. Available: http://www.sciencedirect.com/science/article/pii/0002914971903626

[38] A. A. Luisada, C. K. Liu, C. Aravanis, M. Testelli, and J. Morris, "On the mechanism of production of the heart sounds," *American Heart Journal*, vol. 55, no. 3, pp. 383–399, Mar. 1958. [Online]. Available: http://www.sciencedirect.com/science/article/pii/0002870358900541

[39] A. Luisada, *The sounds of the normal heart.* WH Green Tokyo: Igaku Shoin, St. Louis, 1972.

[40] A. A. Luisada, L. P. Feigen, and K. Mori, "On the unitary nature of cardiac vibrations," *Japanese Heart Journal*, vol. 14, pp. 406–413, 1973.

[41] L. G. Durand, Y. E. Langlois, T. Lanthier, R. Chiarella, P. Coppens, S. Carioto, and S. Bertrand-Bradley, "Spectral analysis and acoustic transmission of mitral and aortic valve closure sounds in dogs. part 1. modelling the heart/thorax acoustic system," *Medical & Biological Engineering & Computing*, vol. 28, no. 4, pp. 269–277, July 1990, PMID: 2246923. [Online]. Available: http://www.ncbi.nlm.nih.gov/pubmed/2246923

[42] ——, "Spectral analysis and acoustic transmission of mitral and aortic valve closure sounds in dogs. part 2. effects of neuromuscular blockade, sternotomy and pacemaker control, and a two-week recovery period," *Medical & Biological Engineering & Computing*, vol. 28, no. 4, pp. 278–286, July 1990, PMID: 2246924. [Online]. Available: http://www.ncbi.nlm.nih.gov/pubmed/2246924

[43] ——, "Spectral analysis and acoustic transmission of mitral and aortic valve closure sounds in dogs. part 3 effects of altering heart rate and P-R interval," *Medical & Biological Engineering & Computing*, vol. 28, no. 5, pp. 431–438, Sept. 1990. [Online]. Available: http://www.springerlink.com/content/5n183621vn957664/

[44] ——, "Spectral analysis and acoustic transmission of mitral and aortic valve closure sounds in dogs. part 4: Effect of modulating cardiac inotropy," *Medical & Biological Engineering & Computing*, vol. 28, no. 5, pp. 439–445, Sept. 1990, PMID: 2277544. [Online]. Available: http://www.ncbi.nlm.nih.gov/pubmed/2277544

[45] A. E. Aubert, B. G. Denys, F. Meno, and P. S. Reddy, "Digital spectrum analysis of quantitative intracardiac and external heart sounds," *J. Cardiography*, vol. 14, pp. 159–163, 1984.

[46] A. E. Aubert, B. G. Denys, H. DE GEEST, F. Meno, and P. S. Reddy, "Quantitative phono study of intracardiac and external heart sounds," in *Proc. 1982 Computers in Cardiology Conf., IEEE Computer Society*, 1982, pp. 501–504.

[47] F. Meno, P. S. Reddy, and L. Bernardi, "Heart sound propagation in the human thorax," *Clinical Physics and Physiological Measurement*, vol. 6, p. 123, 1985.

[48] D. Smith, T. Ishimitsu, and E. Craige, "Mechanical vibration transmission characteristics of the left ventricle: implications with regard to auscultation and phonocardiography," *Journal of the American College of Cardiology*, vol. 4, no. 3, pp. 517–521, 1984.

[49] L. G. Durand, Y. E. Langlois, T. Lanthier, R. Chiarella, P. Coppens, F. Lemire, M. Jarry, A. Solignac, and Y. Latour, "Acoustic transmission of the aortic component of the second heart sound in humans, dogs and pigs," *Innovation et technologie en biologie et mÃľdecine*, vol. 10, no. 4, pp. 383–398, 1989.

[50] P. S. Reddy, R. Salerni, and J. A. Shaver, "Normal and abnormal heart sounds in cardiac diagnosis: Part II. diastolic sounds," *Current Problems in Cardiology*, vol. 10, no. 4, pp. 1–55, Apr. 1985, PMID: 3158481. [Online]. Available: http://www.ncbi.nlm.nih.gov/pubmed/3158481

[51] J. A. Shaver, R. Salerni, and P. S. Reddy, "Normal and abnormal heart sounds in cardiac diagnosis. part i: Systolic sounds," *Current Problems in Cardiology*, vol. 10, no. 3, pp. 1–68, Mar. 1985, PMID: 3996020. [Online]. Available: http://www.ncbi.nlm.nih.gov/pubmed/3996020

[52] J. Abrams, "Current concepts of the genesis of heart sounds i. first and second sounds," *JAMA: the journal of the American Medical Association*, vol. 239, no. 26, pp. 2787–2789, 1978.

[53] ——, "Current concepts of the genesis of heart sounds II. third and fourth sounds," *JAMA: The Journal of the American Medical Association*, vol. 239, no. 19, pp. 2029 –2030, May 1978. [Online]. Available: http://jama.ama-assn.org/content/239/19/2029.short

[54] J. Ronan Jr, "Cardiac auscultation: the first and second heart sounds." *Heart disease and stroke: a journal for primary care physicians*, vol. 1, no. 3, p. 113, 1992.

[55] ——, "Cardiac auscultation: the third and fourth heart sounds." *Heart disease and stroke: a journal for primary care physicians*, vol. 1, no. 5, p. 267, 1994.

[56] A. G. Tilkian, M. B. Conover, and W. S. Company, *Understanding heart sounds and murmurs*. Saunders, 1979.

[57] L. Cohen, "Time-frequency distributions-a review," *Proceedings of the IEEE*, vol. 77, no. 7, pp. 941–981, 1989.

[58] B. Boashash, *Time frequency signal analysis and processing: a comprehensive reference*. Elsevier Science, 2003.

[59] ——, "Wigner analysis of time-varying signalsŮits application in seismic prospecting," in *Proc. European Signal Processing Conf.(EUSIPCO-83)*, 1983, pp. 703–706.

[60] B. Boashash and B. Escudie, "Wigner-ville analysis of asymptotic signals and applications," *Signal processing*, vol. 8, no. 3, pp. 315–327, 1985.

[61] J. Imberger and B. Boashash, "Application of the wigner-ville distribution to temperature gradient microstructure: A new technique to study small-scale variations," *Journal of Physical Oceanography*, vol. 16, 1986.

[62] T. Claasen and W. Mecklenbrauker, "The wigner distribution – a tool for time frequency signal analysis. part iii: Relations with other time–frequency signal transformations," *Philips J. Res*, vol. 35, no. 6, pp. 372–389, 1980.

[63] F. Hlawatsch and G. Boudreaux-Bartels, "Linear and quadratic time-frequency signal representations," *Signal Processing Magazine, IEEE*, vol. 9, no. 2, pp. 21–67, 1992.

[64] E. Wigner, "On the quantum correction for thermodynamic equilibrium," *Physical Review*, vol. 40, no. 5, pp. 749–752, 1932.

[65] P. Flandrin and W. Martin, "A general class of estimators for the wigner-ville spectrum of non-stationary processes," *Analysis and Optimization of Systems*, pp. 15–23, 1984.

[66] T. Claasen and W. Mecklenbrauker, "The wigner distribution – a tool for time frequency signal analysis. part i: Continuous time signals," *Philips J. Res*, vol. 35, no. 3, pp. 217–250, 1980.

[67] ——, "The wigner distribution – a tool for time frequency signal analysis. part ii: Discrete time signals," *Philips J. Res*, vol. 35, no. 4/5, pp. 276–300, 1980.

[68] H. Choi and W. Williams, "Improved time-frequency representation of multicomponent signals using exponential kernels," *Acoustics, Speech and Signal Processing, IEEE Transactions on*, vol. 37, no. 6, pp. 862–871, 1989.

[69] K. Kodera, R. Gendrin, and C. Villedary, "Analysis of time-varying signals with small bt values," *Acoustics, Speech and Signal Processing, IEEE Transactions on*, vol. 26, no. 1, pp. 64–76, 1978.

[70] ——, "A new method for the numerical analysis of time–varying signals with small bt values," *Phys. Earth Planet. Interiors*, no. 12, pp. 142–150, 1976.

[71] D. Gabor, "Theory of communication," *Inst. Electron. Eng.*, vol. 93, no. 11, pp. 429–457, Nov. 1946.

[72] F. Auger and P. Flandrin, "Improving the readability of time-frequency and time-scale representations by the reassignment method," *Signal Processing, IEEE Transactions on*, vol. 43, no. 5, pp. 1068–1089, 1995.

[73] S. Hainsworth and M. Macleod, "Time frequency reassignment: A review and analysis," *Cambridge University Engineering Department, Tech. Rep. CUED/FINFENG/TR*, vol. 459, 2003.

[74] E. Chassande-Mottin and P. Flandrin, "On the time-frequency detection of chirps," *Applied and Computational Harmonic Analysis*, vol. 6, no. 2, pp. 252–281, 1999.

[75] C. Page, "Instantaneous power spectra," *Journal of Applied Physics*, vol. 23, no. 1, pp. 103–106, 1952.

[76] S. Mallat, "A theory for multiresolution signal decomposition: The wavelet representation," *IEEE transactions on pattern analysis and machine intelligence*, vol. 11, no. 7, pp. 674–693, 1989.

[77] ——, "A wavelet tour of signal processing. 1998," *Academic, San Diego, CA*, 1998.

[78] ——, "Multiresolution approximations and wavelet orthonormal bases of L 2 (R)," *Transactions of the American Mathematical Society*, vol. 315, no. 1, pp. 69–87, 1989.

[79] P. Welch, "The use of fast fourier transform for the estimation of power spectra: a method based on time averaging over short, modified periodograms," *Audio and Electroacoustics, IEEE Transactions on*, vol. 15, no. 2, pp. 70–73, 1967.

[80] P. Flandrin, *Time-frequency/time-scale analysis*. Academic Pr, 1999.

[81] R. Coifman, Y. Meyer, and V. Wickerhauser, "Wavelet analysis and signal processing," in *In Wavelets and their Applications*. Citeseer, 1992.

[82] G. Strang and T. Nguyen, *Wavelets and filter banks*. Wellesley Cambridge Pr, 1996.

[83] Y. Meyer, *Les ondelettes. Algorithmes et applications*. Colin Ed., 1993.

[84] M. Wickerhauser, *Adapted wavelet analysis from theory to software*. AK Peters Ltd, 1994.

[85] Q. Zhang, A. Manriquez, C. Medigue, Y. Papelier, and M. Sorine, "Robust and efficient location of t-wave ends in electrocardiogram," in *Computers in Cardiology, 2005*. IEEE, 2005, pp. 711–714.

[86] Q. Zhang, A. Manriquez, C. Médigue, Y. Papelier, and M. Sorine, "An algorithm for robust and efficient location of t-wave ends in electrocardiograms," *Biomedical Engineering, IEEE Transactions on*, vol. 53, no. 12, pp. 2544–2552, 2006.

[87] P. Laguna, R. Mark, A. Goldberg, and G. Moody, "A database for evaluation of algorithms for measurement of qt and other waveform intervals in the ecg," in *Computers in Cardiology 1997*. IEEE, 1997, pp. 673–676.

[88] J. Xu, L. Durand, and P. Pibarot, "Nonlinear transient chirp signal modeling of the aortic and pulmonary components of the second heart sound," *IEEE Transactions on Biomedical Engineering*, vol. 47, no. 10, pp. 1328–1335, 2000.

[89] ——, "Extraction of the aortic and pulmonary components of the second heart sound using a nonlinear transient chirp signal model," *IEEE transactions on biomedical engineering*, vol. 48, no. 3, pp. 277–283, 2001.

[90] B. Boashash, "Estimating and interpreting the instantaneous frequency of a signal. ii. algorithms and applications," *Proceedings of the IEEE*, vol. 80, no. 4, pp. 540–568, 1992.

[91] A. Djebbari and F. Bereksi-Reguig, "First heart sound time–frequency analysis using modified Wigner–Ville Distributions," in *International Conference on the Image and Signal Processing and their Applications (ISPA'10)*, 2010.

[92] L. G. Durand and P. Pibarot, "Digital signal processing of the phonocardiogram: review of the most recent advancements," *Critical Reviews in Biomedical Engineering*, vol. 23, no. 3-4, pp. 163–219, 1995, PMID: 8853950. [Online]. Available: http://www.ncbi.nlm.nih.gov/pubmed/8853950

[93] J. Wood and D. Barry, "Time-frequency analysis of the first heart sound," *Engineering in Medicine and Biology Magazine, IEEE*, vol. 14, no. 2, pp. 144–151, 1995.

[94] J. Wood, A. Buda, and D. Barry, "Time-frequency transforms: a new approach to first heart sound frequency dynamics," *Biomedical Engineering, IEEE Transactions on*, vol. 39, no. 7, pp. 730–740, 1992.

[95] A. Djebbari and F. Bereksi-Reguig, "Smoothed-pseudo wigner-ville distribution of normal and aortic stenosis heart sounds," *Journal of Mechanics in Medicine and Biology*, vol. 5, no. 3, p. 415, 2005.

[96] N. Mehta and I. Khan, "Third heart sound: genesis and clinical importance," *International journal of cardiology*, vol. 97, no. 2, pp. 183–186, 2004.

[97] E. Folland, B. Kriegel, W. Henderson, K. Hammermeister, and G. Sethi, "Implications of third heart sounds in patients with valvular heart disease," *New England Journal of Medicine*, vol. 327, no. 7, pp. 458–462, 1992.

[98] Y. Zhu, F. Peyrin, and R. Goutte, "Transformation de wigner-ville: description d'un nouvel outil de traitement du signal et des images," *Annals of Telecommunications*, vol. 42, no. 3, pp. 105–118, 1987.

[99] J. Xu, L. Durand, and P. Pibarot, "A new, simple, and accurate method for non-invasive estimation of pulmonary arterial pressure," *Heart*, vol. 88, no. 1, pp. 76–80, 2002.

[100] M. Fisher, P. Forfia, E. Chamera, T. Housten-Harris, H. Champion, R. Girgis, M. Corretti, and P. Hassoun, "Accuracy of doppler echocardiography in the hemodynamic assessment of pulmonary hypertension," *American journal of respiratory and critical care medicine*, vol. 179, no. 7, pp. 615–621, 2009.

[101] J. Rich, S. Shah, R. Swamy, A. Kamp, and S. Rich, "Inaccuracy of doppler echocardiographic estimates of pulmonary artery pressures in patients with pulmonary hypertension," *Chest*, vol. 139, no. 5, pp. 988–993, 2011.

[102] D. Chen, L. Durand, and H. Lee, "Time-frequency analysis of the first heart sound. part 1: simulation and analysis," *Medical and Biological Engineering and Computing*, vol. 35, no. 4, pp. 306–310, 1997.

[103] W. Thompson and S. Mehrotra, "Cardiac history and physical examination," *Heart Diseases in Children*, pp. 3–16, 2011.

[104] R. Poley and B. White, "Heart murmurs," *Sports Cardiology Essentials*, pp. 213–234, 2011.

[105] A. Djebbari and F. Bereksi-Reguig, "Detection of the valvular split within the second heart sound using the reassigned smoothed pseudo wigner-ville distribution," *Biomedical engineering online*, vol. 12, no. 1, p. 37, 2013.

[106] T. Tran, N. Jones, and J. Fothergill, "Heart sound simulator," *Medical and Biological Engineering and Computing*, vol. 33, no. 3, pp. 357–359, 1995.

[107] Y. Tang, C. Danmin, and L. Durand, "The synthesis of the aortic valve closure sound of the dog by the mean filter of forward and backward predictor," *Biomedical Engineering, IEEE Transactions on*, vol. 39, no. 1, pp. 1–8, 1992.

[108] A. Baykal, Y. Ziya Ider, and H. Koymen, "Distribution of aortic mechanical prosthetic valve closure sound model parameters on the surface of the chest," *Biomedical Engineering, IEEE Transactions on*, vol. 42, no. 4, pp. 358–370, 1995.

[109] X. Zhang, L. Durand, L. Senhadji, H. Lee, and J. Coatrieux, "Analysis-synthesis of the phonocardiogram based on the matching pursuit method," *Biomedical Engineering, IEEE Transactions on*, vol. 45, no. 8, pp. 962–971, 1998.

[110] ——, "Time-frequency scaling transformation of the phonocardiogram based of the matching pursuit method," *Biomedical Engineering, IEEE Transactions on*, vol. 45, no. 8, pp. 972–979, 1998.

[111] J. Xu, P. Pibarot, and L. Durand, "Method and apparatus for estimating systolic and mean pulmonary artery pressures of a patient," Apr. 9 2002, uS Patent 6,368,283.

[112] J. Shaver, R. Salerni, and P. Reddy, "Normal and abnormal heart sounds in cardiac diagnosis. part i: Systolic sounds." *Current problems in cardiology*, vol. 10, no. 3, p. 1, 1985.

[113] P. Reddy, R. Salerni, and J. Shaver, "Normal and abnormal heart sounds in cardiac diagnosis: Part ii. diastolic sounds." *Current problems in Cardiology*, vol. 10, no. 4, p. 1, 1985.

[114] A. Illanes-Manriquez and Q. Zhang, "An algorithm for robust detection of qrs onset and offset in ecg signals," in *Computers in Cardiology, 2008.* IEEE, 2008, pp. 857–860.

[115] I. Daubechies, "The wavelet transform, time-frequency localization and signal analysis," *Information Theory, IEEE Transactions on*, vol. 36, no. 5, pp. 961–1005, 1990.

[116] P. Abry, *Ondelettes et turbulences: multirésolutions, algorithmes de décomposition, invariance d'échelle et signaux de pression.* Diderot multimédia, 1997.

[117] H. Koymen, B. Altay, and Y. Ider, "A study of prosthetic heart valve sounds," *Biomedical Engineering, IEEE Transactions on*, no. 11, pp. 853–863, 1987.

[118] H. Sava and J. McDonnell, "Spectral composition of heart sounds before and after mechanical heart valve implantation using a modified forward-backward prony's method," *Biomedical Engineering, IEEE Transactions on*, vol. 43, no. 7, pp. 734–742, 1996.

[119] H. Sava, P. Grant, and J. McDonnell, "Spectral characterization and classification of carpentier-edwards heart valves implanted in the aortic position," *Biomedical Engineering, IEEE Transactions on*, vol. 43, no. 10, pp. 1046–1048, 1996.

[120] S. Aggio, E. Baracca, C. Longhini, C. Brunazzi, L. Longhini, G. Musacci, and C. Fersini, "Noninvasive estimation of the pulmonary systolic pressure from the spectral analysis of the second heart sound," *Acta cardiologica*, vol. 45, no. 3, pp. 199–202, 1990.

[121] C. Longhini, E. Baracca, C. Brunazzi, M. Vaccari, L. Longhini, and F. Barbaresi, "A new noninvasive method for estimation of pulmonary arterial pressure in mitral stenosis," *The American journal of cardiology*, vol. 68, no. 4, pp. 398–401, 1991.

[122] A. Bartels and D. Harder, "Non-invasive determination of systolic blood pressure by heart sound pattern analysis," *Clinical Physics and Physiological Measurement*, vol. 13, p. 249, 1992.

[123] M. Farge, "Wavelet transforms and their applications to turbulence," *Annual Review of Fluid Mechanics*, vol. 24, no. 1, pp. 395–458, 1992.

[124] P. Stoica and R. Moses, *Introduction to spectral analysis*. Prentice Hall Upper Saddle River, NJ, 1997, vol. 51.

[125] A. Oppenheim, R. Schafer, J. Buck, *et al.*, *Discrete-time signal processing*. Prentice hall Upper Saddle River^ eN. JNJ, 1989, vol. 2.

[126] M. Misiti, Y. Misiti, and G. Oppenheim, *Les ondelettes et leurs applications*. Hermès Science, 2003.

[127] I. Daubechies, *Ten lectures on wavelets*. Society for Industrial Mathematics, 1992, vol. 61.

[128] J. Eyster, "Studies on the venous pulse," *The Journal of Experimental Medicine*, vol. 14, no. 6, pp. 594–605, 1911.

[129] G. Amit, K. Shukha, N. Gavriely, and N. Intrator, "Respiratory modulation of heart sound morphology," *American Journal of Physiology-Heart and Circulatory Physiology*, vol. 296, no. 3, pp. H796–H805, 2009.

[130] M. Hayes, "Statistical digital signal processing and modeling, by john wiley and sons," *New York*, 1996.

[131] J. Rafiee, M. Rafiee, N. Prause, and M. Schoen, "Wavelet basis functions in biomedical signal processing," *Expert Systems With Applications*, 2010.

# Appendix A

# Developed software

All graphical user interfaces were developed within a MATLAB environment.

## A.1 PCG Recorder

The *PCG Recorder* software gathers some *Data acquisition Toolbox* basic functionalities of a MATLAB environment. Phonocardiographic signals were recorded in 16 bits resolution at various sampling frequencies that avoid spectral aliasing. Several clinical patient's information are also recorded as metadata. Data and metadata were saved as data files with a structure format with PCG extension.

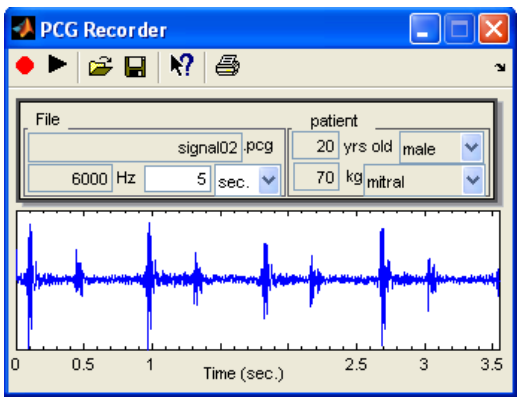


Figure A.1: Graphical user interface of *PCG Recorder* software [2, 3] developed under a MATLAB environment

## A.2 PCG Segmentation

A software was developed within a MATLAB environment to segment PCG signals of the LGB–IRCM cardiac valve database. The graphical user interface (GUI) of this software is illustrated in Figure A.2. Segmentation of the PCG signal is achieved according to systole and diastole phases by detecting the R–peak and the end of the T–wave of the simultaneously recorded ECG signal. Signals were adjusted by cross–correlation to avoid jitter during diastole phases.

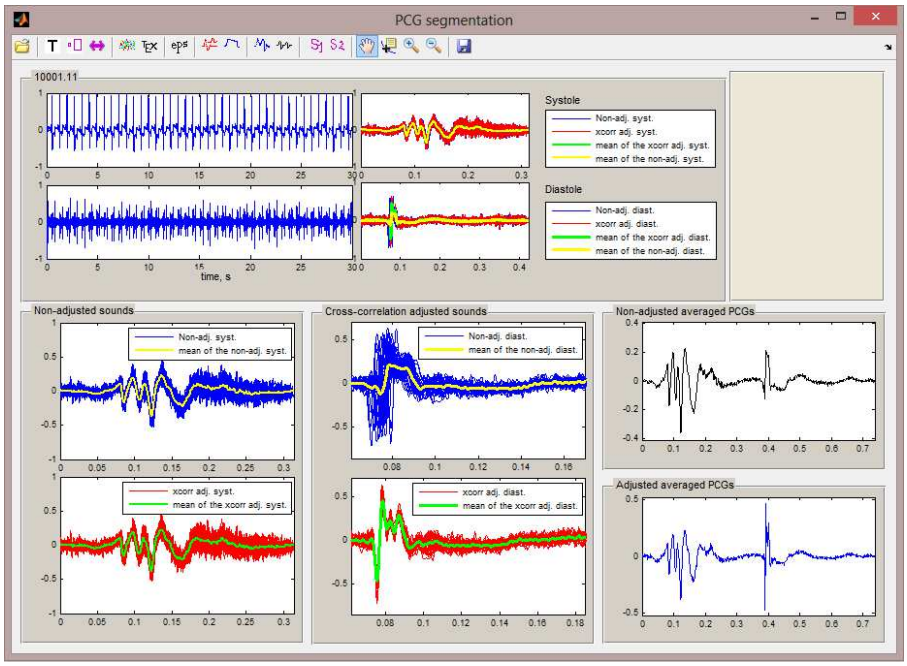


Figure A.2: Graphical User Interface of *PCG segmentation* software

## A.3 PCG WP Analyser

The GUI illustrated in Figure A.3 represents wavelet packets analysis software developed during this work.

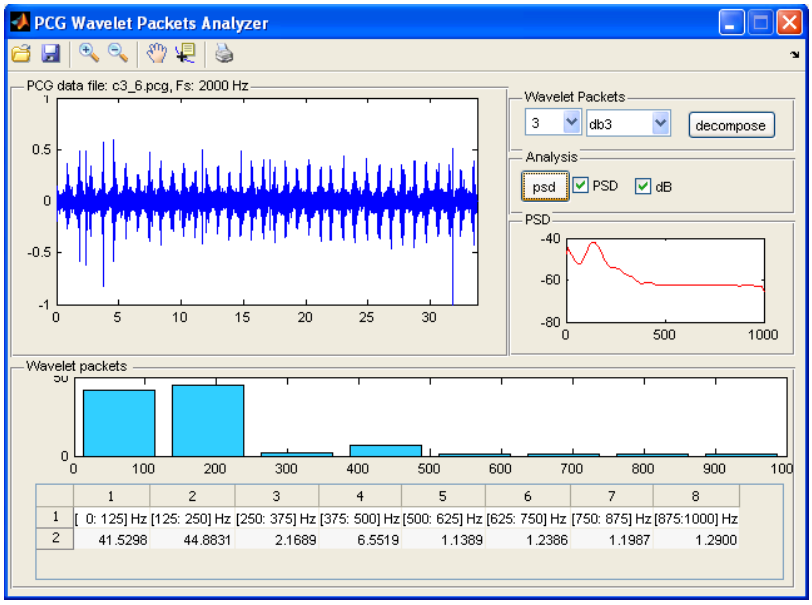


Figure A.3: Graphical User Interface of *Wavelet packets PCG Analyser* software

## A.4 PCG simulator

Software illustrated in Figure A.4 is based on the valvular heart sound model (see section III.3.4). Data are saved in WAV or MP3 format at a high audio quality.


Figure A.4: Graphical User Interface *PCG Simulator* software.

## A.5 Time–frequency analysis software

Several command line functions for time–frequency analysis were developed under a MATLAB environment.

# Appendix A

# LGB–IRCM cardiac valve database – Additional information

## A.1 LGB–IRCM cardiac valve database 10078: Aortic stenosis (light)

- Rythm: pacemaker
- Third heart sound: no
- Heart rate: 74 bpm
- Arterial systolic pressure: 140 mmHg
- Arterial diastolic pressure: 88 mmHg
- Systolic murmur: yes
- Diastolic murmur: no
- New York Heart Association (NYHA) functional class; 2: dyspnea with a reasonable exercise
- Position of the prosthesis: aortic
- Prosthesis type: St–Jude bioprosthesis
- Model: A801
- Prosthesis size: 23 mm
- Morphology of the bioprosthesis: normal
- Hemodynamic function of the bioprosthesis: abnormal

- Transvalvular regurgitation: normal
- Perivalvular regurgitation: normal
- Stenosis: **light**
- Patient–prosthesis disproportion: no
- Movement of rocker: no
- Mobility of the leaflets: normal
- Thickening of the leaflets: no
- Tear of the leaflets: no
- Extrinsic calcification of the leaflets: no
- Intrinsic calcification of the leaflets: no

## A.2 LGB–IRCM cardiac valve database 20008: Aortic stenosis (light)

- Rythm: auricular fibrillation
- Third heart sound: no
- Heart rate: 88 bpm
- Arterial systolic pressure: 110 mmHg
- Arterial diastolic pressure: 60 mmHg
- Systolic murmur: yes
- Diastolic murmur: yes
- New York Heart Association (NYHA) functional class; 3: dyspnea with light or moderated exercise.
- Position of the prosthesis: aortic
- Prosthesis type: Carpentier–Edwards bioprosthesis
- Model: 2625
- Prosthesis size: 23 mm
- Morphology of the bioprosthesis: abnormal
- Hemodynamic function of the bioprosthesis: abnormal

- Transvalvular regurgitation: moderated anomaly
- Perivalvular regurgitation: normal
- Stenosis: **mild**
- Patient–prosthesis disproportion: light anomaly
- Movement of rocker: no
- Mobility of the leaflets: normal
- Thickening of the leaflets: mild
- Tear of the leaflets: small
- Extrinsic calcification of the leaflets: no
- Intrinsic calcification of the leaflets: small

## A.3 LGB–IRCM cardiac valve database 10019: Aortic stenosis (severe)

- Rythm: sinus rhythm
- Third heart sound: no
- Heart rate: 67 bpm
- Arterial systolic pressure: 144 mmHg
- Arterial diastolic pressure: 70 mmHg
- Systolic murmur: yes
- Diastolic murmur: no
- New York Heart Association (NYHA) functional class; 3: dyspnea with light or moderated exercise.
- Position of the prosthesis: aortic
- Prosthesis type: non–common bioprosthesis type
- Model: MMI
- Prosthesis size: 21 mm
- Morphology of the bioprosthesis: abnormal
- Hemodynamic function of the bioprosthesis: abnormal

- Transvalvular regurgitation: moderated anomaly
- Perivalvular regurgitation: normal
- Stenosis: **severe**
- Patient–prosthesis disproportion: normal
- Movement of rocker: no
- Mobility of the leaflets: reduced
- Thickening of the leaflets: moderated
- Tear of the leaflets: no
- Extrinsic calcification of the leaflets: moderated
- Intrinsic calcification of the leaflets: no

## Abstract

**This thesis investigates the time--frequency content of phonocardiographic signals through advanced digital signal processing methods. As a first part, heart sounds and murmurs are studied to understand their nature and genesis. The multidegree of freedom theory concludes several theories behind genesis of heart sounds and murmurs. Understanding the genesis theory allow to select the appropriate tool for analysis. In the second part, time–frequency methods are studied through their theoretical background. Practical applications complement the study to select the adequate time--frequency methods to be used during analysis. The Reassigned smoothed pseudo Wigner–Ville distribution among several time--frequency methods brings to light the required digital signal processing elements to appropriately process information within phonocardiographic data. Finally, several techniques were developed to support the selected time--frequency methods as adaptive algorithms towards extracting information from heart sounds and murmurs. An adjustment algorithm was developed to resolve the amplitude attenuation issue within heart sounds. Additionally, a dechirping algorithm was developed to resolve the phase cancellation issue that cancel valuable valvular sounds during their transmission from the heart to the chest. A detection algorithm of the valvular split within heart sounds based on the Reassigned smoothed pseudo Wigner–Ville distribution was developed. These algorithms were validated on simulated and real heart sounds. Phonocardiographic signals were recorded within the CHUT (Centre hospitalier universitaire de Tlemcen), and from the LGB–IRCM (Laboratoire de Génie biomédical -- Institut de recherches cliniques de Montréal) cardiac valve database. A mother wavelet was developed from the Valvular chirplet model valvular heart sounds. This mother wavelet allowed better scalograms in comparison to usual Morlet and discrete Meyer wavelets. A global analysis of abnormal phonocardiographic signals was performed by wavelet packets to localise energy within the forming frequency subbands of the analysed signal.**

**Keywords: Phonocardiography, time–frequency analysis, Wigner–Ville distribution, Wavelets.**

## Résumé

**Cette thèse explore le contenu temps–fréquence des signaux phonocardiographiques à travers des méthodes avancées de traitement numérique du signal. En première partie, les bruits et souffles cardiaques sont étudiés afin de comprendre leur nature et leur origine. La théorie multidegré de liberté conclue plusieurs théories à l'origine des bruits et souffles cardiaques. Comprendre la théorie de génération permet de sélectionner l'outil d'analyse approprié. En seconde partie, des méthodes temps–fréquence sont étudiées à travers leur théorie. Des applications pratiques complète l'étude pour sélectionner les méthodes temps–fréquence adéquate à utiliser dans l'analyse. La distribution pseudo Wigner–Ville lissée et réallouée parmi plusieurs méthodes temps–fréquence apporte les éléments de traitement numérique du signal permettant de mieux traiter l'information des données phonocardiographiques. Finalement, plusieurs techniques ont été développées pour soutenir le choix des méthodes temps–fréquence comme algorithme adaptée à l'extraction de l'information des bruits et souffles cardiaques. Un algorithme d'ajustement a été développé pour résoudre la problématique d'atténuation d'amplitude des bruits cardiaques. En plus, un algorithme de séparation a été développé pour résoudre la problématique d'annulation de phase qui élimine les précieux bruits valvulaire pendant leur transmission du cœur vers le thorax. Un algorithme de détection du split valvulaire dans les bruits cardiaques basés sur la distribution pseudo Wigner–Ville lissée et réallouée a été développé. Ces algorithmes ont été validés sur des bruits cardiaques simulés et réels. Des signaux phonocardiographiques ont été enregistrés au niveau du Centre hospitalier universitaire de Tlemcen, et de la base de données du Laboratoire de génie biomédical de l'Institut de recherches cliniques de Montréal. Une ondelette mère a été développée à partir du modèle chirplet valvulaire, Cette ondelette mère permet des scalogrammes meilleurs en comparaison aux ondelettes de Morlet et de Meyer discrète. Une analyse globale des signaux phonocardiographiques a été réalisée par packets d'ondelettes afin de localiser l'énergie dans les sous–bandes fréquentielles du signal analysé.**

**Mots clés: Phonocardiographie, analyse temps–fréquence, Distribution de Wigner–Ville, Ondelettes.**

## ملخص

هذه الأطروحة تستكشف المضمون الزمني–الطيفي للاشارات الصوتية القلبية عن طريق المعالجة الرقمية للاشارة. كجزء أول، الأصوات القلبية درست لفهم طبيعتها و مصادرها. النظرية متعددة الحريات تلخص نظريات عدة حول مصدر الأصوات القلبية. فهم نظرية اصدار هذه الأصوات يمكن من اختيار وسيلة التحليل المناسبة. توزيع وغنر–فيل من بين طرق زمنية–طيفية تعزز المعالجة الرقمية الاشارة و تمكن التحليل الأنسب للمعلومة المتواجدة بالأصوات القلبية. و ختاما، تقنيات متعددة طورت لمساندة اختيار طريقة التحليل الزمنية–الطيفية كخوارزمية مكيفة لاستخلاص المعلومة من الأصوات القلبية.

خوارزمية تطابق طورت لحل اشكالية انخفاض شدة الأصوات القلبية. زيادة على هذا، خوارزمية فصل طورت لحل اشكالية انعدام الطور المتسبب بحذف الأصوات الصمامية القلبية خلال ارسالها من القلب الى الصدر. خوارزمية كشف الفاصل بين الأصوات القلبية المعتمدة على توزيع وغنر–فيل قد تم تطويرها. هذه الخوارزميات صودقت على أصوات مصطنعة و أخرى حقيقية.

اشارات قلبية سجلت بالمستشفى الجامعي ابتلمسان و كذا بمخبر الأبحاث الاكلينيكية بمونتريال بكندا. من خلال هذا البحث، طورت مويجة خاصة بتحليل الأصوات القلبية و ذلك لاستخلاص الطاقة المتواجدة داخل هذه الاشارات القلبية.

الكلمات المفتاحية: الأصوات القلبية، التحليل الزمني الطيفي، توزيع وغنر–فيل، المويجات.